TURUN
YLIOPISTO
UNIVERSITY
OF TURKU

Amphiphile-Templated Dynamic Combinatorial Libraries

Jinghui Yang

TURUN YLIOPISTON JULKAISUJA – ANNALES UNIVERSITATIS TURKUENSIS
SARJA – SER. AI OSA – TOM. 758 | ASTRONOMICA – CHEMICA – PHYSICA – MATHEMATICA | TURKU 2026

TURUN
YLIOPISTO
UNIVERSITY
OF TURKU

AMPHIPHILE-TEMPLATED DYNAMIC COMBINATORIAL LIBRARIES

Jinghui Yang

TURUN YLIOPISTON JULKAISUJA – ANNALES UNIVERSITATIS TURKUENSIS
SARJA – SER. AI OSA – TOM. 758 | ASTRONOMICA - CHEMICA - PHYSICA – MATHEMATICA | TURKU 2026

University of Turku

Faculty of Science
Department of Chemistry
Chemistry
Doctoral Programme in Exact Sciences

Supervised by

Doctor Jianwei Li,
MediCity Research Laboratory
University of Turku
Turku, Finland

Professor Tuomas Lönnberg
Department of Chemistry
University of Turku
Turku, Finland

Reviewed by

Professor Hao Li
Department of Chemistry
Zhejiang University
Zhejiang, China

Emeritus Professor Heikki Tenhu
Department of Chemistry
University of Helsinki
Helsinki, Finland

Opponent

Professor Kari Rissanen
Department of Chemistry
University of Jyväskylä
Jyväskylä, Finland

ISBN 978-952-02-0609-3 (PRINT)
ISBN 978-952-02-0610-9 (PDF)
ISSN 0082-7002 (Print)
ISSN 2343-3175 (Online)
Painosalama, Turku, Finland 2026

UNIVERSITY OF TURKU
Faculty of Science
Department of Chemistry
Chemistry
JINGHUI YANG: Amphiphile-Templated Dynamic Combinatorial Libraries
Doctoral Dissertation, 169 pp.
Doctoral Programme in Exact Sciences
03 2026

ABSTRACT

This thesis investigates amphiphile-templated dynamic combinatorial libraries (DCLs) operating through reversible thiol–disulfide exchange, with the aim of elucidating how amphiphilic organization governs molecular selection, amplification, and the emergence of function. By coupling dynamic covalent chemistry with amphiphilic self-assembly, a series of systems was established that exhibit redox-responsive fluorescence regulation, entropy-driven amplification, and persistent supramolecular chirality.

First, a short-chain tetraphenylethene (TPE) amphiphile was designed to act as both a structural template and a fluorescent reporter for oxidation-driven molecular network formation in living cells. Under intracellular oxidative conditions, disulfide bond formation among the building blocks strengthens their supramolecular assembly with the amphiphile and enhances fluorescence, whereas reduction cleaves disulfide bonds, disrupts the assembly, and attenuates the fluorescent response, providing a model for redox-regulated signal transduction in dynamic supramolecular assemblies.

Second, a long-chain TPE amphiphile served as a supramolecular template to preorganize disulfide building blocks in a dynamic combinatorial library, reducing entropic penalties and selectively amplifying octameric macrocycles. Complexation with doxorubicin enabled real-time visualization of drug release via aggregation-induced emission, linking dynamic combinatorial chemistry to functional delivery and optical readout.

Third, sodium dodecyl sulfate (SDS) micelles served as transient amphiphilic environments that reshape DCL composition. Distinct SDS concentrations selectively amplified pentameric, hexameric, or trimeric macrocycles, revealing environment-dependent selection. Notably, the pentamer expressed pronounced supramolecular chirality and retained its chiral bias after micelle removal, demonstrating an imprinting and memory effect.

Overall, these results establish amphiphilic templation as an effective strategy for directing adaptive behavior and information storage in dynamic molecular networks.

KEYWORDS: Dynamic combinatorial chemistry, Amphiphilic templation, Thiol–Disulfide exchange, Tetraphenylethene amphiphiles, Sodium dodecyl sulfate micelles, Aggregation-induced emission, Chiral memory

TURUN YLIOPISTO
Matemaattis-luonnontieteellinen tiedekunta
Kemian laitos
Kemia
JINGHUI YANG: Amfifiilitemplaatilla ohjatut dynaamiset kombinatoriset kirjastot
Väitöskirja, 169 s.
Eksaktien Tieteiden Tohtoriohjelma (EXACTUS)
03 2026

TIIVISTELMÄ

Tässä väitöskirjassa tutkitaan amfifiilisesti templatoituja dynaamisia kombinatorisia kirjastoja (DCL), jotka perustuvat palautuvaan tioli–disulfidinvaihtoon. Tutkimuksen tavoitteena on selvittää, miten amfifiilinen järjestäytyminen ohjaa molekyylivalintaa, amplifikaatiota ja funktion syntyä. Yhdistämällä dynaaminen kovalenttinen kemia ja amfifiilinen itsejärjestyminen kehitettiin useita järjestelmiä, jotka ilmentävät redox-herkkää fluoresenssisäätelyä, entropiavetoista amplifikaatiota ja pysyvää supramolekulaarista kiraalisuutta.

Lyhytketjuinen tetrafenyylieeteeniä (TPE) sisältävä amfifiili suunniteltiin toimimaan rakenteellisena templaattina ja fluoresoivana raportterina elävissä soluissa tapahtuvaa hapetusohjattua molekyyliverkoston muodostumista varten. Solunsisäinen hapetus edistää disulfidisidosten muodostumista, vahvistaa supramolekulaarista kokoonpanoa ja lisää fluoresenssia, kun taas pelkistys purkaa kokoonpanon ja vaimentaa fluoresoivaa vastetta, tarjoten mallin redox-säädellylle signaalinvälitykselle.

Toiseksi pitkäketjuinen TPE-amfifiili toimi supramolekulaarisena templaatina disulfidirakennuspalikoiden esiorganisoimiseksi dynaamisessa kombinatorisessa kirjastossa, mahdollistaen oktaameristen makrosyklien selektiivisen vahvistumisen. Doksorubisiinin kompleksaatio mahdollisti lääkeaineen vapautumisen reaaliaikaisen visualisoinnin aggregaatioindusoidun emission avulla, yhdistäen dynaamisen kombinatorisen kemian toiminnalliseen lääkeannosteluun ja optiseen luentaan.

Kolmannessa osatyössä natriumdodekyylisulfaattimikellit (SDS) toimivat ohimenevinä amfifiilisinä ympäristöinä, jotka muokkasivat dynaamisen kirjaston koostumusta. Eri SDS-pitoisuudet suosivat pentameeristen, heksameeristen tai trimeeristen makrosyklien amplifikaatiota. Pentameeri ilmensi selkeää supramolekulaarista kiraalisuutta ja säilytti kiraalisen vinoumansa mikellien poistamisen jälkeen, mikä osoittaa kiraalisen leimautumisen ja muistivaikutuksen.

Yhteenvetona tulokset osoittavat, että amfifiilinen templaatio on tehokas strategia adaptiivisen käyttäytymisen ja informaation varastoinnin ohjaamiseen dynaamisissa molekyyliverkostoissa.

ASIASANAT: Dynaaminen kombinatorinen kemia, Amfifiilinen templaatio, Tioli–disulfidinvaihto, Tetrafenyylieeni-amfifiilit, Natriumdodekyylisulfaattimikellit; Aggregaatioindusoitu emissio, Kiraalinen muisti

Table of Contents

Abbreviations

ACQ	aggregation-caused quenching
AIE	aggregation-induced emission
AIEgens	aggregate-induced emission luminogens
A. U.	arbitrary units
CAC	critical aggregation concentration
CDC	constitutional dynamic chemistry
CMC	critical micelle concentration
CLSM	confocal laser scanning microscopy
Con A	Concanavalin A
COSY	correlation spectroscopy
CPMG	Carr-Purcell-Meiboom-Gill
CTAB	cetyltrimethylammonium bromide
D	diffusion coefficient
DCC	dynamic combinatorial chemistry
DCL	dynamic combinatorial library
DCM	dichloromethane
DIPEA	N,N-diisopropylethylamine
DLC	drug loading content
DLE	drug loading efficiency
DLS	dynamic light scattering
DFT	density functional theory
DMF	dimethylformamide
DMSO	dimethyl sulfoxide
DOSY	diffusion-ordered spectroscopy
DOX	doxorubicin
DTT	dithiothreitol
EDC·HCl	N-(3-dimethylaminopropyl)-N′-ethylcarbodiimide hydrochloride
ESI	electrospray ionization
EtOH	ethanol
FC	flow cytometry
FE-SEM	field emission scanning electron microscopy

FITC	fluorescein isothiocyanate
FRET	Förster resonance energy transfer
FT-IR	Fourier-transform infrared spectroscopy
GSH	glutathione
HCl	hydrochloric acid
H_2O_2	hydrogen peroxide
HOBt	1-hydroxybenzotriazole hydrate
HPLC	high-performance liquid chromatography
LC-MS	liquid chromatography-mass spectrometry
MeCN	acetonitrile
MeOH	methanol
MS	mass spectrometry
MTT	3-(4,5-dimethylthiazol-2-yl)-2,5-diphenyl tetrazolium bromide
NHS	N-hydroxysuccinimide
NMR	nuclear magnetic resonance spectroscopy
NOESY	nuclear Overhauser effect spectroscopy
PBS	phosphate-buffered saline
PDA	photodiode array
P-gp	P-glycoprotein
PI	polyimide
PTFE	polytetrafluoroethylene
PXRD	powder X-ray diffraction
Q-TOF	quadrupole time of flight
Rh	hydrodynamic radius
RIM	restriction of intramolecular motions
ROS	reactive oxygen species
RP	reversed phase
SDS	sodium dodecyl sulfate
T_2	transverse NMR relaxation time
TEA	triethylamine
TMA	trimethylamine
TEM	transmission electron microscopy
TES	triethylsilane
TFA	trifluoroacetic acid
TLC	thin-layer chromatography
TPE	tetraphenylethene
TTAB	tetradecyltrimethylammonium bromide
UPLC	ultra-performance liquid chromatography
UV	ultraviolet

List of Original Publications

This dissertation is based on the following original publications, which are referred to in the text by their Roman numerals:

I **Yang, J.**, Wang, X., Wu, X., Lyu, Y., Papageorgiou, A. C., Mäkilä, E., Li, J. Oxidation Driven Synthetic Molecular Networks Enable Dynamic Assembly and Fluorescence Modulation in Living Cells. *Cell Reports Physical Science*, 2025; 6, 102922.

II **Yang, J.**, Wang, X., Wu, X., Lyu, Y., Papageorgiou, A. C., Li, J. Quantitative Synthesis of Dynamic Combinatorial Macrocycles Accelerated by Preorganization of AIEgens for Live Visualization of Drug Release. *Cell Reports Physical Science*, 2025; 6, 102355.

III **Yang, J.**, Wang, X., Li, J. Transient Micellar Environments Drive Self-Replication and Imprint Persistent Supramolecular Chirality. (manuscript)

1 Introduction

1.1 Systems Chemistry and Dynamic Molecular Networks

1.1.1 Systems chemistry: from static structures to adaptive networks

Systems chemistry seeks to understand how molecular components interact to produce behaviors that cannot be deduced from individual species in isolation. Rather than treating molecules as static structures with fixed functions, systems chemistry examines networks of reversible interactions that allow the system to redistribute, reorganize and adapt to environmental conditions. This perspective builds on the foundations of supramolecular chemistry, where noncovalent interactions demonstrated how molecular information can be encoded and amplified through self-assembly, as originally articulated by Lehn[1] and Whitesides[2]. Constitutional Dynamic Chemistry (CDC), introduced by Lehn, further established the conceptual basis for adaptive covalent networks (**Figure 1**).[3, 4] Early dynamic combinatorial chemistry studies by Sanders and co-workers established how reversible exchange processes enable template-directed amplification.[5-8] Subsequent work by Otto and co-workers revealed that dynamic networks can display emergent phenomena such as self-replication, pathway selection and adaptation to environmental cues.[9, 10]

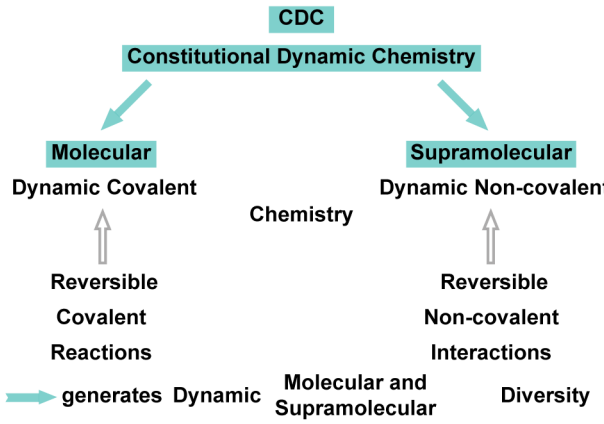

Figure 1. Constitutional dynamic chemistry (CDC) encompasses dynamic covalent chemistry (DCC) and supramolecular chemistry based on reversible covalent and noncovalent interactions. Adapted from ref. [4] with permission.

The central insight that arises from systems chemistry is that chemical behavior depends strongly on context. Interfaces, compartmentalization, gradients in polarity or redox state, and amphiphilic organization can each reshape reaction pathways and influence which molecular states become dominant. Grzybowski and co-workers highlighted how spatial constraints and feedback loops endow chemical systems with complex, history-dependent dynamics.[11, 12] This embedded perspective is essential for understanding how selective or adaptive phenomena arise in synthetic and biological systems. It also provides the guiding framework for the present thesis, which investigates how amphiphilic environments regulate the composition, assembly and function of dynamic disulfide networks.

1.1.2 Dynamic combinatorial chemistry as a systems chemistry toolbox

Dynamic combinatorial chemistry offers an experimental platform for implementing systems chemistry concepts.[13, 14] In a dynamic combinatorial library, building blocks interconvert through reversible covalent reactions, generating a continuously reorganizing mixture of species. The composition of this mixture reflects both intrinsic stability and the influence of external perturbations. Under thermodynamic control, the library amplifies species that best satisfy stabilizing interactions such as template binding or favorable packing, as demonstrated in early work on macrocyclic disulfide libraries by Sanders and co-workers.[7] Under kinetic influence, dynamic reaction networks may accelerate selected pathways or bias reaction fluxes, leading to transient or pathway-dependent outcomes, a principle illustrated in kinetic selection and self-replication experiments carried out in dynamic reagent pools by

Sadownik and Philp.[15] Although dissipative or fuel-driven non-equilibrium assemblies represent an important branch of systems chemistry, this thesis focuses on libraries designed to operate under thermodynamic control at the level of reversible exchange. The systems investigated in this thesis therefore operate within a thermodynamic framework, while recognizing that structured environments can impose persistent kinetic bias and give rise to long-lived metastable states without continuous energy input.[16]

The adaptability of dynamic libraries has enabled studies of recognition, molecular evolution and self-assembly. Importantly, dynamic libraries respond to subtle changes in their environment. Variations in pH, solvent polarity, compartmentalization or aggregation can shift equilibria or direct reaction pathways without altering the chemical identities of the building blocks. This context sensitivity makes dynamic libraries ideal tools for probing how amphiphilic structuring guides molecular selection. Environmental responsiveness in dynamic systems was established in early adaptive imine libraries reported by Giuseppone and Lehn[17], and later studies revealed how membrane interfaces or aqueous media can bias library composition and receptor amplification without altering the available building blocks.[18, 19] The amphiphile-templated environments examined in this thesis provide distinct modes of influence through compartmentalization, hydrophobic confinement or restricted mobility.

1.1.3 Dynamic covalent bonds in aqueous media

Dynamic covalent chemistry encompasses a range of reversible bond-forming reactions that typically operate under thermodynamic control and enable continuous molecular reorganization in solution. Several dynamic covalent reactions are compatible with aqueous environments, including imine formation, hydrazone and acylhydrazone exchange, oxime formation, disulfide exchange, as well as boronic ester, thioacetal, and thioester exchange (**Figure 2**).[8, 20, 21] Their reversibility under mild conditions allows library members to interconvert without loss of structural integrity, while the responsiveness of these reactions to pH, ionic strength and solvent polarity enables fine control over equilibration rates and product distributions.[21, 22] These water-compatible dynamic covalent processes provide a versatile foundation for constructing adaptive molecular networks in which reorganization occurs through reversible chemistry rather than covalent degradation. Representative aqueous dynamic combinatorial systems further illustrate how reversible covalent exchange can support higher-order structural behavior, including macrocycle stacking and supramolecular assembly under water-rich conditions.[23]

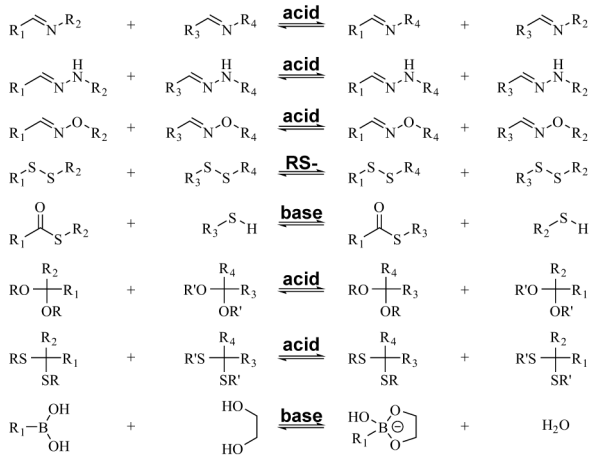

Figure 2. Representative reversible covalent reactions employed in dynamic combinatorial chemistry, including imine, hydrazone, oxime, disulfide, boronic ester, thioester, and thioacetal exchange reactions, illustrating the range of bond-forming processes used for the construction and reorganization of dynamic covalent libraries under thermodynamic control. Adapted from ref. [8, 20] with permission.

Beyond bulk aqueous solution, microenvironmental structuring significantly modulates dynamic covalent reactivity. Interfaces, vesicles, surfactant assemblies and compartmentalized aqueous domains can alter effective concentrations, stabilize selective intermediates or impose polarity and acidity gradients that bias exchange equilibria.[11, 12, 18] Dynamic covalent libraries and networks, including imine- and thioester-based systems, show pronounced shifts in composition and behavior under confined or amphiphilic conditions in which local environments differ markedly from bulk water.[17, 18, 24] These examples highlight the context sensitivity of aqueous dynamic covalent systems and establish the broader conceptual framework for later examining how specific reversible bonds such as disulfides respond to amphiphilic structuring and compartmentalization, as discussed in Section 1.3.

1.1.4 Thermodynamic and kinetic control in dynamic networks

Dynamic molecular networks exist at the intersection of thermodynamics and kinetics. Under equilibrium conditions, the most stable species are amplified.[8, 25] However, in structured or heterogeneous environments, kinetic effects often play a critical role. Restricted diffusion, localized concentration gradients or interfacial preorganization can limit access to certain conformations or transition states.[11, 12] As a result, networks may favor metastable or pathway-dependent products rather than

the global energy minimum, reflecting the broader energy-landscape perspective of supramolecular systems chemistry.[10, 26]

Understanding how thermodynamic and kinetic influences interplay is essential for interpreting the systems studied in this thesis. In intracellular environments, redox gradients and amphiphilic compartmentalization can bias the formation and reorganization of dynamic covalent networks.[10, 11, 27] In AIE-based aggregates, restricted intramolecular motion and hydrophobic confinement create local environments that can influence oxidation processes and favor macrocycle formation.[28, 29] In micellar and compartmentalized dynamic combinatorial systems, nanoscale domains guide reaction pathways and enable selective amplification and pathway-dependent network behavior.[18, 30] These processes illustrate how amphiphilic organization imposes structure on dynamic covalent chemistry, resulting in emergent behavior that cannot be explained by the molecular building blocks alone.

1.2 Template Effects in Dynamic Combinatorial Libraries

1.2.1 Principles of templation in dynamic networks

Template effects lie at the heart of dynamic combinatorial chemistry. In a dynamic library, building blocks continuously exchange through reversible reactions, giving rise to an ensemble of interconverting species. Although these species differ in stability, their relative populations can be markedly reshaped by the presence of a template that selectively stabilizes particular arrangements (**Figure 3**).[31, 32] Foundational studies by Sanders and Otto established that metal ions, small molecules or supramolecular receptors can bias dynamic equilibria by preferentially binding complementary library members, leading to their amplification.[8, 33] In aqueous disulfide systems, West and Otto established a baseline by showing that cysteine-derived cages and interlocked architectures can form spontaneously in untemplated dynamic combinatorial libraries under thermodynamic control.[34] In subsequent studies, Corbett and Otto demonstrated that introducing guest molecules as templates biases these equilibria, leading to selective amplification of receptors that best complement the guest.[35] These studies collectively show that templation translates molecular recognition events into compositional control in dynamic networks.

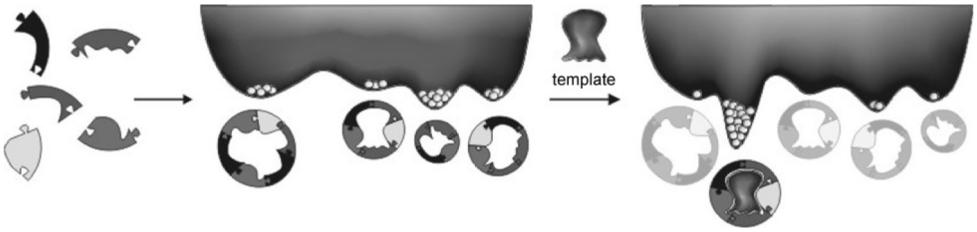

Figure 3. Schematic illustration of a dynamic combinatorial library composed of bifunctionalized building blocks forming multiple macrocyclic species. The relative abundance of individual library members is governed by their thermodynamic stabilities, represented by the free-energy landscape. Selective binding of a guest or template stabilizes one macrocycle and shifts the equilibrium toward its amplification at the expense of other library members. Reprinted from ref. [36] with permission.

A fundamental role of templation is to introduce external information into a reversible system. Rather than relying solely on the intrinsic energetic preferences of the building blocks, the network becomes responsive to an imposed set of interactions, which may include hydrogen bonding, electrostatic complementarity, hydrophobic partitioning, or geometric confinement. Anion-templated macrocyclizations reported by Alfonso and co-workers illustrate how charge and shape complementarity can strongly bias imine-based dynamic covalent systems toward specific pseudopeptidic macrocycles, even when these architectures are otherwise disfavored.[37] Protein-directed DCC, summarized by Canal-Martin and Pérez-Fernández, further exemplifies how biomolecular receptors act as highly selective templates that amplify their strongest binders in situ.[38] Beyond molecular hosts, amphiphilic assemblies can also impose templating effects: Hunter and co-workers showed that lipid vesicles modulate product distributions by differential partitioning of dynamic covalent intermediates at bilayer interfaces.[39] In a more complex biological context, Alfonso and collaborators demonstrated that whole living cells can act as effective templating environments, selectively amplifying imine-based polyamines that interact with extracellular matrix components.[40] Across these diverse examples, templation enables the programmed selection of architectures that are not necessarily favored in the untemplated equilibrium distribution.

Templation also underpins adaptive behavior, a central concept in systems chemistry. When environmental variables such as chemical fuel, pH, redox state or template availability fluctuate, dynamic libraries reorganize in response. Otto and co-workers showed that self-replicating disulfide macrocycles can undergo competitive amplification linked to supramolecular aggregation, a behavior later conceptualized as adaptive in dynamic molecular networks.[7, 13] Boekhoven and co-workers extended templation into the non-equilibrium regime by demonstrating that chemically fuelled dynamic libraries can undergo transient, template-based copying

processes operating under kinetic control.[41] Leclaire and co-workers further demonstrated that environmental inputs such as CO_2 can act as reversible selection pressures that reorganize multicomponent dynamic networks.[42] Meanwhile, Dumartin and Vial illustrated that subtle variations in guest identity or redox conditions can reorganize disulfide-based dynarene networks, revealing a higher level of adaptivity and structural complexity than previously assumed.[43] Such examples highlight that templation not only directs equilibrium speciation but also governs how dynamic networks evolve under feedback, thereby forming the conceptual foundation for understanding the amphiphile-mediated selection phenomena discussed later in this thesis.

1.2.2 Thermodynamic selection versus kinetic catalysis

Template effects may operate under thermodynamic or kinetic control. Under thermodynamic control, the template preferentially stabilizes the ground state of a particular library member. Stabilization may arise from specific binding interactions or from improved packing and solvation around the template-bound structure. Because dynamic covalent bonds allow continuous exchange, the system eventually reaches equilibrium where the most stabilized species becomes the dominant product. This classical mode of templation has been widely exploited for macrocycle discovery and selective receptor amplification. For example, Mandolini group demonstrated that transacetalation-based cyclophane libraries respond strongly to metal-ion templates, with Ag^+ selectively amplifying a specific cyclophane dimer under thermodynamic control.[44] Similar thermodynamic templation governs many imine- and disulfide-based macrocycles reported in earlier work.[8, 33]

In contrast, templates may also influence dynamic libraries through kinetic pathways. Kinetic templation occurs when the template accelerates the formation of particular species by stabilizing transition states or reactive intermediates. Even when the templated structure is not the global energy minimum, pathway-selective catalysis may allow it to accumulate as a metastable product. Philp and co-workers have shown that replicator networks often exhibit such kinetic selection, where catalytic connectivity and pathway competition drive amplification under non-equilibrium conditions.[45] Lehn and co-workers further demonstrated that metal coordination can impose high-energy strained conformations in imine macrocycles; upon demetallation these activated species follow defined kinetic pathways to rearrange into more stable architectures, illustrating how templates can shape reactivity by accessing high-energy states.[46] These examples highlight that kinetic templation can introduce history dependence and pathway selectivity not captured by equilibrium thermodynamics alone.

In amphiphilic settings, thermodynamic and kinetic effects frequently coexist and may be coupled. Hydrophobic confinement can simultaneously stabilize particular macrocycles and accelerate their formation. Interfaces restrict the mobility and orientation of reactive species, steering the system toward specific topologies. Vesicle-templated dynamic covalent chemistry and bilayer-associated exchange processes illustrate how partitioning and spatial organization modify both equilibria and reaction rates.[18, 30] Enzymatic dynamic combinatorial systems provide particularly clear examples: Beeren and co-workers showed that cyclodextrin glucanotransferase-mediated mixtures of linear and cyclic glucans behave as transient out-of-equilibrium libraries in which templates selectively stabilize kinetically trapped cyclodextrins.[47] Subsequent work demonstrated that ionisable templates enable pH-dependent switching between α- and β-cyclodextrin formation, underscoring the role of environmental variables in tuning the balance between thermodynamic and kinetic control.[48] Understanding how these influences merge in amphiphilic environments is therefore essential for interpreting the complex selection behaviors explored later in this thesis.

1.2.3 Classes of templates in DCC

1.2.3.1 Small-molecule templates

Small-molecule templates constitute the earliest and most extensively developed class in DCC. Metal ions, anions and polyamines can impose strong structural preferences on dynamic networks. Mandolini and co-workers demonstrated that Ag^{+} selectively amplifies a cyclophane dimer in a formaldehyde-acetal library, establishing metal-ion-mediated selectivity within fast-exchanging systems.[44] Au-Yeung and co-workers showed that Cu^{+} and Cu^{2+} direct phenanthroline-based DCLs toward [2]catenanes that do not form in the absence of metal templates.[49] Lisowski and co-workers used Cd^{2+} to convert a 2+2 macrocycle into a larger 6+6 container, illustrating metal-controlled reshaping of dynamic imine macrocycles.[50]

Anionic templates have also been widely exploited. Alfonso and co-workers used terephthalate and related dicarboxylates to template pseudopeptidic macrocycles.[37] They further demonstrated that geometrically disfavored macrocycles can still form selectively when the anion provides sufficient preorganization.[51] In a size-selective dynamic combinatorial system developed by Jurczak and co-workers, deprotonated carboxylates were shown to act as discrete anionic templates that bias oligomacrocycle size selection (**Figure 4A**).[52] Ballester and co-workers showed that polar interior guests can direct the assembly of dynamic covalent capsules by stabilizing specific capsular geometries.[53] Stoddart's work on

acetal-based crown ether architectures illustrated how small-molecule geometry can enforce high levels of chiral amplification.[54]

Cationic small-molecule templates represent a complementary mode of molecular templation. Biogenic polyamines such as spermine selectively amplify complementary macrocyclic receptors through multivalent electrostatic interactions, reflecting the ability of flexible, multicationic guests to bias dynamic combinatorial equilibria toward hosts that maximize charge compensation and binding cooperativity.[8, 55] In related systems, amines, ammonium and quaternary ammonium salts, including adamantylammonium derivatives, act as shape-defined cationic templates whose size and rigidity further bias library distributions toward matching host architectures (**Figure 4B**).[56, 57]

These examples highlight the power of small molecules to impose precise recognition constraints on DCLs, though their rigid binding modes limit adaptability relative to larger biological or supramolecular environments.

1.2.3.2 Macromolecular and biomolecular templates

Macromolecular templates introduce multivalency, conformational flexibility and hierarchical binding surfaces unavailable to small molecules. The Lehn and co-workers showed that lectins such as Con A can selectively amplify mannose-containing disulfide macrocycles from complex libraries, demonstrating protein-driven templation in carbohydrate recognition.[58] Leclaire and co-workers expanded this concept to bacterial, demonstrating selective amplification of glyco-dyn[n]arenes with nanomolar affinity.[59]

Macromolecular templation has also been applied to enzymatic systems. Beeren and co-workers demonstrated that cyclodextrin glucanotransferase generates a transient glucan DCL whose composition can be directed toward α-, β-, γ- or δ-cyclodextrins through added templates or pH-responsive ionisable guests.[47, 48] More recent studies further showed that bolaamphiphile and azobenzene templates can direct the selective formation of large-ring cyclodextrins or modulate product distribution via photoswitching (**Figure 4C**).[60, 61] In medicinal chemistry, Hirsch and co-workers used target-directed DCC to identify inhibitors of bacterial glucosyltransferase GTF180 and the essential metabolic enzyme 1-deoxy-D-xylulose-5-phosphate synthase.[62, 63] Reviews by Pérez-Fernández and co-workers summarize how proteins and nucleic acids operate as thermodynamic selectors in DCLs.[64]

Synthetic macromolecules can also serve as emergent templates. In our group's work on single-chain polymer folding, the polymer's evolving conformation created internal cavities that selectively stabilized disulfide-based crosslinkers generated within the DCL, providing an example of self-induced macromolecular templation arising from structural dynamics rather than predefined binding sites.[65]

1.2.3.3 Supramolecular and interfacial templates

Supramolecular assemblies occupy an intermediate level between molecular and macromolecular templates. Their influence arises from mesoscale organization, such as compartmentalization, local concentration gradients and restricted mobility. Hunter and co-workers demonstrated that vesicle bilayers can bias a dynamic Michael-addition library toward a single dominant product via differential partitioning (**Figure 4D**).[39] Otto and co-workers showed that surfactant-derived compartments and bilayer interfaces reshape disulfide-based DCLs, stabilizing specific macrocycles or enabling supramolecular architectures inaccessible in bulk solution.[18, 30]

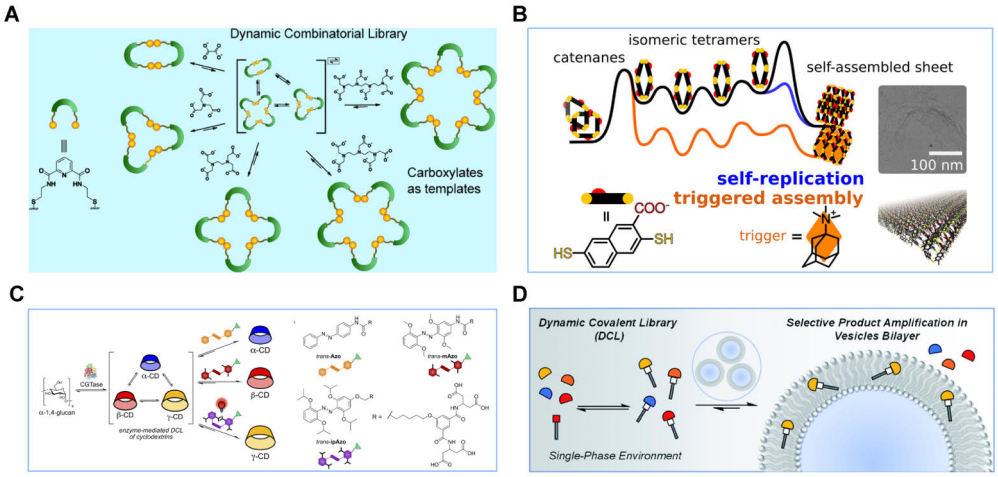

Figure 4. Representative examples of template effects in dynamic combinatorial libraries. (A) Anionic carboxylate templates selectively amplify specific disulfide-based macrocycles through molecular recognition. (B) Cationic templates induce selective amplification by promoting self-assembly and triggering self-replication. (C) Enzymatic processing generates a dynamic combinatorial library whose composition is subsequently directed by small-molecule organic templates under external control. (D) Vesicle lipid bilayers function as spatial templates that modulate library composition through interfacial partitioning effects. Panels (A) and (B) reprinted from refs. [52, 56] with permission. Panels (C) and (D) reproduced from ref. [61] and ref. [39] under the Creative Commons Attribution 3.0 (CC BY 3.0) licence.

1.2.4 Amphiphilic templation as a distinct mode of environmental control

Amphiphilic templation represents a form of environmental control that originates primarily from the collective behavior of self-assembled amphiphiles rather than from discrete molecular recognition. Assemblies such as micelles, vesicles, coacervates and soft nanodomains generate sharp spatial variations in polarity,

hydration and mobility. Dynamic covalent reactions that occur within or near these environments experience altered local concentrations, restricted conformational freedom and micro-equilibria that differ substantially from bulk solution. These mesoscale features can shift macrocycle distributions, stabilize otherwise inaccessible species or couple covalent exchange to compartment formation, as demonstrated in disulfide-based surfactant libraries and other unconventional amphiphilic systems.[30]

Synthetic systems chemistry expands these concepts into controllable laboratory platforms. Fletcher and co-workers reported micellar systems capable of self-reproduction that modulate downstream reactivity,[66, 67] illustrating how amphiphile-driven autocatalytic networks can be integrated with broader chemical functions. Amphiphilic amino-acid derivatives have also been used to regulate imine polymerization and crystallization in water by forming micelles that act as dynamic barriers during the growth of single-crystal covalent organic frameworks.[68] In parallel, our group has shown that a disulfide-based dynamic combinatorial library, when combined with a cationic amphiphilic pyridinium template and a hydrophobic drug, selectively amplifies an octameric macrocycle that co-assembles into high-loading nanorods, directly coupling dynamic covalent selection with amphiphile-driven nanostructure formation.[69] Collectively, these findings highlight amphiphilic templation as an adaptable mesoscale mechanism capable of shaping dynamic molecular networks in ways inaccessible to classical molecular templates.

1.3 Disulfide-Based Dynamic Combinatorial Libraries

1.3.1 Rationale for using disulfide chemistry

Disulfide exchange represents one of the most versatile and robust dynamic covalent reactions for constructing adaptive molecular networks in aqueous environments. Its distinctive value arises from the balance between reversibility and stability: disulfide bonds maintain structural integrity under physiological conditions while undergoing rapid thiolate-mediated exchange that enables continuous network reconfiguration. Fundamental studies have shown that reversible disulfide exchange is sensitive to weak noncovalent interactions, allowing supramolecular environments to modulate exchange pathways and influence constitutional outcomes.[70] This interplay between covalent adaptability and supramolecular responsiveness provides a mechanistic basis for employing disulfide motifs in reconfigurable molecular architectures, including reversible polymerizations and dynamic materials.[71, 72]

A second advantage of disulfide chemistry is its pronounced responsiveness to redox conditions. Because thiols and disulfides interconvert through oxidation and reduction, redox gradients can reorganize dynamic library compositions, regulate macrocycle formation, or trigger reversible assembly–disassembly transitions. Such behavior is particularly significant in biological environments, where glutathione levels, mitochondrial reactive oxygen species (ROS), and compartmentalized redox processes can continuously reorganize disulfide-containing networks.[73, 74] These features make disulfide exchange a powerful mechanism for programming redox-adaptive behavior, especially in intracellular settings relevant to this thesis.

A third reason for the extensive adoption of disulfide exchange in dynamic systems is its compatibility with supramolecular and amphiphilic organization. Hydrophobic interactions, microphase separation and amphiphile-rich interfaces strongly influence thiol–disulfide reactivity by altering local polarity, thiolate availability and effective concentration.[18, 30] Amphiphilic environments such as micellar and interfacial assemblies reorganize local polarity, effective concentration and aggregation behavior, thereby modulating the constitutions and exchange equilibria of dynamic covalent systems.[30] Such sensitivity enables disulfide-based libraries to function as probes of microstructural organization and provides a tractable platform for investigating how amphiphiles direct the evolution of adaptive molecular networks, which constitutes a central conceptual foundation for this thesis.[75]

1.3.2 Thiol–disulfide exchange mechanisms

Thiol–disulfide exchange occurs through nucleophilic attack of a thiolate on a disulfide bond, forming a new disulfide and a new thiolate species. This process is reversible and strongly pH dependent, as thiolate formation increases at neutral to basic pH and is suppressed under acidic conditions. Foundational studies by Sanders and Otto demonstrated that thiolate availability governs exchange rates in aqueous dynamic combinatorial libraries, establishing pH as a key experimental control parameter.[7, 8]

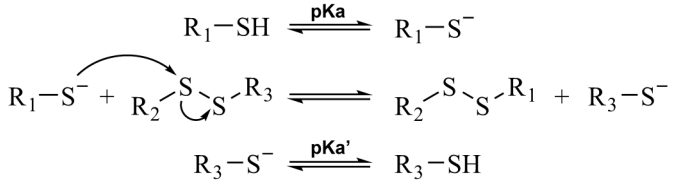

Figure 5. Thiolate–disulfide exchange mechanism. The reversible exchange proceeds through nucleophilic attack of a thiolate on a disulfide bond and is controlled by thiolate availability and pH. Adapted from ref. [70] with permission.

Disulfide bonds required for exchange processes are typically generated through oxidation of thiols, for example by dissolved oxygen or reactive oxygen species. In both biological and synthetic contexts, however, the adaptive behavior of disulfide-based systems is governed by subsequent thiolate-mediated exchange rather than by the specific oxidative pathways involved. In dynamic combinatorial libraries, oxidized mixtures of linear and cyclic disulfides therefore equilibrate through exchange reactions, and the resulting macrocycle distribution reflects thermodynamic selection within the exchange network. Such behavior has been demonstrated in supramolecularly influenced disulfide systems, selenocystine-accelerated libraries, and protein- or enzyme-directed selection processes (**Figure 5**).[70, 76]

Local polarity and hydrophobicity further modulate thiol–disulfide exchange by influencing thiolate accessibility and the stability of exchange intermediates. In micelles and amphiphilic polymer aggregates, hydrophobic substrates can partition into compartmentalized environments that alter local concentration, solvation, and conformational freedom, enabling exchange pathways that are inefficient or inaccessible in bulk aqueous solution. Outside the context of dynamic combinatorial libraries, redox-responsive AIE-active systems illustrate how disulfide-linked structural reconfiguration can be coupled to higher-order organization and spatial confinement, without relying on explicit modulation of oxidative pathways.[77-79] Together with reports of surfactant-templated macrocycle amplification, these observations underscore the utility of disulfide exchange as a probe for understanding how amphiphilic environments direct dynamic covalent evolution.[30, 39]

1.3.3 Structural diversity and supramolecular behavior

Disulfide-based dynamic libraries display substantial structural diversity, arising from oxidative macrocyclization that generates rings of different sizes. The distribution of these macrocycles responds sensitively to redox conditions, solvent composition, ionic strength and the presence of amphiphilic components. These dependencies illustrate the intimate connection between molecular reactivity and supramolecular environment, as demonstrated in aqueous disulfide libraries, disulfide cages and other adaptive macrocyclic systems.[34, 70] In addition, recent studies have shown that dynamic covalent systems can give rise to folded macrocycles with intrinsically low symmetry when monomer interactions favor uniquely stabilized conformational states, including architectures containing a prime number of building units.[80]

Many disulfide macrocycles possess amphiphilic elements that promote their organization into higher-order structures such as fibres, ribbons, sheets, nanotubes and vesicle-like assemblies. Within dynamic libraries, the formation of ordered aggregates can selectively stabilize specific macrocycle sizes or topologies and thereby bias the overall equilibrium. This phenomenon has been reported in

disulfide-based macrocyclic systems and plays a role in adaptive amplification within dynamic networks.[7, 70] Studies on dynamic covalent macrocycles designed for gene and drug co-delivery, as well as investigations of disulfide-bridged hybrid nanoparticles, further demonstrate how subtle differences in connectivity and topology translate into distinct supramolecular morphologies.[81]

Amphiphilic environments introduce an additional level of structural control by confining dynamic species within locally ordered microdomains. Micelles and vesicles impose orientational and spatial restrictions, whereas aggregation-induced emission assemblies generate hydrophobic regions that enhance the stability of particular disulfide structures according to their solvation compatibility. These effects have been observed in vesicle-organized dynamic covalent systems and in libraries formed within surfactant-based compartments.[30, 39] Such mechanisms form the conceptual basis for the amphiphile-guided systems examined in Sections 3.2 and 3.3 of this thesis and illustrate how disulfide macrocycles can support the emergence of ordered structures in spatially organized aqueous media.

1.3.4 Functional relevance and applications

The environmental sensitivity and reversible nature of disulfide chemistry underpin a broad range of functional applications. Because thiol–disulfide exchange is directly coupled to local redox fluctuations, disulfide-containing assemblies can operate as reporters of oxidative or reductive events in complex media. When combined with luminogens whose emission responds to changes in supramolecular organization, such as aggregation-induced emission (AIE) chromophores, these dynamic networks become powerful probes for intracellular redox behavior.[28, 82]

Beyond sensing, dynamic disulfide networks can exhibit adaptive reconfiguration when exposed to heterogeneous or amphiphilic environments. Exchange pathways may become kinetically biased, enabling the transient stabilization of macrocycles or architectures disfavored under bulk equilibrium conditions. The pathway dependence and context sensitivity of disulfide-based DCLs illustrate how mesoscale structuring and restricted diffusion can generate persistent or memory-like states.[70] These phenomena provide an important conceptual bridge between classical dynamic combinatorial chemistry and the amphiphile-templated molecular evolution examined in this thesis.

Disulfide-containing assemblies also play a significant role in drug delivery and therapeutic materials (**Figure 6**). Their reversible chemistry enables structurally encoded responses to reductive intracellular environments and facilitates controlled disassembly or release events. Dynamic covalent design principles have become increasingly prominent in delivery systems, particularly for enabling triggered activation or for coupling structural rearrangement to functional output.[81, 83] Among

these developments, the extensive work of Ryu and co-workers stands out in demonstrating that redox- or enzyme-triggered intramitochondrial polymerization or oligomerization of disulfide-containing monomers can induce context-specific modulation of cell fate, enabling potent anticancer or senolytic responses (**Figure 6C**).[84-90] These findings highlight how disulfide-mediated adaptive growth processes, operating within compartmentalized and redox-regulated environments, can produce emergent therapeutic behaviors that are difficult to achieve with conventional carriers.

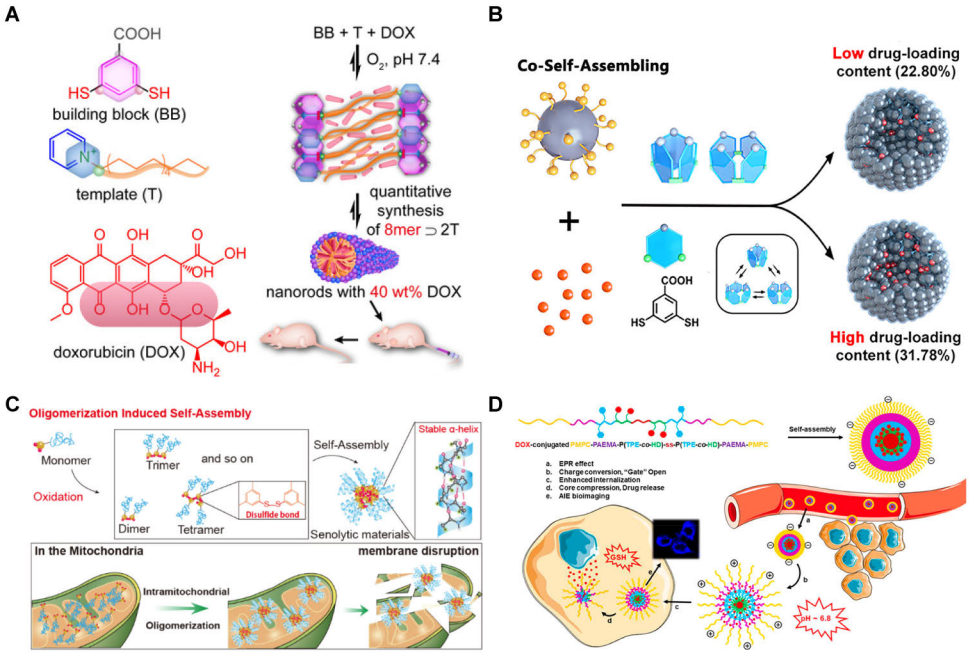

Figure 6. Functional self-assembled systems enabled by disulfide chemistry and redox-responsive design. (A) Thermodynamically controlled disulfide exchange within a dynamic combinatorial library enables template-directed co-assembly involving amphiphilic building blocks and drug molecules, yielding responsive nanocarriers. (B) Kinetically biased *in situ* thiol–disulfide exchange gradually generates self-assembling species that trigger controlled co-self-assembly into stable nanosystems. (C) Redox-triggered intracellular disulfide oligomerization drives selective self-assembly of peptide-based nanostructures in confined cellular environments. (D) pH- and redox-responsive disulfide-containing polymeric micelles enable adaptive assembly, controlled disassembly, and signal-reporting functionality. Panels (A), (C) and (D) were reprinted from refs.[69, 88, 91] with permission. Panel (B) reprinted from ref.[92]

AIE-active disulfide carriers further enrich this design space by providing simultaneous cargo delivery and fluorescence reporting. Redox-responsive micelles, nanogels, and macrocyclic assemblies have been developed to monitor drug release through changes in AIE or FRET signals while maintaining selective disassembly

profiles in the presence of intracellular glutathione (**Figure 6D**).[77, 91] This multifunctional behavior parallels the results of Section 3.2, where AIE aggregates not only template the formation of specific macrocycles but also act as optically traceable nanostructures enabling controlled drug loading, release.

Overall, disulfide-based dynamic combinatorial libraries represent a chemically versatile and environmentally responsive platform for studying emergent molecular behavior. Their compatibility with redox biology, ability to integrate with amphiphilic structuring, and capacity to support signal-transducing supramolecular assemblies make them uniquely suited for exploring amphiphile-guided molecular evolution. These attributes motivate the transition to the next section, which examines how AIEgens serve as both amphiphilic organizers and optical reporters within dynamic disulfide systems.

1.4 Aggregation-Induced Emission (AIE) as a Dual-Function Module

1.4.1 Photophysical foundations of AIE

Aggregation-Induced Emission (AIE) was first reported by Tang and co-workers in 2001 for 1-methyl-1,2,3,4,5-pentaphenylsilole, revealing that certain non-planar luminogens become highly emissive upon aggregation despite being weakly fluorescent in dilute solution.[93] This observation sharply contrasted the aggregation-caused quenching (ACQ) behavior typical of planar π-conjugated dyes, which was rationalized within early exciton theory.[94] As the field developed, tetraphenylethene (TPE) and its derivatives emerged as the most widely studied archetypal AIEgens due to their structural simplicity and conformational freedom. This enabled systematic elucidation of AIE photophysics and the establishment of the restriction of intramolecular motions (RIM) mechanism.[95, 96] Modern excited-state analyses further show that aggregation or conformational locking reduces access to non-radiative decay channels, including conical intersections, thereby stabilizing radiative pathways.[97, 98] Recent studies also highlight how aggregate morphology, supramolecular topology, and dynamic covalent environments tune molecular rigidity and modulate AIE output.[99, 100]

1.4.1.1 Aggregation-caused quenching vs AIE

Traditional planar fluorophores frequently exhibit ACQ because strong π–π stacking promotes non-radiative decay or excimer formation.[101, 102] In contrast, AIEgens are intrinsically non-planar and flexible; therefore, they show weak emission in solution where intramolecular motions dominate excited-state deactivation. Aggregation

restricts these motions and suppresses non-radiative pathways, producing pronounced fluorescence enhancement.[95, 96] The opposite behaviors of ACQ dyes and AIEgens thus arise from fundamentally different relationships between intermolecular packing and intramolecular dynamics.

1.4.1.2 Restriction of intramolecular motion

The restriction of intramolecular motion (RIM) provides the unified mechanistic basis for AIE. In dilute solution, low-frequency rotations and torsions create efficient internal conversion channels, often via facile access to conical intersections.[97, 98] Aggregation constrains these motions, reshaping the excited-state potential energy surface, suppressing non-radiative decay, and favoring emissive pathways.[95, 96] TPE derivatives exemplify this behavior, with numerous studies demonstrating how conformational restriction amplifies fluorescence.[96, 103] Beyond simple aggregation, supramolecular confinement and dynamic covalent interactions can impose additional rigidity and thereby modulate AIE responses, enabling adaptive control of emission in structured chemical environments.[100]

1.4.2 Supramolecular behavior of AIEgens

AIEgens frequently possess amphiphilic or partially amphiphilic structures that promote aggregation into well-defined supramolecular assemblies. Depending on the balance between hydrophobic, π-conjugated, and charged segments, AIE molecules can form nanoparticles, vesicles, micelles, or elongated fibers. These architectures generate distinct local polarity, hydration, and mobility, thereby influencing both optical output and chemical reactivity within the aggregated state.[96, 104]

In dynamic covalent systems, AIE aggregates can modulate reaction pathways by altering molecular orientation, restricting conformational freedom, or concentrating reactants within hydrophobic nanodomains. These effects become particularly important when reversible reactions depend on local dielectric environment or steric accessibility, as in thiol–disulfide exchange.[70, 100] Because the internal organization of AIE assemblies is sensitive to concentration, pH, and ionic strength, these aggregates introduce a tunable form of environmental structuring, which is critical for directing the equilibria and selectivity of dynamic covalent bond exchange.[99, 105, 106]

AIE aggregates also exhibit cooperative assembly behavior, where subtle differences in packing lead to large emission changes. This property has been applied to monitor supramolecular polymerization, conformational transitions, and real-time rearrangement processes.[96, 107, 108] In dynamic libraries, the emission response provides a built-in readout of network evolution, enabling AIEgens to function

simultaneously as structural organizers and reporters.[100, 109, 110] These concepts and representative examples are summarized in **Figure 7**.

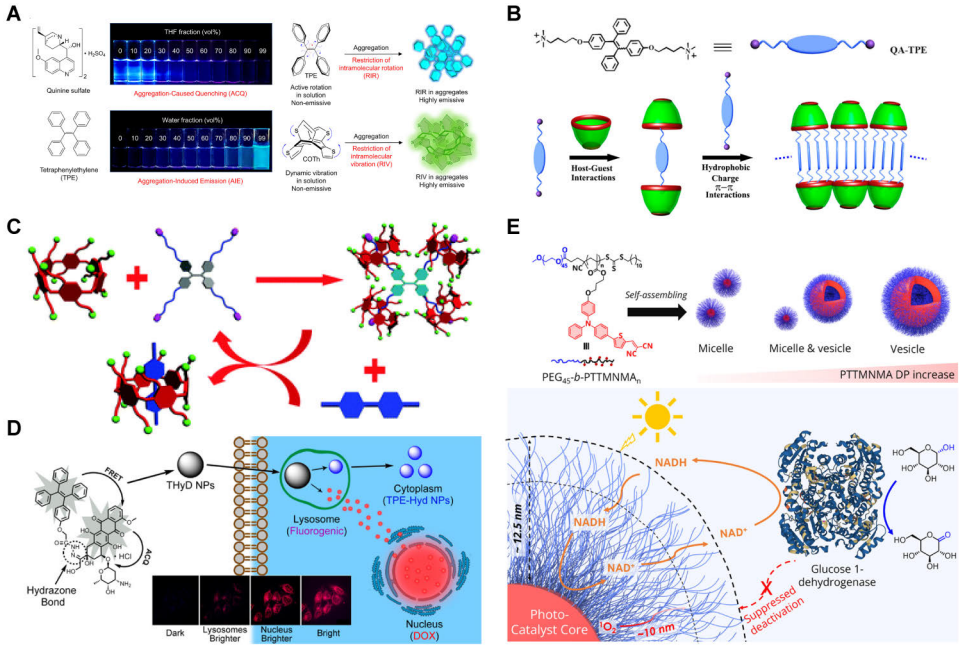

Figure 7. Aggregation-induced emission (AIE) as a photophysical and supramolecular module for functional systems. (A) Comparison between aggregation-caused quenching (ACQ) and aggregation-induced emission (AIE), illustrating how restriction of intramolecular motion (RIM) activates fluorescence upon aggregation in non-planar luminogens such as tetraphenylethene. (B) and (C) Supramolecular regulation of AIE through host–guest interactions, where macrocycles induce aggregation, restrict intramolecular motion, and enable stimulus-responsive fluorescence switching or sensing. (D) AIE-based fluorescent prodrug systems in which aggregation state and energy-transfer processes report intracellular drug release and trafficking with high spatiotemporal resolution. (E) Amphiphilic AIE-active polymer micelles and vesicles functioning as confined reaction media, enabling photochemical processes while simultaneously providing optical readout and protection of sensitive biological components. Panel (A) reproduced from ref. [111] under the CC BY-NC-ND License. Panel (B) assembled from two figures in ref. [112] and reproduced with permission. Panels (C)-(E) reproduced from refs. [113-115] with permission.

1.4.3 AIEgens as functional scaffolds for sensing and reactive preorganization

Beyond acting as fluorescent probes, aggregation-induced emission (AIE) luminogens can serve as amphiphilic scaffolds that generate confined microenvironments capable of modulating dynamic covalent processes.[100, 115] Upon aggregation, hydrophobic AIE domains give rise to localized substrate enrichment and restricted conformational

freedom, features that favor thiol–disulfide oxidation, exchange, and macrocyclization by reducing entropic penalties and stabilizing reactive conformations.[70] Such aggregation-induced preorganization provides a mechanistic basis for the templation effects explored in Section 3.2 of this thesis.[70, 100]

In parallel, AIEgens offer powerful opportunities for in situ monitoring and kinetic profiling of dynamic combinatorial libraries. Because emission intensity directly reflects aggregation state, temporal changes in reaction kinetics, macrocycle distributions, and supramolecular topology can be followed continuously under operational conditions, avoiding reliance on interrupted sampling.[96, 116, 117] In biological environments, AIE-based conjugates have been widely used as redox- and thiol-triggered imaging probes, enabling low-background visualization of intracellular thiol/disulfide-related processes and adaptive aggregation behavior.[118, 119] This capability is further exemplified by the system developed in Sections 3.1 and 3.2.

Aggregation-induced rigidity couples mesoscale amphiphilic organization to molecular-level reaction pathways, providing a versatile platform for understanding how supramolecular preorganization governs the adaptive behavior of dynamic covalent networks.[95, 99]

1.5 Amphiphilic Environments as Dynamic Templates

1.5.1 Environmental structuring effects on dynamic covalent chemistry

Amphiphilic environments generate structured, heterogeneous landscapes that strongly influence molecular behavior by reshaping solvation, mobility and local concentration profiles within soft assemblies such as micelles, vesicles and interface-rich domains. [2] Within supramolecular and dynamic covalent chemistry, these environments can be viewed as adaptive reaction media in which reversible bond formation and molecular recognition are coupled to mesoscale organization. [8, 33] Upon self-assembly, surfactants and related amphiphiles create polarity gradients and confined hydrophobic regions that modulate reaction kinetics and equilibria through changes in effective molarity, transition-state stabilization and conformational flexibility.[120]

In the context of dynamic combinatorial chemistry (DCC), where library composition emerges from the interplay between thermodynamic stability and exchange kinetics, such environmental structuring provides a means of biasing molecular populations.[8, 13] Hydrophobic confinement and reduced conformational freedom can favor macrocyclic architectures that are disfavored in bulk aqueous

solution by lowering entropic penalties or restricting the accessible conformational space.[7, 70] At the same time, the curvature, packing and internal dynamics of amphiphilic aggregates govern the partitioning of reactive species between aqueous and interfacial regions, thereby reshaping the effective energy landscape of exchange reactions.[18, 30]

More generally, soft, dispersed and interface-rich aqueous systems have been shown to promote and channel chemical reactivity by combining local concentration effects, compartmentalization and non-uniform solvent properties.[121] These observations underscore that reactivity in amphiphilic systems cannot be fully understood at the level of individual molecules alone, but instead emerges from the coupling between reversible chemistry and mesoscale organization. As such, environmental structuring represents a central principle by which amphiphilic assemblies act as dynamic templates capable of directing selection and adaptation within dynamic covalent networks.

1.5.2 Amphiphilic systems explored in this thesis

1.5.2.1 Surfactant micelles: confinement-driven selection, memory and chirality

Surfactant micelles represent one of the simplest and most extensively studied amphiphilic environments. In aqueous solution, they form dynamic nanoscale aggregates with hydrophobic cores and hydrophilic coronas, leading to strong partitioning of hydrophobic or aromatic species and pronounced changes in local polarity and microviscosity.[120, 122, 123] Such microenvironmental effects have been classically probed using pyrene-based photophysical reporters, where changes in monomer and excimer emission provide direct evidence for altered local organization within micellar assemblies (**Figure 8A**).[123-125]

Beyond static confinement, micelles are inherently dynamic, with molecular exchange and morphology that are highly sensitive to surfactant composition, concentration and external conditions.[126, 127] Variations in curvature, packing and charge balance, particularly in mixed or catanionic surfactant systems, give rise to a range of aggregate structures, each associated with distinct interfacial properties and degrees of confinement.[122, 128] These features allow micelles to function as adaptive reaction compartments.

In the context of thiol–disulfide exchange and related dynamic covalent reactions, micellar confinement reduces conformational freedom and increases effective local concentrations of reactive building blocks, thereby shifting equilibria between linear oligomers and macrocyclic species relative to bulk aqueous solution.[70, 120] More generally, soft, interface-rich micellar systems have been shown to promote

multistep and cascade transformations by combining hydrophobic effects with controlled compartmentalization, highlighting the capacity of micelles to bias reaction pathways through environmental structuring.[121, 129]

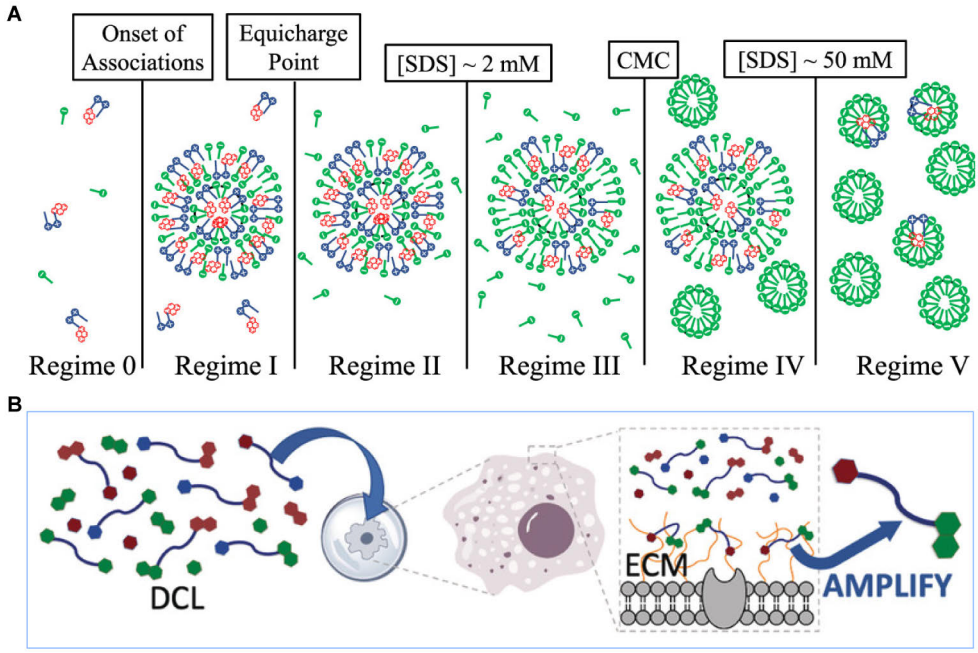

Figure 8. Amphiphilic environments as templates for molecular organization. (A) Regime-dependent self-assembly of oppositely charged surfactants, illustrating how amphiphilic aggregation generates structured, heterogeneous microenvironments with distinct interfacial properties. (B) Application of amphiphilic templation in dynamic combinatorial chemistry, where whole living cells act as complex templates that bias the amplification of library members through selective interactions with the extracellular matrix. Panel (A) reproduced from ref. [125] with permission. Panel (B) reproduced from ref [40] with permission.

1.5.2.2 AIE aggregates: preorganized amphiphilic domains for accelerated macrocyclization

Building on the photophysical and supramolecular properties of AIEgens discussed above, their aggregated states can be viewed more generally as a distinct class of amphiphilic reaction environments. AIE aggregates form densely packed, hydrophobic nanodomains with restricted internal motion, creating preorganized microenvironments that differ from classical micelles in rigidity, packing density and internal order.[28, 95, 107]

From the perspective of dynamic covalent chemistry, such aggregates provide confinement and reduced conformational freedom that can bias reversible bond

exchange by stabilizing specific molecular topologies.[70, 130] Unlike small-molecule templates, AIE aggregates act as soft, collective templates whose influence emerges from mesoscale organization rather than discrete binding sites. Their structural sensitivity to concentration, solvent composition and external stimuli further renders them tunable environments for directing dynamic covalent processes.[99, 105, 106] In this sense, AIE aggregates occupy an intermediate position within the spectrum of amphiphilic templates, bridging highly dynamic micellar systems and the complex, heterogeneous environments encountered in biological settings.

1.5.2.3 Intracellular microenvironments: redox-guided adaptive network formation

Cells constitute the most complex amphiphilic environments encountered by dynamic covalent systems. Biological membranes, organelles, lipid droplets and cytoskeletal structures generate a hierarchy of compartments and interfaces characterized by gradients in polarity, viscosity, molecular crowding and redox potential.[27, 39] These heterogeneous microenvironments influence the partitioning, localization and effective concentration of small molecules, while simultaneously regulating access to oxidants, reductants and nucleophiles, thereby shaping the operation of reversible covalent chemistry in vivo (**Figure 8B**).[40, 81]

From the perspective of dynamic covalent chemistry, intracellular organization imposes spatial and kinetic constraints that bias covalent exchange through redox control, restricted diffusion and interfacial confinement.[27, 131] Local redox gradients, buffering by glutathione and compartment-specific chemical accessibility determine the balance between reduced and oxidized species, while membrane and organellar interfaces limit conformational freedom and molecular mobility.[76, 132] Recent studies on dynamic covalent reactions in living cells and on enzyme-instructed intracellular assemblies demonstrate that endogenous biochemical cues can trigger covalent exchange and supramolecular organization in a spatially regulated manner.[131, 133]

More broadly, protobiological and synthetic systems chemistry models highlight how amphiphilic organization in cellular or protocellular contexts can couple compartmentalization, chemical reactivity and adaptive behavior.[75, 134] In this sense, intracellular microenvironments represent a limiting case of amphiphilic templation, where dynamic covalent networks operate under maximal environmental heterogeneity and regulatory complexity.

1.5.3 Outstanding challenges addressed in this work

Despite substantial progress in dynamic covalent chemistry, the mechanistic basis by which soft amphiphilic templates impose selective pressure on dynamic libraries

remains incompletely understood. In particular, the relative contributions of hydrophobic partitioning, spatial confinement, restricted molecular motion, aggregate curvature and interfacial electrostatics to macrocycle topology and amplification patterns have not been disentangled in a systematic manner across dynamic covalent systems.[3, 8] A unified framework that connects these environmental parameters to selection outcomes in dynamic libraries is still lacking.

A second challenge arises from the integration of aggregation-induced emission (AIE)–based preorganization into dynamic covalent systems. Aggregate-level features such as size, packing density and internal dynamics can simultaneously govern photophysical behavior and reaction kinetics, yet their roles in entropy-driven selection, kinetic trapping and pathway biasing remain poorly defined.[28, 100, 135] Understanding how mesoscale organization couples emission response to reversible covalent exchange is essential for the rational design of AIE-templated dynamic networks.

Finally, extending dynamic covalent chemistry into living cells introduces additional complexity associated with molecular crowding, environmental heterogeneity and competing biochemical processes. How reversible covalent networks operate under redox regulation, spatial confinement and compartmentalized amphiphilic interfaces remains an open question.[13, 40] More broadly, there is a need to bridge mechanistic insights gained from well-defined micellar and aggregate-based systems with the more complex behaviors observed in lipid replicators, protocell models and compartmentalized molecular networks.[67]

1.6 Aims of This Thesis

The central aim of this thesis is to understand how amphiphilic and structurally organized environments regulate the behavior of dynamic disulfide networks in aqueous media. Such environments impose spatial and kinetic constraints that influence macrocycle topology, direct supramolecular assembly, modulate reaction pathways, and enable the emergence of adaptive functions. The thesis was deliberately structured as a hypothesis-guided progression from cellular feasibility, to entropy-driven selectivity in preorganized amphiphilic assemblies, and finally to environmental imprinting and persistence in micellar systems, allowing increasingly controlled model environments to reveal how amphiphilic organization shapes molecular exchange, supramolecular assembly, and ultimately function.

The first objective is to examine how intracellular oxidative conditions influence the formation and reconfiguration of dynamic disulfide networks and how these processes can be monitored through fluorescence. Living cells provide intrinsically heterogeneous chemical environments characterized by regulated redox gradients, molecular crowding, and compartmentalized amphiphilic interfaces. This objective

investigates how a dithiol precursor undergoes oxidation-induced macrocyclization inside cells, how the resulting disulfide macrocycles associate with aggregation-induced emission (AIE) luminogens to form fluorescent assemblies, and how these structures respond reversibly to intracellular reductive and oxidative stimuli. Through this approach, the objective establishes a mechanistic framework for integrating dynamic covalent chemistry with intracellular redox regulation and adaptive behavior.

The second objective is to elucidate how aggregation-induced emission luminogens create preorganized amphiphilic environments that bias dynamic disulfide libraries toward defined macrocyclic products while providing optical access to structural evolution. In aqueous solution, AIE molecules form confined hydrophobic domains that modulate molecular mobility and local concentration. This objective explores how such AIE-based assemblies accelerate thiol oxidation, redirect dynamic combinatorial libraries toward specific macrocycles, and function simultaneously as structural templates, kinetic modulators, and optical reporters. Building on this preorganization mechanism, the study further examines how the anticancer drug doxorubicin (DOX) can be co-assembled within these structures and how fluorescence modulation can be used to follow its loading and release in real time.

The third objective is to determine how transient micellar microenvironments direct macrocycle topology, promote amplification pathways, and imprint persistent supramolecular features within dynamic disulfide libraries. Surfactant micelles provide dynamic nanoscale compartments that control precursor partitioning, constrain conformations, and reshape the energetic landscape accessible to macrocycle formation. This objective investigates how different micellar regimes select for distinct macrocyclic ring sizes, how feedback-driven amplification and self-replication can emerge under specific conditions, and how selected species assemble into higher-order supramolecular structures. Particular emphasis is placed on determining whether such functions persist after removal of the micellar scaffold, thereby probing how transient environments can encode lasting molecular memory and chirality.

Taken together, these objectives define a coherent framework for understanding how amphiphilic organization across multiple contexts, including intracellular compartments, AIE-based assemblies, and surfactant micelles, shapes the evolution, selection, and functional emergence of dynamic disulfide networks. Across these settings, the thesis is designed to clarify how amphiphilic environments influence library composition, guide supramolecular assembly, and, in selected systems, produce effects that persist beyond the immediate templating environment.

2 Materials and Methods

2.1 General Methods

2.1.1 General synthetic methods

All reagents and solvents were obtained from commercial suppliers including Sigma-Aldrich, TCI, abcr, Fisher Scientific, BLD, and VWR. Unless otherwise noted, they were used as received without further purification. Anhydrous solvents were dried and stored under appropriate conditions prior to use. The progress of synthetic reactions was monitored by thin-layer chromatography (TLC) on silica gel 60 F254 plates (Merck) and visualized under UV light or by chemical staining, such as potassium permanganate ($KMnO_4$), where appropriate. After completion, reactions were worked up using standard aqueous and organic extraction procedures where necessary. Detailed synthetic procedures and characterization data for all compounds are provided in the corresponding sections of this thesis or in the original publications where applicable.

Automated flash column chromatography was employed for the purification of compounds when required. Purifications were performed using a Büchi Pure 850 system equipped with pre-packed silica gel cartridges. Typical cartridge sizes ranged from 4 g to 40 g, depending on the scale of purification.

Elutions were carried out using solvent systems such as petroleum ether/ethyl acetate (PE/EA), dichloromethane/methanol (DCM/MeOH), or petroleum ether/dichloromethane (PE/DCM), with gradients adjusted as necessary according to the separation requirements. Compound detection was performed using UV absorbance at 254 nm, and an evaporative light-scattering detector (ELSD) was used for compounds lacking UV chromophores. In addition, conventional silica gel column chromatography under atmospheric pressure was occasionally employed when appropriate.

2.1.2 General DCLs preparation

Stock solutions of building blocks and templates were freshly prepared at higher concentrations prior to the preparation of dynamic combinatorial libraries (DCLs).

Phosphate-buffered saline (PBS) or borate buffer (50 mM, pH 7.4) was used as the aqueous medium unless otherwise stated. Stock solutions were mixed and diluted in appropriate ratios to achieve the desired final concentrations in the DCLs, typically in a total volume of 0.5 mL. The resulting mixtures were stirred at 700 rpm at room temperature (22–23 °C) under continuous exposure to air. Unless otherwise stated, compositional comparisons are based on normalized HPLC/UPLC peak-area fractions obtained under identical analytical conditions within a given experimental series, including fixed injection volume, fixed detection wavelength, and consistent chromatographic integration parameters. Operationally, compositional stability was inferred when monomer consumption was complete, or had reached a constant minimum level, and the relative peak-area distribution remained unchanged over consecutive time points within the resolution of the analytical method.

2.1.3 Cell culture

Cells were cultured under standard conditions in a humidified incubator at 37 °C with 5% CO_2. Cells were incubated in complete culture medium and propagated according to standard cell culture protocols prior to use in subsequent experiments.

2.2 Characterization Methods

2.2.1 Nuclear magnetic resonance (NMR)

^{1}H and ^{13}C NMR spectra, as well as COSY, NOESY, DOSY and transverse relaxation (T_2) experiments, were recorded on Bruker AVANCE-III NMR spectrometers at magnetic field strengths corresponding to ^{1}H frequencies of 500, 600 and 850 MHz. NOESY experiments were performed using the *noesygpphpp* pulse sequence. DOSY measurements were carried out using the *ledbpgp2s* pulse program with linear gradient ramping. The gradient strength was adjusted to ensure a signal attenuation of approximately 90–95% across the diffusion dimension. Transverse relaxation time (T_2) was determined using the Carr-Purcell-Meiboom-Gill (CPMG) pulse sequence. All data were processed and analyzed using Topspin and MestReNova software.

2.2.2 Liquid chromatography (HPLC/UPLC)

High-performance liquid chromatography (HPLC) and ultra-performance liquid chromatography (UPLC) were employed to analyze the composition of samples throughout this thesis. Analytical HPLC measurements were performed using an Ultimate 3000 system, while UPLC analyses were carried out on a Waters

ACQUITY H-Class system. Chromatographic separations were conducted under reversed-phase conditions using gradient elution, with detection by UV absorbance at appropriate wavelengths. For compositional comparison within each experimental series, normalized peak-area fractions were extracted from chromatograms acquired under identical analytical conditions, including fixed injection volume, fixed detection wavelength, and unchanged integration settings.

Semi-preparative chromatographic separations were performed when required for compound isolation using an Agilent 1100 system. Detailed chromatographic conditions for specific analyses or separations are described in the corresponding experimental sections.

2.2.3 Mass spectrometry (MS)

Mass spectrometric analyses were performed to determine the molecular weights and compositions of samples throughout this thesis. Ultra-performance liquid chromatography–mass spectrometry (UPLC–MS) measurements were carried out using a Waters ACQUITY H-Class system coupled to a Waters RDa accurate-mass detector. Mass spectra were acquired in appropriate ionization modes depending on the nature of the analytes. UPLC methods were selected, adapted, or optimized as required for different samples. Data acquisition and processing were performed using standard Waters software.

2.2.4 MALDI-TOF mass spectrometry

MALDI-TOF mass spectra were acquired using a Bruker timsTOF flex mass spectrometer operated in positive or negative ion mode, as appropriate. Samples were prepared in acetone and mixed with a super-DHB matrix solution (10 mg/mL in acetone) prior to analysis. Sample-to-matrix mixtures were typically prepared at a volume ratio of 1:5 (v/v), deposited onto the MALDI target, and allowed to dry before measurement. To ensure optimal signal quality, samples were analyzed at multiple dilution levels when necessary.

2.2.5 UV–Vis spectroscopy

UV–visible absorption spectra were recorded using a PerkinElmer Lambda 365 UV–Vis spectrophotometer. Measurements were performed using quartz cuvettes under ambient conditions.

2.2.6 Thiol quantification (Ellman's assay)

Free thiol concentrations were quantified using Ellman's assay based on the reaction of thiols with 5,5'-dithiobis-(2-nitrobenzoic acid) (DTNB). The formation of the 2-nitro-5-thiobenzoate (TNB) anion was monitored by UV–Vis absorption at 412 nm. Thiol concentrations were calculated using the molar extinction coefficient of TNB^{2-} ($\varepsilon = 14150\ M^{-1}\ cm^{-1}$). [136] Blank samples were measured in parallel for background correction.

2.2.7 Fluorescence spectroscopy

Fluorescence spectra were recorded using a Varian Cary Eclipse fluorescence spectrophotometer. Measurements were performed using quartz cuvettes under ambient conditions.

2.2.8 Circular dichroism (CD)

Circular dichroism (CD) spectra were recorded using a Chirascan CD spectrometer. Measurements were performed at room temperature using quartz cuvettes with appropriate path lengths.

2.2.9 Optical density (OD)

Optical density (OD) measurements were performed using an Agilent BioTek Cytation 5 multimode plate reader. Absorbance was continuously monitored at a wavelength of 550 nm.

2.2.10 Dynamic light scattering (DLS) and zeta potential

The hydrodynamic size distribution and zeta potential of nanoparticles were determined using a Zetasizer Nano ZS instrument (Malvern Instruments Ltd., Worcestershire, UK). Each sample was measured in triplicate.

2.2.11 Powder X-ray diffraction (PXRD)

Powder X-ray diffraction (PXRD) measurements were performed to probe the structural organization of selected samples. PXRD patterns were recorded using a MicroMax 007 HF X-ray generator equipped with a HyPix-6000HE photon-counting detector. The experiments were conducted at the Turku Bioscience Centre. To avoid diffraction artifacts arising from residual salts, samples were prepared from

salt-free solutions. Prior to PXRD measurements, the samples were freeze-dried to obtain dry powders suitable for analysis.

2.2.12 Transmission electron microscopy (TEM)

Transmission electron microscopy (TEM) techniques were employed to investigate the nanoscale morphologies of supramolecular assemblies studied in this thesis. Both conventional TEM and cryogenic transmission electron microscopy (cryo-TEM) were used depending on the nature of the system and the specific structural information required.

Conventional TEM measurements were carried out by the author using standard protocols. Formvar film–coated copper grids (100 mesh) were typically glow-discharged prior to sample application. Samples were deposited onto the grids either directly or following negative staining with an aqueous solution of uranyl acetate, depending on the experiment. After sample deposition, the grids were allowed to air-dry at room temperature. TEM images were acquired using a JEOL JEM-1400 Plus microscope operated at an accelerating voltage of 80 kV.

For selected systems, cryogenic transmission electron microscopy (cryo-TEM) measurements were performed at Aalto University. Cryo-TEM grids were prepared by vitrification using standard plunge-freezing methods, and imaging was conducted on a JEOL JEM-3200FSC liquid-helium cryo-TEM microscope operated at accelerating voltages of 200 or 300 kV.

2.2.13 Scanning electron microscopy (SEM)

Scanning electron microscopy (SEM) was employed to examine the surface morphologies of nanoparticle assemblies studied in this thesis. Field-emission SEM (FE-SEM) measurements were performed using a Thermo Scientific Apreo S microscope. To minimize imaging artifacts arising from residual metal salts, samples were typically prepared from salt-free aqueous solutions (pH 7.4). A small aliquot of the dispersion was drop-cast onto freshly cleaved mica substrates and allowed to air-dry at room temperature. Prior to imaging, the samples were sputter-coated with a thin platinum layer (approximately 10 nm) to enhance surface conductivity and image quality.

2.2.14 *In vitro* cytotoxicity (MTT assay)

In vitro cytotoxicity and cell viability were evaluated using the MTT assay. Cells were seeded in 96-well plates and allowed to adhere overnight prior to treatment. After incubation with different formulations or compounds for a defined period,

MTT solution was added and the cells were further incubated to allow for formazan formation. The resulting formazan crystals were dissolved in dimethyl sulfoxide (DMSO), and absorbance was measured at 570 nm using a microplate reader. Cell viability was calculated relative to untreated control cells. All experiments were performed in triplicate.

2.2.15 Flow cytometry

Flow cytometry (FC) was employed to analyze cellular uptake, intracellular fluorescence signals, and apoptotic cell populations. Measurements were performed using a BD Fortessa flow cytometer. Cells subjected to different treatments were collected and prepared according to standard flow cytometric procedures prior to analysis. For apoptosis assays, cells were stained with Annexin V–FITC and propidium iodide (PI) and subsequently analyzed by flow cytometry.

2.2.16 Confocal laser scanning microscopy (CLSM)

Confocal laser scanning microscopy (CLSM) images were acquired using a Zeiss LSM 880 confocal microscope equipped with an Airyscan detector. Imaging was performed using a 20 × objective under standard confocal conditions. For live-cell imaging experiments, cells were imaged in complete culture medium under controlled environmental conditions (37 °C, 5% CO_2). Time-lapse imaging was performed where indicated to monitor dynamic processes over extended periods. Image acquisition and quantitative analysis were carried out using ZEN software (Zeiss) and ImageJ.

3 Results and Discussion

3.1 Oxidation-Driven Dynamic Molecular Networks in Living Cells

Building on the conceptual framework of systems chemistry, this thesis investigates how amphiphilic molecules can act as operative templates in dynamic disulfide libraries. The overarching goal is to understand how the organization provided by amphiphilic assemblies can translate reversible molecular exchange into controllable selection, amplification, and adaptive behavior. This section establishes the first experimental foundation of this concept by constructing an oxidation-driven molecular network that operates inside living cells, linking redox dynamics to fluorescence modulation through reversible disulfide exchange.

3.1.1 Introduction

The development of systems chemistry has established molecular networks as functional entities that can display emergent behaviors, including adaptability, responsiveness, and dynamic regulation. Unlike traditional chemistry, which primarily focuses on the synthesis and characterization of individual molecules, systems chemistry emphasizes the collective properties arising from interactions within molecular ensembles. Central to this field is the use of dynamic combinatorial chemistry (DCC), where reversible covalent bonds enable the continuous reshaping of networks under thermodynamic or environmental control.[10, 137] Among these, disulfide exchange reactions have proven especially powerful due to their inherent redox responsiveness, compatibility with aqueous environments, and ability to interconvert between reduced and oxidized states in biological contexts.[74, 138]

Oxidative processes play a fundamental role in biology, acting not only as signals in cellular differentiation and apoptosis but also as hallmarks of pathological states such as cancer, inflammation, and neurodegenerative diseases. Reactive oxygen species (ROS) serve as key modulators in these pathways, yet their highly transient and localized nature poses significant challenges for monitoring redox dynamics in living cells. Conventional fluorescent probes often provide irreversible or endpoint signals, while pre-synthesized nanomaterials require elaborate preparation and lack

adaptability within the cellular environment. These limitations underscore the need for synthetic systems capable of autonomously assembling and disassembling in response to cellular oxidative stimuli, thereby offering real-time, reversible readouts of intracellular processes.

Aggregation-induced emission luminogens (AIEgens) represent an attractive solution to this challenge, as their fluorescence is activated through restricted intramolecular motion upon aggregation.[28] By integrating AIEgens into dynamic covalent assemblies, it becomes possible to directly link molecular reconfiguration to an optical signal. tetraphenylethene-derived quaternary ammonium salt (**TPEC$_4$A**), a cationic AIEgen, is particularly suitable for such applications due to its strong electrostatic interactions and biocompatibility.[114] However, its fluorescence response in biological environments requires an assembly partner that can provide both structural organization and dynamic responsiveness.

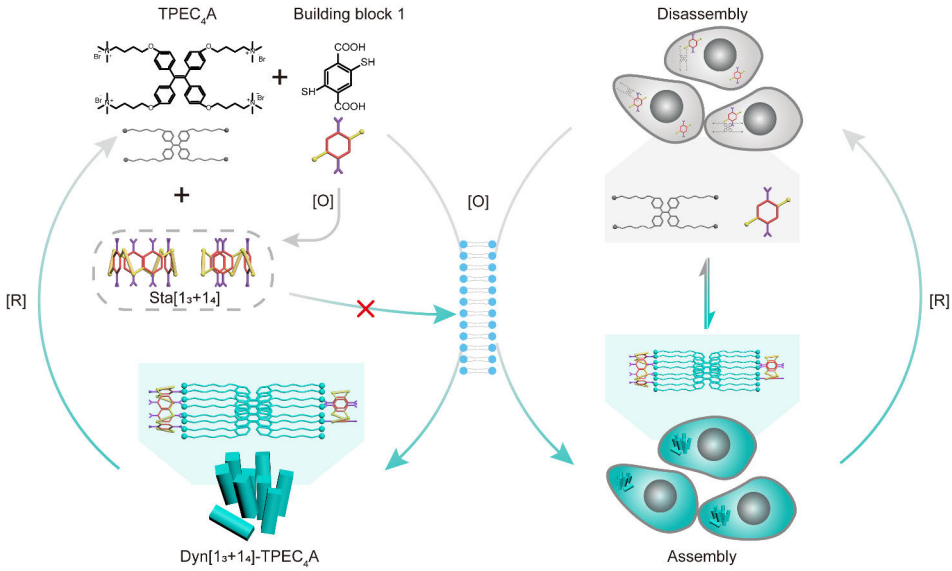

Figure 9. Intracellular oxidation-driven dynamic macrocyclization of dithiol Building block **1** and co-assembly with **TPEC$_4$A** under *in vitro* conditions (left) and within living cells (right), enabling redox-responsive fluorescence. Reproduced from Original Publication I.

To address this challenge, this section introduces an oxidation-driven synthetic molecular network (ODSMN) that operates within living cells. The system is constructed from a dithiol building block **1** that undergoes oxidative macrocyclization to yield dynamic disulfide macrocycles. These macrocycles co-assemble with tetraphenylethylene-derived quaternary ammonium salt (**TPEC$_4$A**) to form fluorescent nanostructures selectively under oxidative conditions. Crucially,

the assemblies are reversible: they can be disassembled by reduction and re-formed upon reoxidation, enabling repeated cycles of fluorescence modulation. By harnessing endogenous ROS as the stimulus, the network autonomously responds to the cellular environment, bridging dynamic systems chemistry with biological complexity (**Figure 9**).

The objective of this section is to demonstrate the construction and operation of ODSMN in vitro and in living cells. Specifically, we investigate (i) the role of oxidation in driving macrocycle formation and fluorescence activation, (ii) the supramolecular interactions that stabilize the assemblies, (iii) the reversibility of the system under redox cycling, and (iv) the ability of the network to function as a fluorescent reporter of intracellular oxidative states. Together, these results establish a framework for adaptive molecular networks that translate redox fluctuations into real-time imaging signals, opening opportunities for applications in bioimaging, diagnostics, and redox-regulated therapeutics.

3.1.2 Experimental section

3.1.2.1 Materials and general methods

All reagents and solvents were obtained from commercial suppliers and used without further purification unless otherwise specified. Phosphate-buffered saline (50 mM PBS, pH 7.4) was used as the standard aqueous medium. Ultrapure water (Milli-Q, 18.2 MΩ·cm) was used in all experiments.

3.1.2.2 Synthesis of building block **1** and templates

The synthesis of building block **1** and the molecular templates **TPEC$_4$A**, as well as its structural analogue phenol-derived quaternary ammonium salt **(PQAS)** as an alternative template, was performed according to previously reported procedures (**Figure 10**).[55, 114] In brief, 2,5-dihydroxyterephthalic acid diethyl ester was converted into 2,5-dimercaptoterephthalic acid through thiocarbamoylation, thermal rearrangement, and subsequent hydrolysis, affording building block **1** as a yellow solid in 95% yield. The para-substituted terephthalate scaffold was chosen for this first intracellular study because, under the experimental conditions used, it oxidized faster and therefore formed disulfides more rapidly.

TPEC$_4$A was synthesized via reduction of 4,4'-dimethoxybenzophenone to tetraphenylethene, followed by demethylation and alkylation. Final quaternization with trimethylamine proceeded efficiently to afford the amphiphilic cationic template. **PQAS** was prepared through alkylation of phenol followed by

quaternization with trimethylamine. Detailed synthetic routes are shown in **Figure 10**.

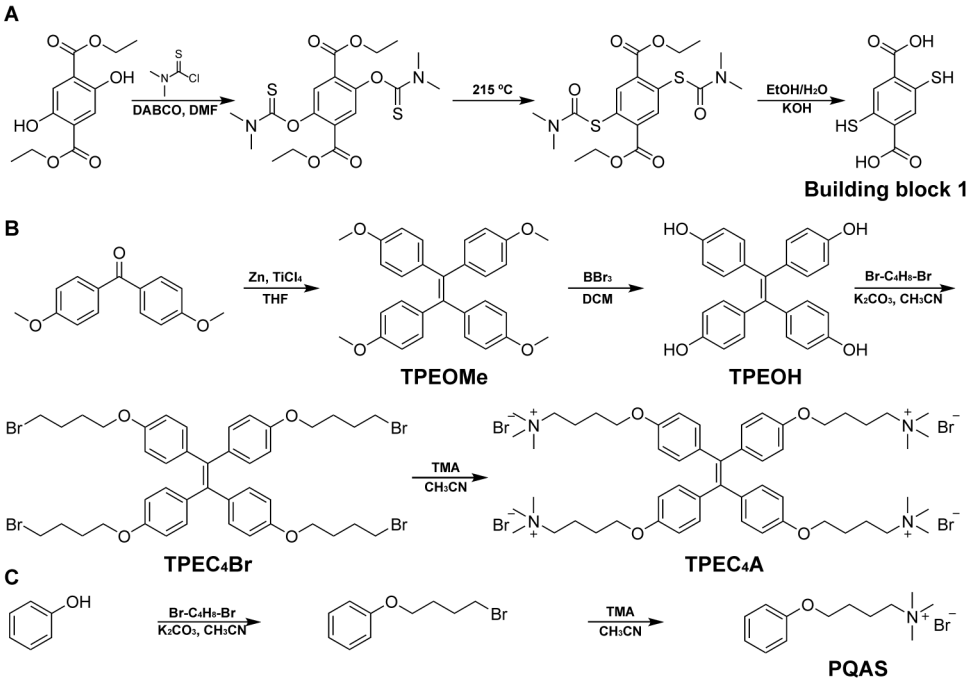

Figure 10. Scheme of the synthetic route of building block **1**, template **TPEC$_4$A** and **PQAS**. Adapted from Original Publication I.

Following synthesis, the chemical structures of building block **1** and the molecular templates (**TPEC$_4$A** and **PQAS**) were confirmed by ^{1}H NMR spectroscopy, as shown in **Figure 11**.

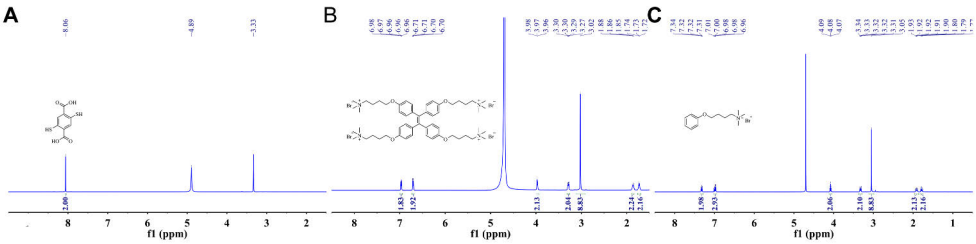

Figure 11. ^{1}H NMR characterization of the molecular components used in this section: (A) building block **1** (600 MHz, MeOD-*d*$_4$), (B) **TPEC$_4$A** (600 MHz, DMSO-*d*$_6$), and (C) **PQAS** (600 MHz, D_2O). Adapted from Original Publication I.

3.1.2.3 Preparation of oxidation-driven assemblies

Stock solutions of building block **1** and **TPEC$_4$A** were mixed in PBS to achieve final concentrations of 1.0 mM and 0.5 mM, respectively. The mixtures were allowed to oxidize under ambient conditions with continuous stirring for up to 72 h. Oxidation and assembly processes were monitored over time by fluorescence spectroscopy. Control experiments were performed with **TPEC$_4$A** or building block **1** alone, as well as pre-oxidized macrocyclic products. The progression of oxidation and the formation of supramolecular assemblies were monitored using spectroscopic and chromatographic techniques.

3.1.2.4 Redox-responsive behavior

Reductive disassembly experiments were performed by adding dithiothreitol (DTT) to oxidized samples at concentrations of 10-40 μM. Reoxidation was achieved by adding hydrogen peroxide (H_2O_2, 50 μM). Fluorescence intensity was monitored as a function of time to evaluate the reversibility of the oxidation-driven assembly process.

3.1.2.5 Cell culture and cytotoxicity evaluation

MCF-7S human breast cancer cells and human dermal fibroblasts (HDF) were cultured under standard conditions (37 °C in a 5% CO_2). Cell viability was evaluated using the MTT assay following 24 h incubation with varying concentrations of building block **1**, **TPEC$_4$A**, or pre-oxidized macrocycles (**Sta[1$_3$+1$_4$]**). In addition, the cytotoxic effects of H_2O_2 and DTT were evaluated and included as oxidative and reductive redox controls, respectively. Cell viability was calculated relative to untreated control cells.

3.1.2.6 Intracellular assembly and imaging

For intracellular experiments, cells were first incubated with **TPEC$_4$A** (0.2 mM) for 30 min, washed with PBS, and subsequently treated with building block **1** (0.4 mM). Oxidation-driven intracellular assembly was investigated by confocal laser scanning microscopy (CLSM) after 12 h incubation. Flow cytometry was employed to quantify fluorescence changes during redox cycling, where cells were sequentially treated with DTT and H_2O_2. Reactive oxygen species stimulation was achieved using phorbol 12-myristate 13-acetate (PMA) at concentrations of 10–50 μM.

3.1.3 Results and discussion

3.1.3.1 Fluorescence properties and oxidation-induced macrocycle formation

To explore how oxidation influences molecular self-organization and fluorescence behavior, the aggregation properties of the AIE-active molecule **TPEC$_4$A** were first examined in phosphate-buffered saline (PBS 50 mM, pH 7.4). Fluorescence measurements revealed that **TPEC$_4$A** remains essentially non-emissive below its critical aggregation concentration (CAC), determined to be approximately 1.26×10^{-4} M (**Figure 12**). At higher concentrations, weak emission appeared as restricted intramolecular motion began to occur, consistent with the typical aggregation-induced emission mechanism.

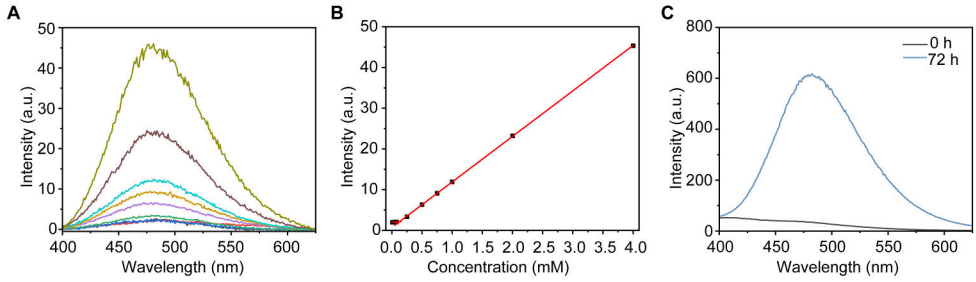

Figure 12. Fluorescence characterization of **TPEC$_4$A** aggregation and oxidation-driven co-assembly: (A, B) CAC determination of **TPEC$_4$A** in PBS (pH 7.4). (C) fluorescence enhancement of **TPEC$_4$A** in the presence of building block **1** upon oxidation. Adapted from Original Publication I.

To establish the oxidation-driven system, **TPEC$_4$A** (0.5 mM) was mixed with the building block **1** (1.0 mM) in PBS and allowed to oxidize under ambient conditions for 72 hours. A pronounced enhancement of fluorescence intensity was observed during this process (**Figure 12 C**), indicating that oxidation promoted the formation of supramolecular aggregates capable of restricting the intramolecular rotation of the phenyl rings in **TPEC$_4$A**. The increase in fluorescence intensity correlated well with the progress of oxidation, suggesting that molecular organization and redox transformation occur simultaneously.

3.1.3.2 Structural characterization of oxidation products and supramolecular assemblies

To gain insight into the structural nature of the oxidation products and their supramolecular organization, a combination of spectroscopic and microscopic methods was employed. Matrix-assisted laser desorption/ionization time-of-flight (MALDI-TOF) mass spectrometry confirmed that oxidation of building block **1** produced mainly trimeric and tetrameric disulfide macrocycles. The nearly identical trimer-to-tetramer ratios observed in the presence and absence of **TPEC$_4$A** verified that the aggregation-induced emitter does not significantly influence the outcome of the oxidation reaction (**Figure 13A** and **13B**). This finding suggests that oxidation proceeds through a self-limiting disulfide exchange process, leading to a stable macrocyclic equilibrium.

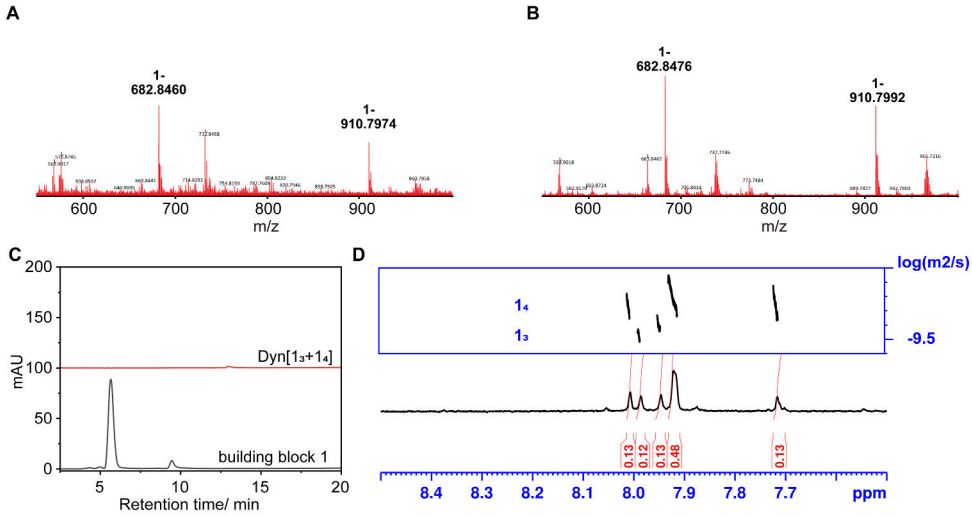

Figure 13. Structural characterization of oxidized dynamic combinatorial libraries. (A) MALDI-TOF mass spectrum of oxidized **Dyn[1$_3$+1$_4$]**, showing peaks at m/z 682.85 and 910.80, assigned to [**1$_3$**-H]$^-$ and [**1$_4$**-H]$^-$, respectively. (B) MALDI-TOF mass spectrum of **Dyn[1$_3$+1$_4$]** in the presence of **TPEC$_4$A** shows the same dominant signals at m/z 682.85 and 910.80, indicating that **TPEC$_4$A** does not alter the composition of the dynamic library (calcd for [**1$_3$**-H]$^-$: 682.86; [**1$_4$**-H]$^-$: 910.81). (C) HPLC traces of building block **1** before oxidation and the oxidized mixture (**Dyn[1$_3$+1$_4$]**). (D) DOSY NMR spectrum of the oxidized library, showing diffusion signals corresponding to trimeric and tetrameric species. Adapted from Original Publication I.

No well-resolved peaks corresponding to oxidized macrocyclic products were detected by HPLC under the current conditions (**Figure 13C**), which is likely attributable to aggregation into nanoscopic assemblies and the conformational diversity of the resulting macrocycles. Diffusion-ordered NMR spectroscopy

(DOSY) provided further information about the molecular size distribution in solution. Two distinct diffusion coefficients were detected, corresponding to trimeric (2.45×10^{-10} m^2/s) and tetrameric (1.82×10^{-10} m^2/s) species (**Figure 13D**). The predominance of the slower-diffusing component indicated that the tetramer represents the major oxidation product. The DOSY data also revealed a substantial decrease in the overall diffusion rates compared with those of the building block **1** (7.35×10^{-10} m^2/s), consistent with the formation of compact cyclic structures that subsequently aggregate into larger assemblies.

Dynamic light scattering analyses were then used to assess the hydrodynamic dimensions of these assemblies in aqueous media. The oxidized mixtures containing both **TPEC$_4$A** and building block **1** yielded nanoparticles with an average size of approximately 500-600 nm, whereas systems prepared with excess building block **1** displayed a secondary population around 80 nm, indicative of partial disassembly under nonstoichiometric conditions (**Figure 14A**). The corresponding zeta potential measurements showed strongly negative surface potentials (**Figure 14B**), confirming electrostatic interactions between the cationic **TPEC$_4$A** and anionic disulfide macrocycles as the main driving force for network stabilization.

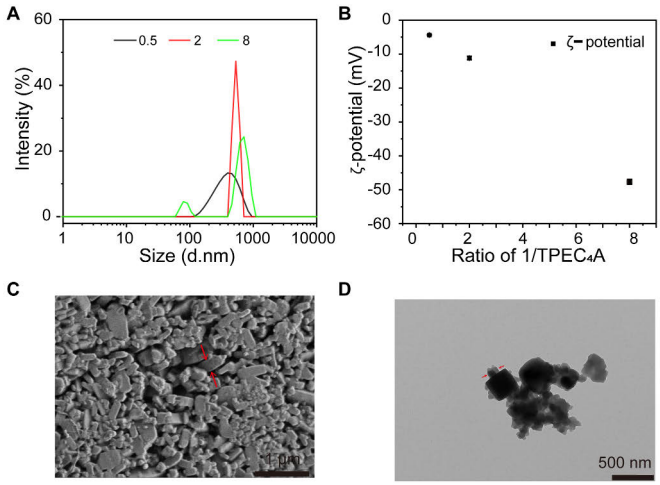

Figure 14. (A) DLS profiles of **Dyn[1$_3$+1$_4$]-TPEC$_4$A** at different building block **1** concentrations. (B) Zeta potential values of the corresponding assemblies. (C) TEM image of **Dyn[1$_3$+1$_4$]-TPEC$_4$A** aggregates (scale bar: 1 μm). (D) SEM image of **Dyn[1$_3$+1$_4$]-TPEC$_4$A** aggregates (scale bar: 500 nm). Adapted from Original Publication I.

Morphological observations by scanning electron microscopy revealed uniform tetragonal prism-like architectures, and transmission electron microscopy demonstrated that the cross sections of these structures were square with widths around 150 nm (**Figure 14C** and **14D**). The absence of any diffraction peaks in

powder X-ray diffraction patterns indicated that the supramolecular assemblies lack long-range crystalline order and are best described as amorphous networks held together by multiple noncovalent interactions.

Taken together, these complementary characterizations demonstrate that oxidation of the building block **1** leads to the formation of discrete macrocycles that further assemble into well-defined nanoscale architectures. The incorporation of **TPEC$_4$A** within these aggregates restricts its intramolecular motions, resulting in efficient fluorescence activation. These findings provide a structural foundation for understanding how redox-triggered molecular transformations can translate into emergent optical properties at the supramolecular level.

3.1.3.3 Mechanistic insights into the oxidation-induced assembly process

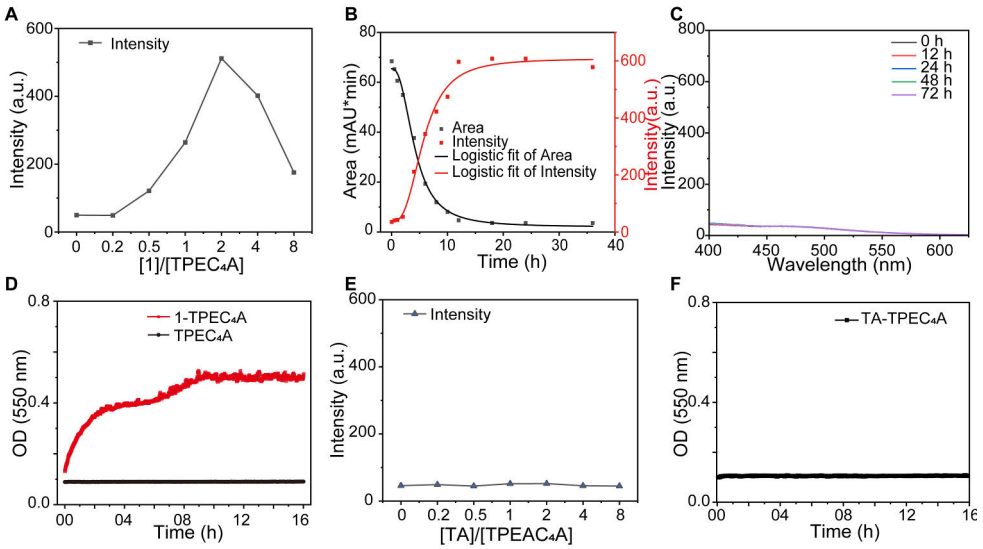

Figure 15. (A) Fluorescence intensity at 480 nm of **TPEC$_4$A** at different [**1**]/[**TPEC$_4$A**] molar ratios after oxidation. (B) Time-dependent consumption of building block **1** (HPLC peak area) and corresponding fluorescence intensity of **TPEC$_4$A**. (C) Time-dependent fluorescence of **TPEC$_4$A** alone. (D) Optical density (OD_{550}) changes of the **1-TPEC$_4$A** mixture and **TPEC$_4$A** alone over time in 50 mM PBS (pH 7.4). (E) Fluorescence intensity of **TPEC$_4$A** upon addition of increasing equivalents of TA. (F) Time-dependent turbidity (OD_{550}) of the TA-**TPEC$_4$A** mixture. Adapted from Original Publication I.

To elucidate the molecular mechanism underlying oxidation-driven assembly and fluorescence activation, the dependence of fluorescence output on the stoichiometric ratio between building block **1** and **TPEC$_4$A** was first examined (**Figure 15A**). Upon oxidation, the fluorescence intensity varied markedly with composition, reaching a

maximum at a molar ratio of **1**:**TPEC$_4$A** = 2:1. This ratio corresponds closely to the charge-balanced regime identified in the DLS measurements, where the formation of well-defined supramolecular aggregates was most pronounced. These observations indicate that efficient fluorescence activation requires an optimal balance between the oxidized anionic macrocycles and the cationic **TPEC$_4$A**, consistent with the aggregation behavior discussed above.

Having established the optimal stoichiometry, the temporal evolution of oxidation-driven assembly was subsequently investigated. A mixture containing building block **1** (1.0 mM) and **TPEC$_4$A** (0.5 mM) was incubated in PBS buffer under ambient conditions, and fluorescence changes were recorded over time (**Figure 15B**). Initially, the solution was nearly non-fluorescent, but as oxidation progressed, a sharp tenfold increase in intensity was observed, reaching a plateau after approximately 12 hours. The consumption of building block **1** during this period matched the fluorescence growth profile, indicating that oxidation triggers self-assembly and fluorescence activation.

In contrast, **TPEC$_4$A** alone exhibited no appreciable change in fluorescence intensity over time under identical conditions (**Figure 15C**). Concurrently, optical density (OD_{550}) increased, signifying the formation of supramolecular aggregates that stabilized upon completion of oxidation (**Figure 15D**). These observations indicate a close temporal correlation between molecular oxidation and supramolecular aggregation. To further verify the necessity of thiol-driven oxidative assembly, terephthalic acid (TA), a dicarboxylic molecule lacking thiol groups, was employed as a control. In contrast to building block **1**, the TA-based system failed to induce either fluorescence enhancement or changes in optical density upon oxidation (**Figure 15E** and **15F**), indicating that thiol functionalities are essential for initiating oxidation-driven aggregation. Together, these results suggest that gradual oxidation is critical for directing the formation of stable and functional supramolecular assemblies.

Table 1. T_2 relaxation times of the DCLs measured by the CPMG NMR experiments on a 600 MHz NMR spectrometer at 298 K.

T_2 (ms)	1H	HA	HB	HC	HD	HE	HF	HG
1	58.80							
TPEC$_4$A		745.92	706.79	43.90	353.90	354.44	434.29	593.93
1-TPEC$_4$A	42.73	183.07	147.48	14.73	107.93	138.08	155.05	254.67

Note: The labels a-g indicate the positions of protons on the **TPEC$_4$A** molecule and are used solely for identifying the T_2 relaxation times shown in **Table 1**. The concentration of precursor building block **1** is 1.0 mM and the concentration of **TPEC$_4$A** is 0.5 mM in 50 mM phosphate buffer (pD 7.4, D_2O). Reproduced from Original Publication I.

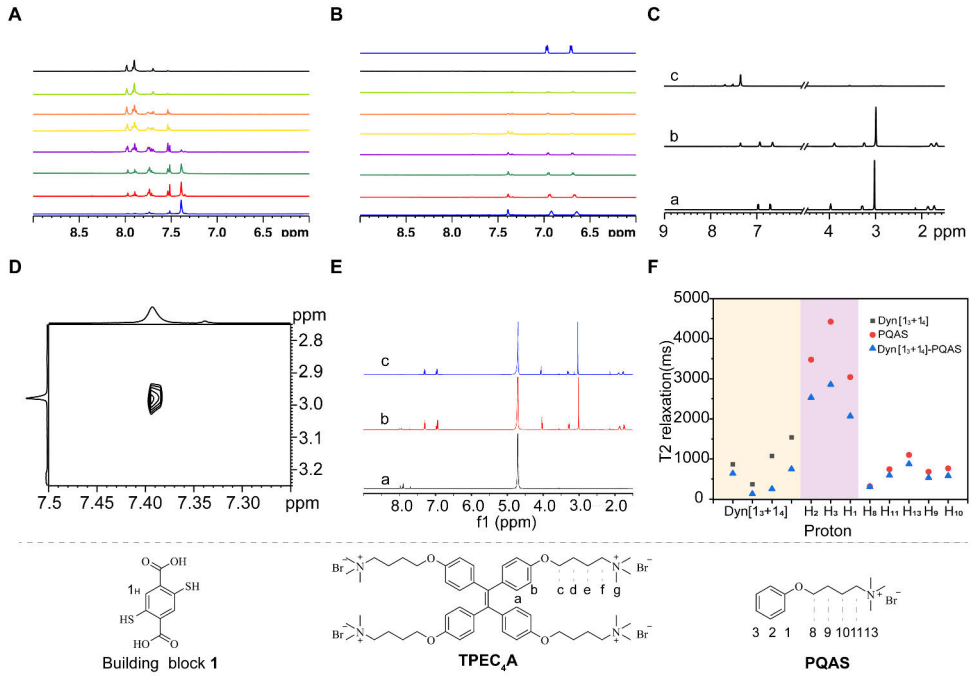

Figure 16. Time-dependent ^{1}H NMR spectra of building block **1** during oxidation (0-14 h) in the absence (A) and presence (B) of **TPEC$_4$A**. Partial ^{1}H NMR spectra of **TPEC$_4$A**, building block **1**, and their mixture, showing chemical-shift changes upon mixing. (D) 2D NOESY spectrum of the **1-TPEC$_4$A** mixture, indicating intermolecular proximity between building block **1** and the trimethylammonium groups of **TPEC$_4$A**. (E) ^{1}H NMR spectra of **PQAS**, **Dyn[1$_3$+1$_4$]-PQAS**, and **Dyn[1$_3$+1$_4$]**, showing signal shifts upon complexation. (F) T_2 relaxation times measured by CPMG experiments for selected **PQAS** protons, showing reduced T_2 values upon interaction with **Dyn[1$_3$+1$_4$]**. Adapted from Original Publication I.

To elucidate the interactions between building block **1** and **TPEC$_4$A**, ^{1}H NMR spectroscopy was performed. Upon oxidation, the NMR signals of building block **1** and **TPEC$_4$A** gradually diminished (**Figure 16A** and **16B**), consistent with oxidation-induced aggregation and restricted molecular mobility. Therefore, the interaction analysis was focused on the early stage prior to oxidation, where both components remained NMR-detectable. The addition of **TPEC$_4$A** caused a downfield shift of aromatic signals from building block **1** and an upfield shift of protons from **TPEC$_4$A**, indicating electrostatic attraction and host-guest complexation (**Figure 16C**). Two-dimensional NOESY spectra confirmed spatial proximity between the aromatic protons of building block **1** and the trimethylammonium group (Hg) of **TPEC$_4$A** (**Figure 16D**), while T_2 relaxation studies revealed reduced mobility for both molecules, supporting preorganization in solution (**Table 1**).

To assess the generality of this interaction mode, a phenol-derived quaternary ammonium salt (**PQAS**) was employed as an analogue of **TPEC$_4$A**. Upon complexation with the oxidized form of building block **1**, **PQAS** exhibited uniform upfield shifts in its proton resonances together with pronounced reductions in T_2 relaxation times, particularly in the aromatic region (**Figure 16E** and **16F**). These spectral changes are consistent with electrostatic association and restricted molecular mobility in solution.

Together with the NMR observations obtained for **TPEC$_4$A**, these results suggest that electrostatic and host–guest interactions between quaternary ammonium AIEgens and oxidized precursor-derived macrocycles give rise to a preorganized interaction state. As oxidation proceeds and disulfide-linked macrocycles accumulate, further supramolecular assembly progressively restricts the intramolecular motions of the AIEgens, contributing to the formation of **Dyn[1$_3$+1$_4$]-TPEC$_4$A** assemblies with stabilized fluorescence output.

3.1.3.4 Redox responsiveness and reversible network reconfiguration

The reversible nature of disulfide bonds enabled direct evaluation of the system's redox responsiveness. Upon addition of dithiothreitol (DTT), fluorescence intensity gradually decreased, reflecting network disassembly induced by disulfide bond reduction. Lower DTT concentrations produced partial quenching and redox equilibrium within one hour, whereas higher concentrations led to nearly complete fluorescence loss and structural breakdown as confirmed by scanning electron microscopy, which showed disappearance of the prism-like morphology (**Figure 17**).

Reoxidation using hydrogen peroxide effectively restored fluorescence within two hours, indicating reformation of the disulfide-linked network (**Figure 17C**). Repeated reduction–oxidation cycles demonstrated that fluorescence could be recovered multiple times with minimal degradation, confirming the robustness of the dynamic molecular system (**Figure 17D**). These reversible optical transitions illustrate that the supramolecular assemblies behave as adaptive redox-responsive materials whose organization can be modulated by external chemical stimuli.

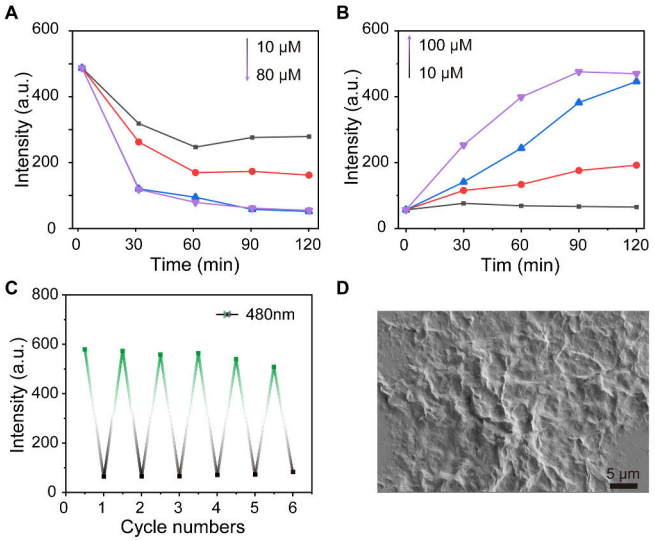

Figure 17. (A) Time-dependent fluorescence quenching of **Dyn[1$_3$+1$_4$]-TPEC$_4$A** upon addition of DTT. (B) Fluorescence recovery upon reoxidation with H_2O_2 following DTT treatment. (C) Fluorescence intensity over multiple DTT/ H_2O_2 redox cycles. (D) SEM image of **Dyn[1$_3$+1$_4$]-TPEC$_4$A** assemblies after DTT reduction, showing disruption of the nanostructures. Reproduced from Original Publication I.

3.1.3.5 Intracellular oxidation-induced assembly and redox imaging

To examine biological applicability, the cytotoxicity of building block **1**, **TPEC$_4$A**, and **Sta[1$_3$+1$_4$]** was evaluated using MCF-7S breast cancer cells. All components exhibited low toxicity with half-maximal inhibitory concentrations above 1 mM, demonstrating acceptable biocompatibility for cell studies (**Figure 18A and 18B**). Because preassembled particles were too large for efficient uptake, a stepwise intracellular assembly strategy was employed. Cells were first incubated with **TPEC$_4$A** followed by addition of building block **1**, allowing oxidation-driven aggregation to occur under physiological oxidative conditions.

Based on the cytotoxicity evaluations, a **TPEC$_4$A** concentration of 0.2 mM was selected for subsequent experiments. At this reduced concentration, pronounced fluorescence enhancement was observed both in PBS buffer and in complete cell-culture medium, confirming effective supramolecular aggregation of the oxidation-driven network under physiologically relevant conditions, with the resulting nanoparticles exhibiting sizes suitable for intracellular applications (**Figure 18D**). Confocal laser scanning microscopy revealed gradual intracellular fluorescence enhancement after 12 hours of incubation, indicating successful oxidation-induced assembly within cells (**Figure 18E**). In contrast, direct incubation of cells with pre-formed **Sta[1$_3$+1$_4$]** resulted in no detectable intracellular fluorescence, which is

attributed to the highly charged nature of the macrocyclic assemblies that limits membrane permeation. Flow cytometry further demonstrated redox responsiveness inside living cells. Treatment with DTT reduced intracellular fluorescence, while subsequent addition of hydrogen peroxide restored it, showing that the system remains dynamically reversible under biological conditions (**Figure 18F**). Short-term exposure to either reductant or oxidant caused no observable cytotoxic effects (**Figure 18C**), further supporting the stability and biocompatibility of the oxidation-driven assemblies.

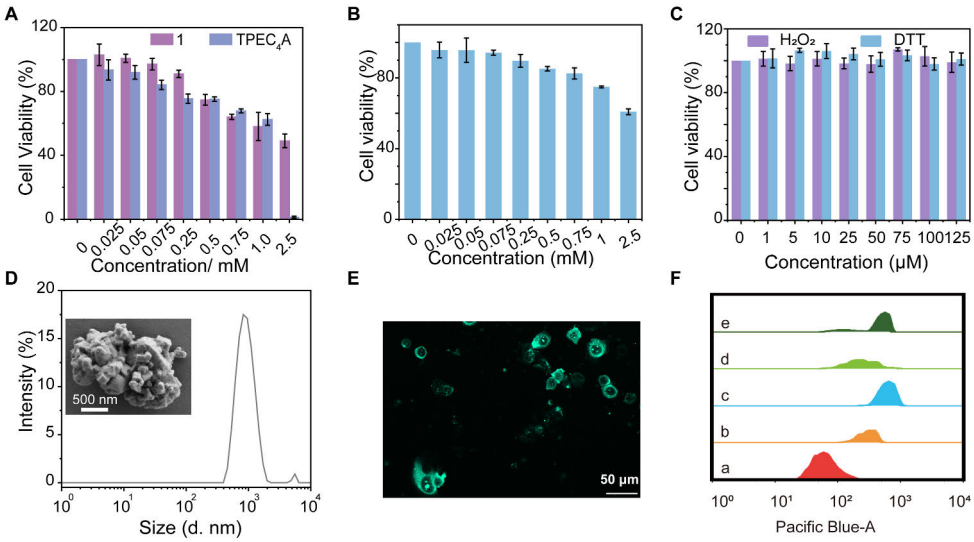

Figure 18. Cellular evaluation and intracellular redox responsiveness of the **Dyn[1_3+1_4]-TPEC$_4$A**. (A-C) Cell viability of MCF-7S cells treated with **1**, **TPEC$_4$A**, **Sta[1_3+1_4]**, and redox reagents (H_2O_2 or DTT), measured by MTT assay. (D) SEM and DLS characterization of preformed **Dyn[1_3+1_4]-TPEC$_4$A** assemblies at low concentration. (E) Confocal fluorescence image of MCF-7S cells after sequential incubation with **TPEC$_4$A** followed by **1**, showing punctate lysosomal fluorescence. (F) Flow-cytometry analysis of intracellular fluorescence under different redox conditions. Adapted from Original Publication I.

Importantly, building block **1** remained readily oxidizable even in the presence of 5.0 mM glutathione (**Figure 19A-C**), demonstrating its compatibility with intracellular redox environments. Together, these results support the feasibility of oxidation-driven assembly and reversible reconfiguration under physiologically relevant conditions.

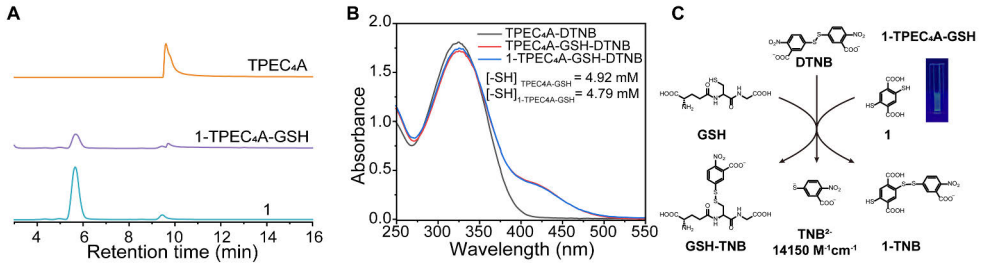

Figure 19. Oxidation of building block **1** in the presence of GSH. (A) HPLC analysis of building block **1** consumption in the **1-TPEC$_4$A**-GSH system after 8 h of oxidation. (B) Thiol quantification by Ellman's assay in the same system. (C) Schematic illustration of the Ellman's assay; inset shows fluorescence of the **1-TPEC$_4$A**-GSH system under UV light (365 nm) after 8 h. Adapted from Original Publication I.

3.1.3.6 Dynamic and adaptive behavior of the synthetic network in living cells

The temporal evolution of intracellular fluorescence was analyzed by time-lapse confocal microscopy to capture the dynamic nature of the synthetic network. A distinct fluorescence growth profile was observed, characterized by a lag period of several hours followed by rapid activation and saturation after approximately 12 hours (**Figure 20A**). To further assess the responsiveness of the **Dyn[1$_3$+1$_4$]-TPEC$_4$A** system to intracellular oxidative stimuli, the effect of phorbol 12-myristate 13-acetate (PMA) was examined. In a cell-free **1-TPEC$_4$A** solution, PMA treatment did not produce any detectable fluorescence enhancement, indicating that PMA does not directly activate the system (**Figure 20C**). In contrast, when applied to living cells, PMA treatment led to a gradual increase in intracellular fluorescence over time (**Figure 20D**), consistent with stimulation of intracellular ROS production. The delayed onset likely reflects endocytic uptake and intracellular oxidation kinetics. Inhibition experiments using ammonium chloride, which increases endolysosomal pH, effectively suppressed fluorescence activation, confirming that the process depends on oxidative conditions in acidic intracellular compartments (**Figure 20E**).

Further redox cycling experiments within living cells showed that addition of DTT induced rapid fluorescence quenching, followed by spontaneous recovery as reoxidation occurred. Subsequent exposure to hydrogen peroxide further enhanced fluorescence intensity, consistent with oxidation-driven regeneration of the supramolecular network (**Figure 20B**). These reversible fluorescence changes provide a real-time optical signature of intracellular dynamic redox processes in living cells.

Comparative experiments using human dermal fibroblasts, which possess lower basal reactive oxygen species levels, resulted in minimal fluorescence activation under identical conditions (**Figure 20F** and **20G**). This contrast

demonstrates that the formation and behavior of the assemblies depend critically on the intracellular redox state. When reactive oxygen species production was stimulated by phorbol 12-myristate 13-acetate, fluorescence intensity increased markedly, confirming that the assemblies respond sensitively to endogenous oxidative stress (**Figure 20H**).

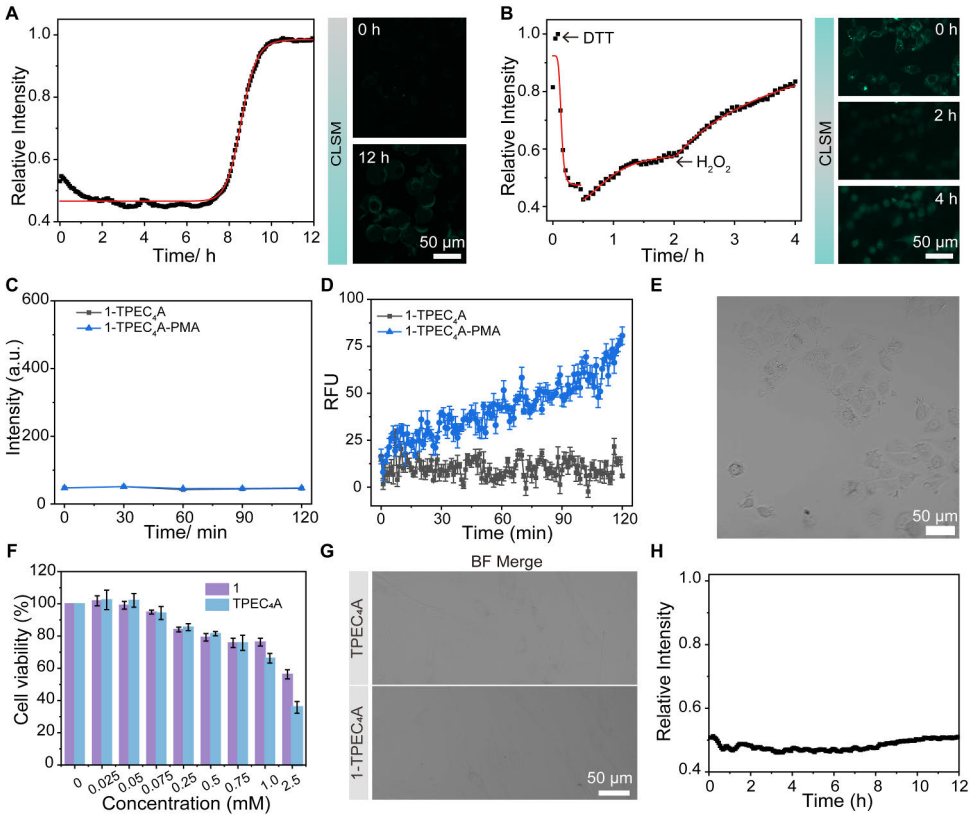

Figure 20. Intracellular redox-responsive fluorescence activation and control experiments. (A) Time-dependent intracellular fluorescence activation of the **1-TPEC$_4$A** system during oxidation, with representative CLSM images of MCF-7S cells at 0 and 12 h. (B) Fluorescence intensity profiles during reduction and reoxidation, showing reversible intracellular fluorescence modulation; representative CLSM images at 0, 2, and 4 h (black dots: experimental data; red lines: fitted curves). Scale bar: 50 μm. (C) Time-dependent fluorescence intensity of **1-TPEC$_4$A** and **1-TPEC$_4$A**-PMA in PBS buffer (pH 7.4). (D) Real-time fluorescence intensity of **1-TPEC$_4$A** and **1-TPEC$_4$A**-PMA in living MCF-7S cells measured by Cytation 5. (E) Confocal fluorescence images of MCF-7S cells treated with **1-TPEC$_4$A** in the presence of NH_4Cl, showing suppressed fluorescence activation. (F) Cell viability of HDF cells treated with **1** or **TPEC$_4$A**, assessed by MTT assay. (G) Confocal fluorescence images of HDF cells after sequential incubation with **TPEC$_4$A**, followed by treatment with building block **1** in the absence of oxidative activation, showing no detectable fluorescence response. (H) Time-dependent intracellular fluorescence activation of the same **1-TPEC$_4$A** shown in (G) during oxidation. Scale bar: 50 μm. Adapted from Original Publication I.

3.1.4 Summary

In summary, an oxidation-driven dynamic molecular network was developed through the co-assembly of thiol-containing building block **1** and the aggregation-induced emitter **TPEC$_4$A**. Oxidative macrocyclization produced discrete trimeric and tetrameric disulfide species that organized into fluorescent supramolecular structures. The assemblies displayed redox-controlled reversibility, maintaining structural integrity over multiple reduction-oxidation cycles. When introduced into living cells, these components underwent in situ oxidation to generate stable, fluorescent aggregates responsive to intracellular redox changes. The system thus exemplifies how chemical oxidation can be harnessed to construct adaptive molecular architectures capable of reversible functional transformation. This work establishes a foundation for the design of oxidation-responsive molecular networks and provides a versatile platform for studying dynamic self-assembly and emergent behavior in complex biological environments.

3.2 Entropy-Controlled Amplification in Amphiphilic Preorganized Libraries

The previous section demonstrated that amphiphile-templated dynamic disulfide networks can operate reversibly within living cells, translating redox fluctuations into fluorescence modulation. While this establishes the biological feasibility of dynamic molecular systems based on amphiphilic organization, the next step is to achieve selective amplification of products under controlled conditions. This section therefore focuses on how amphiphilic templation can overcome entropic barriers in dynamic combinatorial libraries (DCLs), biasing the equilibrium toward specific macrocyclic species and coupling molecular selectivity to functional outputs such as drug release.

3.2.1 Introduction

Dynamic combinatorial chemistry (DCC) provides a versatile platform for generating molecular diversity through reversible covalent reactions.[3, 31] Within such libraries, thermodynamically favored species are amplified under the influence of templates or external stimuli, allowing the system to adapt to its environment. While this principle has enabled the discovery of receptors, catalysts, and self-replicators, achieving both high efficiency and selectivity in the amplification of specific products remains a persistent challenge. In particular, the controlled synthesis of higher-order macrocycles is often hindered by entropic barriers and competing pathways, resulting in mixtures of products rather than a single dominant species.[13]

Overcoming these limitations requires strategies that bias the system toward selective amplification while maintaining its dynamic nature.

Aggregation-induced emission luminogens (AIEgens) offer an intriguing opportunity to address this challenge.[28, 93] Unlike conventional fluorophores that suffer from aggregation-caused quenching, AIEgens become highly emissive upon restriction of intramolecular motion. This unique optical property has been widely exploited in optoelectronics, sensors, and bioimaging. More recently, AIEgens have been recognized not only as fluorophores but also as functional templates capable of influencing supramolecular organization.[107] Their propensity to aggregate and form ordered structures suggests that they could act as preorganizing agents in dynamic systems, lowering the entropic cost of macrocyclization and guiding the selective formation of otherwise inaccessible species.

At the same time, drug delivery remains a central challenge in biomedical research, particularly in the treatment of multidrug-resistant cancers. Doxorubicin (DOX), a widely used chemotherapeutic, is limited by poor intracellular retention and efflux through P-glycoprotein transporters.[139] Nanostructured carriers can improve stability and uptake, yet most delivery systems lack responsiveness and real-time traceability.[140] Integrating drug molecules into a dynamic covalent system, where assembly and disassembly are directly coupled to optical signals, offers a powerful strategy for monitoring drug release in real time while simultaneously enhancing therapeutic efficacy.

This section introduces a system in which an AIEgen template, tetraphenylethylene-derived quaternary ammonium salt (**TPEC$_{10}$A**), drives the selective amplification of an octameric disulfide macrocycle (**2$_8$**) within a DCC framework. The aggregation of **TPEC$_{10}$A** promotes preorganization, accelerating thiol oxidation and directing the system toward quantitative synthesis of **2$_8$**, accompanied by a morphological transformation from micelles to nanofibers. Incorporation of DOX further decreases entropy, accelerates reaction kinetics, and yields a multicomponent nanofiber bundle with high drug-loading efficiency. Importantly, the resulting nanosystem exhibits reversible fluorescence responses to both redox and pH stimuli, enabling visualization of drug release.

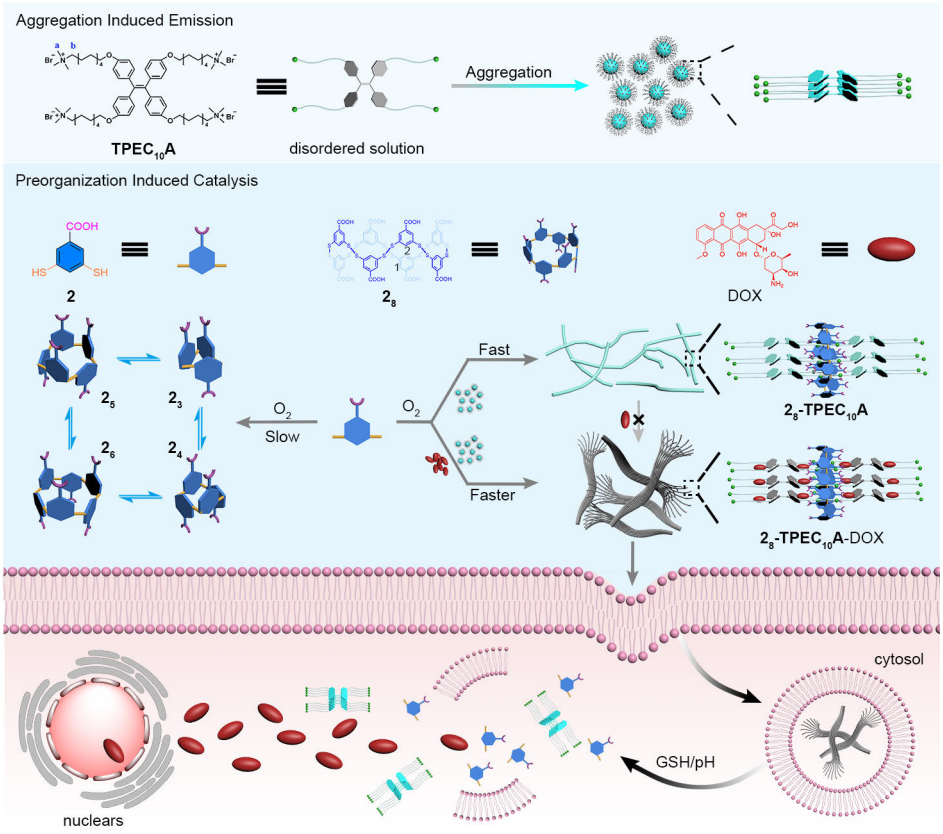

Figure 21. Preorganization-driven amplification in dynamic combinatorial systems. Aggregation of the AIEgen template **TPEC$_{10}$A** induces molecular preorganization in a disulfide-based dynamic combinatorial library, accelerating thiol oxidation and selectively amplifying the octameric macrocycle (**2$_8$**). Incorporation of doxorubicin (DOX) further enhances confinement, leading to adaptive nanostructure formation with redox- and pH-responsive fluorescence and drug release. Adapted from Original Publication II.

The objectives of this section are fourfold: (i) to demonstrate how AIEgen preorganization accelerates dynamic covalent macrocyclization, (ii) to elucidate the mechanism underlying the selective amplification of the octameric macrocycle, (iii) to integrate DOX into the supramolecular assembly to achieve responsive and efficient drug delivery, and (iv) to visualize the spatiotemporal dynamics of drug release in multidrug-resistant cancer cells. Collectively, this study expands the role of AIEgens beyond fluorescence reporters, establishing them as entropic templates that convert molecular preorganization into chemical selectivity and functional performance.

3.2.2 Experimental section

3.2.2.1 Materials and general methods

All reagents and solvents were obtained from commercial suppliers and used without further purification unless otherwise specified. Phosphate-buffered saline (PBS, 50 mM, pH 7.4) was used as the standard aqueous medium. Ultrapure water (Milli-Q, 18.2 MΩ·cm) was used in all experiments. Doxorubicin (DOX, >98%) was purchased from Melone Pharmaceutical Co., Ltd. (Dalian, China).

3.2.2.2 Synthesis of building block **2** and templates

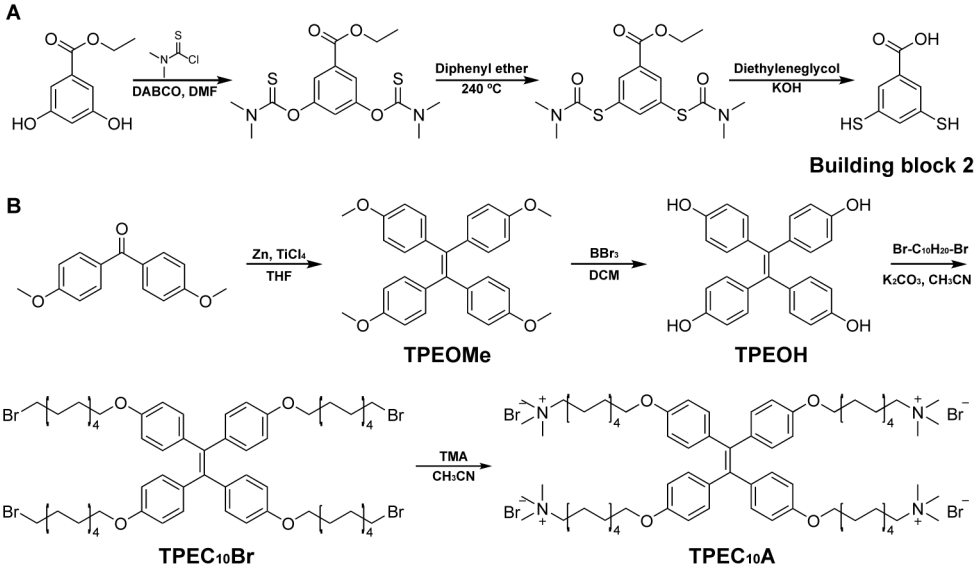

Figure 22. Scheme of the synthetic route of building block **2**, template **TPEC$_{10}$A**. Adapted from Original Publication II.

The synthesis of building block **2** and the molecular template **TPEC$_{10}$A** was carried out according to previously reported procedures with minor modifications (**Figure 22**).[36, 114] In brief, methyl 3,5-dihydroxybenzoate was subjected to thiocarbamoylation using N,N-dimethylthiocarbamoyl chloride in dry N,N-dimethylformamide, followed by thermal Newman–Kwart rearrangement under inert atmosphere. Subsequent hydrolysis and acidification afforded 3,5-dimercaptobenzoic acid (building block **2**). **TPEC$_{10}$A** was synthesized via reduction of 4,4'-dimethoxybenzophenone to tetraphenylethene, followed by demethylation

and alkylation with 1,10-dibromodecane. Final quaternization with trimethylamine proceeded efficiently to afford the amphiphilic cationic template.

Following synthesis, the chemical structures of building block **2** and the molecular templates **TPEC$_{10}$A** were confirmed by ^{1}H NMR spectroscopy and mass spectroscopy, as shown in **Figure 23**.

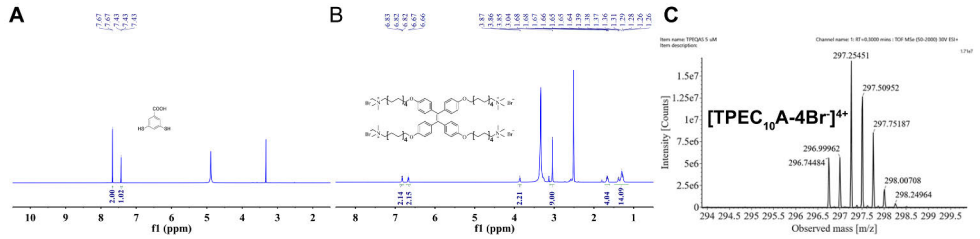

Figure 23. ^{1}H NMR characterization of the molecular components used in this section: (A) building block **2** (600 MHz, DMSO-*d*$_6$), (B) **TPEC$_{10}$A** (600 MHz, DMSO-*d*$_6$), and (C) High-resolution mass spectrometry of **TPEC$_{10}$A**: m/z calcd for $C_{78}H_{132}N_4O_4^{4+}$ [**TPEC$_{10}$A**-4Br]$^{4+}$ 297.25; found 297.2545. Adapted from Original Publication II.

3.2.2.3 Preparation of preorganized dynamic libraries

Dynamic combinatorial libraries (DCLs) were prepared by mixing building block **2** (1.0 mM) and **TPEC$_{10}$A** (0.25 mM) in phosphate-buffered saline (50 mM, pH 7.4). Upon exposure to ambient oxygen, the thiol groups underwent gradual oxidation to form disulfide-linked macrocycles, thereby driving the evolution of the dynamic combinatorial library toward thermodynamically favored assemblies. The mixtures were stirred under ambient conditions until equilibrium was reached. The progression of oxidation and the formation of supramolecular assemblies were monitored using spectroscopic and chromatographic techniques.

3.2.2.4 Drug loading and *in vitro* release studies

Doxorubicin (DOX)-loaded nanofiber assemblies were prepared by introducing DOX into the assemblies formed from building block **2** and **TPEC$_{10}$A**. After complete oxidation and assembly, excess free DOX was removed by dialysis, yielding purified DOX-loaded nanofiber bundles. The drug loading content and loading efficiency were determined by UV–Vis absorption spectroscopy.

The *in vitro* release behavior of DOX from the assemblies was investigated under different pH and redox conditions to simulate physiological and endosomal environments. Release studies were performed at pH 7.4 and pH 5.5 in the absence or presence of glutathione (GSH). At predetermined time points, the amount of released DOX was quantified by UV–Vis spectroscopy.

3.2.2.5 Cellular uptake and cytotoxicity evaluation

The cytotoxicity of free DOX, **2_8-TPEC$_{10}$A**, and DOX-loaded assemblies (**2_8-TPEC$_{10}$A**-DOX) were evaluated using the MTT assay after incubation for a defined period. Cell viability of DOX-resistant NCI/ADR-RES human ovarian cancer cell line was calculated relative to untreated control cells. Cellular uptake of **2_8-TPEC$_{10}$A**-DOX assemblies was quantified by flow cytometry to assess efficiency of internalization.

3.2.2.6 Intracellular distribution and apoptosis analysis

The intracellular distribution of doxorubicin (DOX) and the corresponding supramolecular assemblies were examined by confocal laser scanning microscopy (CLSM) following incubation with **2_8-TPEC$_{10}$A**-DOX. Fluorescence signals originating from DOX and the **TPEC$_{10}$A**-based assemblies were used to visualize intracellular localization and distribution patterns. Where indicated, time-lapse CLSM imaging was performed to monitor dynamic intracellular redistribution over time. Apoptosis induced by different formulations was evaluated using Annexin V–FITC and propidium iodide (PI) staining followed by flow cytometric analysis. The proportions of viable, early apoptotic, late apoptotic, and necrotic cells were quantified to assess the therapeutic efficacy of the **2_8-TPEC$_{10}$A**-DOX.

3.2.3 Results and discussion

3.2.3.1 Formation and characterization of **2_8-TPEC$_{10}$A** nanofibers

The behavior of **TPEC$_{10}$A** in aqueous solution was first investigated. As a cationic amphiphile, **TPEC$_{10}$A** self-assembled into micellar aggregates above its critical aggregation concentration (2.1×10^{-6} M) in PBS buffer at pH 7.4 (**Figure 24A** and **24B**). Transmission electron microscopy revealed spherical micelles with an average diameter of approximately 20 nm (**Figure 24C**). These aggregates displayed the typical aggregation-induced emission (AIE) behavior: fluorescence intensity increased markedly with higher water content as molecular motions became restricted (**Figure 24D** and **24E**). Molecular modeling indicates an extended molecular dimension of approximately 3.3 nm for **TPEC$_{10}$A** (**Figure 24F**).

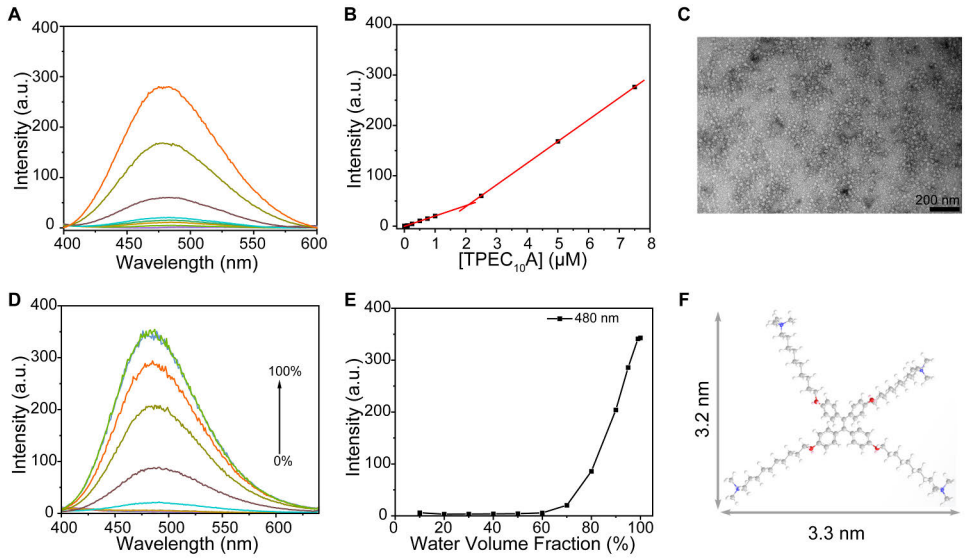

Figure 24. Aggregation behavior and molecular dimensions of **TPEC$_{10}$A**. (A, B) Fluorescence spectra and concentration-dependent intensity of **TPEC$_{10}$A** in PBS buffer. (C) TEM image of **TPEC$_{10}$A** micelles. (D, E) Fluorescence response of **TPEC$_{10}$A** with increasing water volume fraction. (F) Energy-minimized molecular model of **TPEC$_{10}$A**. Adapted from Original Publication II.

When mixed with the dithiol building block **2** (1.0 mM), **TPEC$_{10}$A** (0.25 mM) strongly accelerated the air-oxidation of thiols to disulfide macrocycles. This acceleration was supported by Ellman's thiol assay, which showed a markedly faster depletion of free thiol groups (**Figure 25**). High-performance liquid chromatography and mass spectrometry confirmed the formation of trimeric (**2$_3$**) and tetrameric (**2$_4$**) disulfides as the principal products in the absence of **TPEC$_{10}$A** after 9 days (**Figure 26A** and **26B**). In contrast, in the presence of **TPEC$_{10}$A** the oxidation reached completion within 3 days, as evidenced by Ellman's thiol assay and consistent with HPLC analysis, demonstrating an approximately threefold rate enhancement (**Figure 26C**).

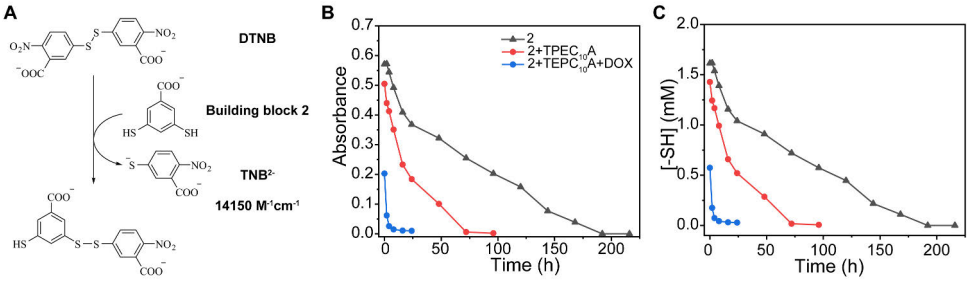

Figure 25. Quantification of changes in building block **2** concentration during oxidation using Ellman's method. (A) Reaction of building block **2** with Ellman's reagent. (B) The UV-Vis absorbance with oxidation time. (C) The thiol concentration with oxidation time. black line: building block **2**, red line: building block **2-TPEC$_{10}$A**, blue line: building block **2-TPEC$_{10}$A** -DOX. Adapted from Original Publication II.

Notably, an additional disulfide macrocycle, the octamer (**2$_8$**), appeared as the dominant species in the **TPEC$_{10}$A**-containing libraries, indicating that the preorganized AIE template not only accelerated the reaction but also imposed remarkable selectivity (**Figure 26D**). Fluorescence spectra showed a pronounced blue shift, characteristic of H-type aggregation, consistent with tighter packing in the nanofiber structure (**Figure 26E**). TEM analysis revealed a morphological transformation from micelles to uniform nanofibers with a width of about 3.7 nm, closely matching the molecular width of **TPEC$_{10}$A**, suggesting linear stacking of the template units (**Figure 26F**).

The zeta potential of pure **TPEC$_{10}$A** micelles was +8.4 mV, whereas that of the **2$_8$-TPEC$_{10}$A** nanofibers shifted to +6.6 mV, confirming partial charge compensation upon complexation between the cationic **TPEC$_{10}$A** and the anionic octameric disulfide. These results collectively demonstrate that **TPEC$_{10}$A**'s amphiphilic preorganization drives selective and near-quantitative formation of **2$_8$**, while the resulting supramolecular organization yields fibrous architectures with distinct optical properties. Importantly, this transition from micellar aggregates to ordered nanofibers reflects a substantial reduction in conformational and translational entropy, effectively lowering the entropic penalty associated with multicomponent macrocyclization, and thereby providing an entropic driving force for the selective amplification of the otherwise unfavorable octameric macrocycle.[13]

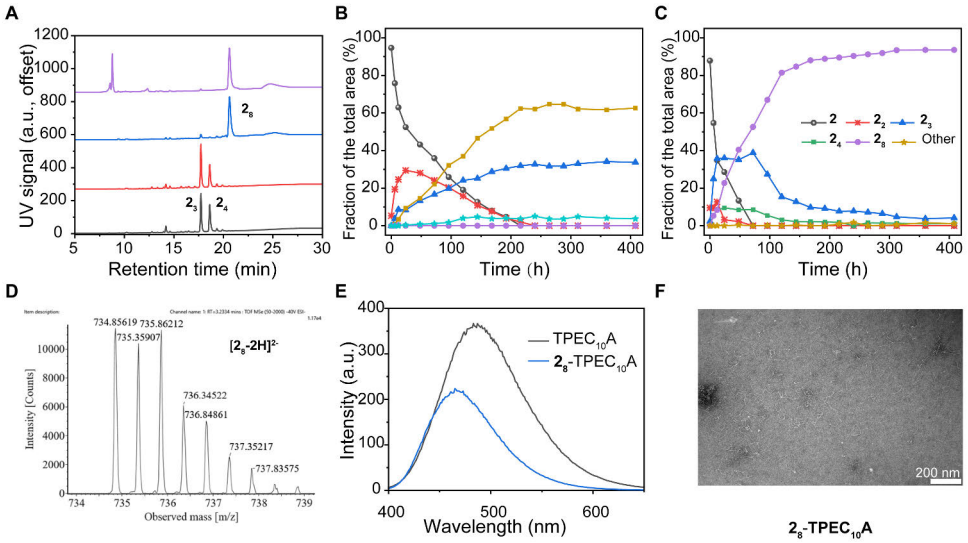

Figure 26. Template-assisted amplification and kinetics of disulfide DCLs. (A) HPLC-MS analysis of fully oxidized DCLs prepared from building block **2** alone, with **TPEC$_{10}$A** at different concentrations. (B, C) Kinetic profiles of DCL formation from building block **2** alone (B) and in the presence of **TPEC$_{10}$A** (C) in PBS buffer (50 mM, pH 7.4). (D) enlarged mass spectrum of Octamer (**2$_8$**) from the MS analysis. m/z calculated for $C_{56}H_{30}O_{16}S_{16}^{2-}$: 734.8538 [**2$_8$**-2H]$^{2-}$, found: 734.8562. (E) Fluorescence spectra of **TPEC$_{10}$A** solution and diluted **2$_8$-TPEC$_{10}$A** library in PBS buffer. (F) TEM image of the **2$_8$-TPEC$_{10}$A** assemblies. Adapted from Original Publication II.

3.2.3.2 Mechanistic analysis of preorganization and accelerated macrocyclization

To elucidate the molecular basis for the selective formation of **2$_8$**, the early-stage evolution of the system was examined using complementary spectroscopic methods. To probe the relationship between supramolecular organization and the oxidation process, the fluorescence kinetics of a diluted dynamic library containing building block **2** and **TPEC$_{10}$A** were first monitored in PBS buffer (50 mM, pH 7.4). Upon mixing, **TPEC$_{10}$A** exhibited an immediate blue shift in fluorescence emission, indicating rapid supramolecular preorganization that precedes and conditions the subsequent oxidation-driven macrocyclization. As thiol oxidation proceeded, the fluorescence intensity gradually decreased and reached a steady state, closely mirroring the depletion of free thiols during the reaction (**Figure 27A** and **27B**). Compared with **TPEC$_{10}$A** alone, the final fluorescence intensity decreased by 41.1%, suggesting that early aggregation-induced organization accompanies and precedes accelerated macrocyclization.

To understand the molecular basis for the selective formation of **2$_8$**, ^{1}H NMR experiments were performed at the early stages of oxidation. In the presence of

TPEC$_{10}$A, the aromatic proton H_2 of building block **2** shifted upfield and exhibited a substantial reduction in T_2 relaxation time from 3049 ms to 608 ms, reflecting restricted molecular mobility and enhanced electrostatic association within the hydrophobic interior of **TPEC$_{10}$A** aggregates (**Figure 27C**). These effects indicate that the building block penetrates the hydrophobic region of the AIE template, resulting in effective preorganization before oxidation.

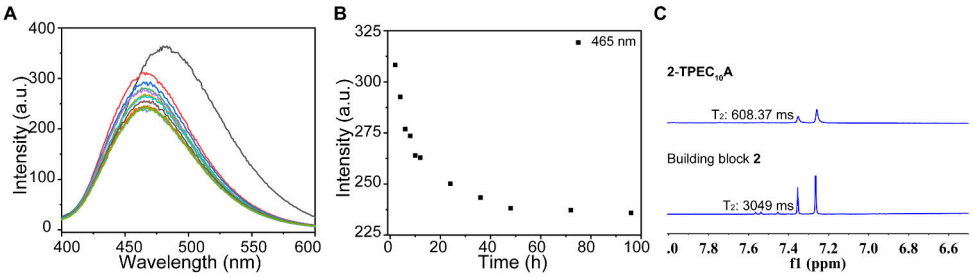

Figure 27. Fluorescence evolution and NMR characterization of **2-TPEC$_{10}$A** dynamic library. (A) Time-dependent fluorescence spectra of a diluted library containing building block **2** (40 μM) and **TPEC$_{10}$A** (10 μM) in PBS buffer (50 mM, pH 7.4) during oxidation. (B) Corresponding fluorescence intensity at 465 nm as a function of oxidation time. (C) Partial ^{1}H NMR spectrum (600 MHz) of the dynamic combinatorial library recorded in D_2O (pD 7.4). Adapted from Original Publication II.

To further probe electrostatic interactions, the cationic surfactant octadecyl trimethylammonium bromide (**OTAB**) was employed as minimal cationic analogue of **TPEC$_{10}$A** to probe electrostatic interactions. ^{1}H NMR and 2D NOESY spectra of **OTAB** with **2$_8$** revealed upfield shifts of ammonium protons and downfield shifts of aromatic protons on **2$_8$**, confirming complementary electrostatic binding between carboxylates and quaternary ammonium groups (**Figure 28**).

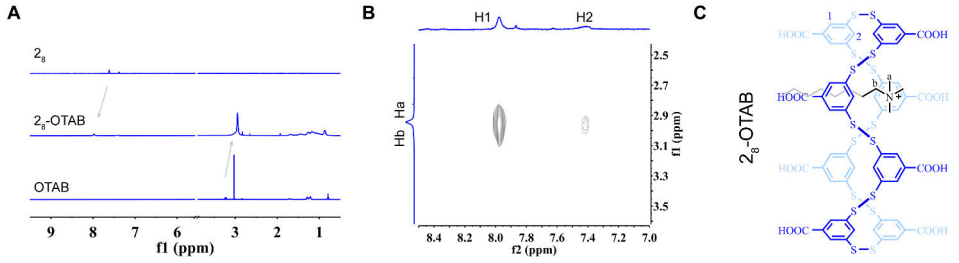

Figure 28. NMR characterization of the interaction between **2$_8$** and **OTAB**. (A) Partial ^{1}H NMR spectra of **OTAB**, **2$_8$-OTAB**, and **2$_8$** in D_2O (pD 7.4). (B) NOESY spectrum of the **2$_8$-OTAB** mixture. (C) Schematic illustration of the **2$_8$-OTAB** complex. Adapted from Original Publication II.

The complex stoichiometry between **2_8** and **$TPEC_{10}A$** was determined to be 1:2 by Job's plot analysis using fluorescence spectroscopy (**Figure 29A** and **29B**). The binding affinity was further quantified by fluorescence titration under different experimental conditions (**Figure 29C-F**). A representative association constant of $K = 6.2 \times 10^5\ M^{-1}$ was obtained in PBS buffer (50 mM, pH 7.4) at room temperature. A slight decrease in binding strength was observed at lower pH, whereas variations in temperature had only a minor effect, indicating that the complexation is stable over a broad temperature range. The reduced affinity under acidic conditions is attributed to partial protonation of the carboxylate groups, which weakens the electrostatic interactions between **2_8** and **$TPEC_{10}A$**.

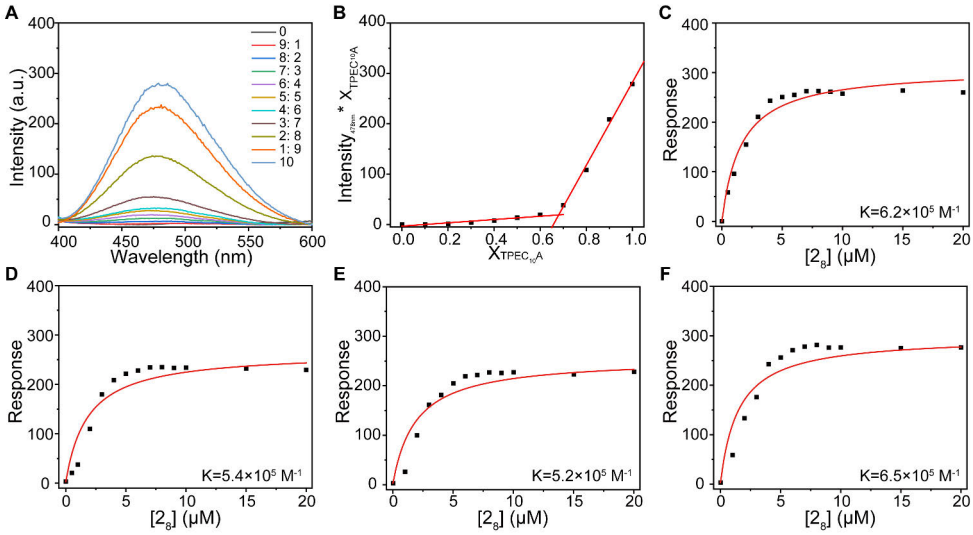

Figure 29. Stoichiometry and binding analysis of the **2_8-$TPEC_{10}A$** complex in PBS buffer. (A) Fluorescence spectra of **2_8-$TPEC_{10}A$** mixtures at different molar ratios with a constant total concentration (10 μM, pH 7.4). (B) Job plot indicating a 1:2 stoichiometry between **2_8** and **$TPEC_{10}A$**. (C–F) Fluorescence titration curves of **2_8** into **$TPEC_{10}A$** under different pH and temperature conditions. Fluorescence titration and Job-plot analyses revealed a 1:2 stoichiometry with a representative association constant of $K = 6.2 \times 10^5\ M^{-1}$ in PBS (pH 7.4). Adapted from Original Publication II.

To verify the structural role of aggregation, dynamic libraries were reconstructed in 70% acetonitrile, where **$TPEC_{10}A$** aggregates were disrupted. Under these conditions, the octamer **2_8** was no longer detected, and trimeric species became predominant (**Figure 30A** and **30B**). The loss of selectivity in organic medium confirmed that aggregation and electrostatic preorganization are prerequisites for the accelerated and selective macrocyclization, by eliminating the entropic advantage conferred by confinement when the aggregated state is disrupted. Collectively, these

results indicate that one molecule of $\mathbf{2_8}$ strongly associates with two quaternary ammonium groups from adjacent $\mathbf{TPEC_{10}A}$ molecules, consistent with the proposed binding model (**Figure 30C**). These observations support an entropy-controlled mechanism, in which aggregation-induced preorganization lowers the entropic penalty associated with macrocyclization, thereby accelerating reaction kinetics and biasing the dynamic equilibrium toward the octameric product.[141]

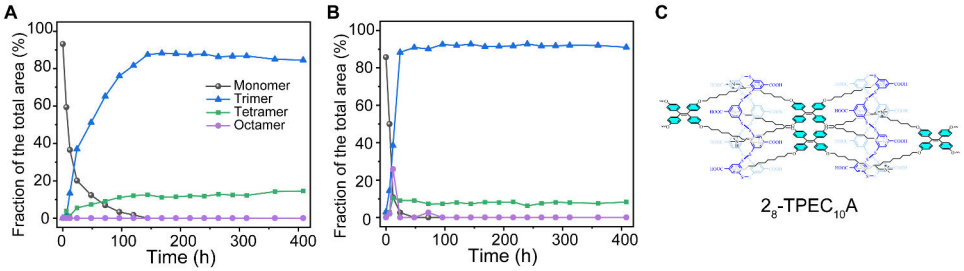

Figure 30. Time-dependent product distribution of DCLs in 70% acetonitrile. (A) Building block **2** (1.0 mM) in 70% (v/v) acetonitrile/PBS buffer. (B) Building block **2** (1.0 mM) with $\mathbf{TPEC_{10}A}$ (0.25 mM) under the same conditions. (C) Schematic illustration of the proposed 1:2 binding between $\mathbf{2_8}$ and $\mathbf{TPEC_{10}A}$. Adapted from Original Publication II.

3.2.3.3 Synthesis and characterization of $\mathbf{2_8}$-$\mathbf{TPEC_{10}A}$-DOX nanofiber bundles

Building on the catalytic role of AIE preorganization, the anticancer drug doxorubicin (DOX) was incorporated into the dynamic libraries to generate a ternary nanosystem. DOX contains both aromatic and cationic regions, allowing it to embed within the hydrophobic domains of supramolecular assemblies and modulate reaction thermodynamics through entropy reduction. When 0.4 mM DOX was introduced to the 1.0 mM building block **2** and 0.25 mM $\mathbf{TPEC_{10}A}$ mixture, oxidation was accelerated by a further factor of 4.8 relative to the $\mathbf{TPEC_{10}A}$-only system (**Figure 31A** and **31B**).

Fluorescence of $\mathbf{TPEC_{10}A}$ was progressively quenched as DOX concentration increased, with nearly complete quenching at 0.5 mM. Spectral overlap between $\mathbf{TPEC_{10}A}$ emission and DOX absorption confirmed an energy-transfer process (**Figure 31C** and **31D**). Importantly, the product distribution remained dominated by the octamer $\mathbf{2_8}$ (**Figure 26A**), confirming that the presence of DOX enhanced the reaction rate without compromising selectivity. The optimized formulation ($\mathbf{2_8}$: $\mathbf{TPEC_{10}A}$: DOX = 0.125:0.25:0.5 mM) exhibited a drug loading content of 31.8% and an encapsulation efficiency of 93.5%. TEM and DLS analyses revealed that the nanosystem transformed into bundled nanofibers with average dimensions of 50 × 220 nm and hydrodynamic diameters around 260 nm. Zeta potential measurements

showed a moderately positive surface charge of +5.2 mV, indicating partial charge compensation and colloidal stability of the nanofiber bundles. PXRD patterns lacked crystalline peaks, indicating amorphous encapsulation of DOX within the nanofiber bundles (**Figure 31E-H**). GSH treatment led to pronounced disassembly of nanofiber bundles, as observed by TEM (**Figure 31I**). The amphiphilic nature of DOX and its electronic interaction with **TPEC$_{10}$A** likely drive its localization in the hydrophobic core, producing stable, fluorescently quenched nanofiber bundles.

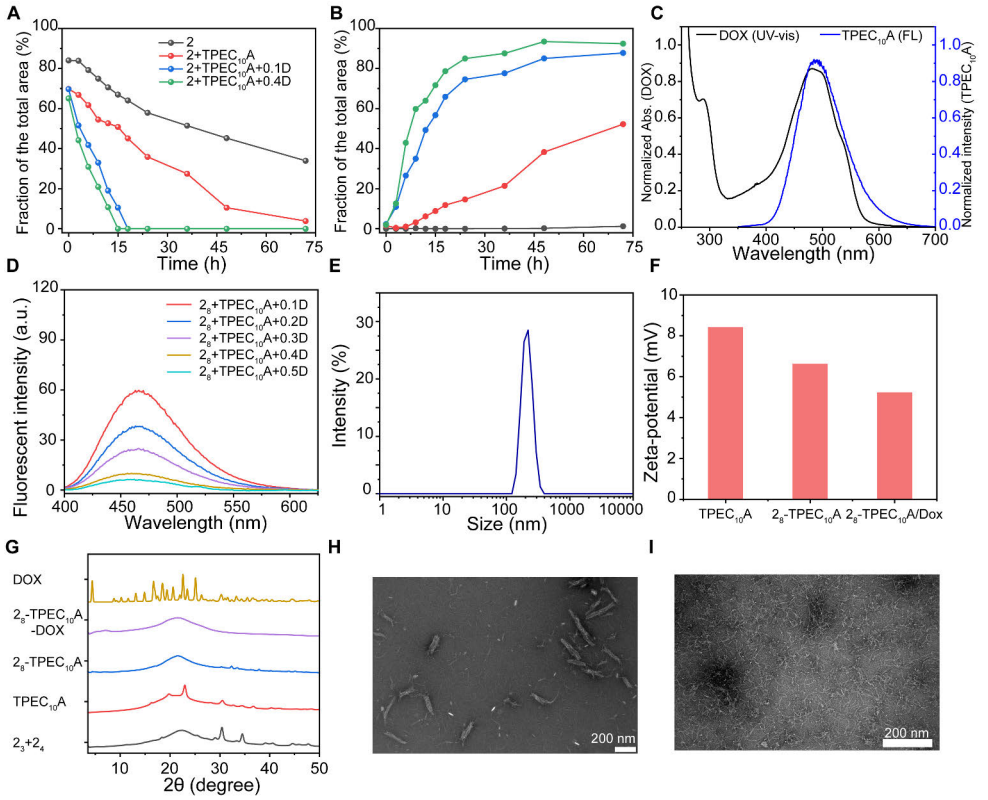

Figure 31. DOX-enhanced oxidation kinetics and structural characterization of **2$_8$-TPEC$_{10}$A**-DOX assemblies. (A) Consumption of building block **2** and (B) formation of **2$_8$** under different conditions: building block **2** alone (1.0 mM, black), **2-TPEC$_{10}$A** (1.0/0.25 mM, red), **2-TPEC$_{10}$A**-DOX (0.1 mM DOX, blue), and **2-TPEC$_{10}$A**-DOX (0.4 mM DOX, green). (C) UV–vis absorption spectrum of DOX and fluorescence spectrum of **TPEC$_{10}$A** (λ_{ex} = 330 nm), showing spectral overlap. (D) Fluorescence analysis of diluted **2$_8$-TPEC$_{10}$A**-DOX libraries containing **2$_8$**, **TPEC$_{10}$A**, and varying DOX equivalents in PBS buffer (50 mM, pH 7.4). (E) Hydrodynamic size distribution determined by DLS and (F) zeta potential **TPEC$_{10}$A**, **2$_8$-TPEC$_{10}$A**, and **2$_8$-TPEC$_{10}$A**-DOX assemblies. (G) PXRD patterns of **2$_3$+2$_4$**, **TPEC$_{10}$A**, **2$_8$-TPEC$_{10}$A**-DOX, optimized **2$_8$-TPEC$_{10}$A**-DOX, and DOX. (H) TEM image of **2$_8$-TPEC$_{10}$A**-DOX nanostructures and (I) TEM image after GSH treatment. Scale bar: 200 nm. Adapted from Original Publication II.

3.2.3.4 Redox and pH-responsive drug release behavior

Stimuli-responsive behavior of the **2_8-TPEC$_{10}$A**-DOX nanofiber bundles were next evaluated under physiologically relevant conditions. Drug release was negligible (<7%) at pH 7.4, indicating excellent stability under normal physiological conditions. In contrast, at pH 5.5 in the presence of 5 mM glutathione (GSH), the release of DOX reached approximately 80% within 24 hours. At acidic pH, protonation of carboxylate groups on **2_8** progressively weakens electrostatic interactions with the quaternary ammonium groups of **TPEC$_{10}$A**, destabilizing the nanofibers (**Figure 32A**). Simultaneously, the amine moieties of DOX become protonated, increasing its solubility and facilitating release (**Figure 32E**).

These results confirm that the nanofiber bundles are dually responsive to pH and redox stimuli, releasing its payload preferentially under intracellular or tumor-like conditions. Such controlled release behavior makes **2_8-TPEC$_{10}$A**-DOX a promising platform for targeted drug delivery and real-time imaging.

3.2.3.5 Cellular uptake and antiproliferative effects

The cytotoxicity of free DOX, **2_8-TPEC$_{10}$A**, and **2_8-TPEC$_{10}$A**-DOX was assessed using drug-resistant NCI/ADR-RES cells. Free DOX exhibited an IC_{50} of approximately 100 μM, whereas the **2_8-TPEC$_{10}$A**-DOX nanofiber bundles achieved an IC_{50} of 3.2 μM, representing a thirty-fold increase in cytotoxicity (**Figure 32B**). The enhanced efficacy arises primarily from the nanocarriers' ability to circumvent P-glycoprotein (P-gp) efflux and improve intracellular accumulation.

Flow cytometry confirmed that cellular uptake of free DOX was minimal (3-5% after 4 hours), whereas **2_8-TPEC$_{10}$A**-DOX achieved nearly 90% internalization within the same period (**Figure 32C**). This efficient uptake correlates with strong antiproliferative activity and apoptosis induction, as verified by Annexin V/PI staining (**Figure 32D**). These findings establish that preorganized AIE-based assemblies not only mediate catalytic synthesis but also provide functional nanocarriers for drug delivery in resistant cancer cells.

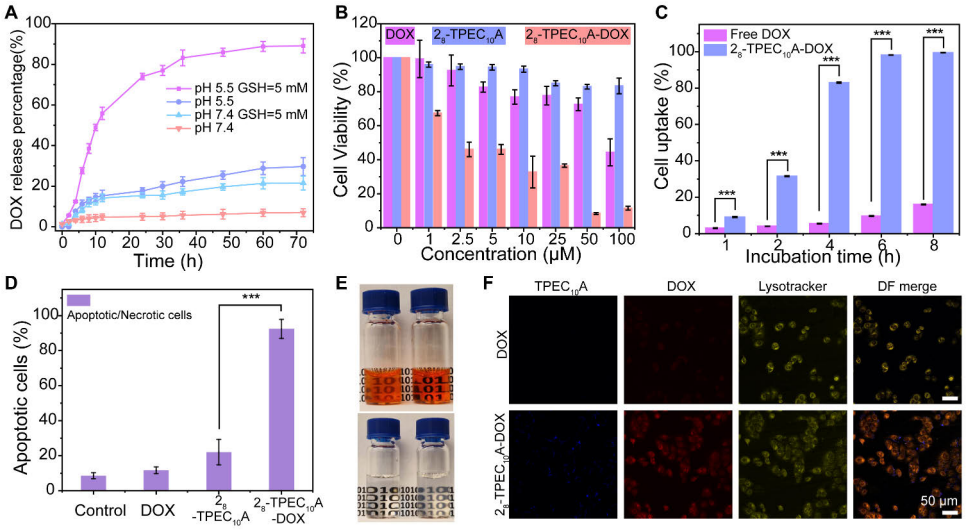

Figure 32. Enhanced antitumor activity of **2_8-TPEC$_{10}$A**-DOX nanofiber bundles. (A) Time-dependent release of DOX from **2_8-TPEC$_{10}$A**-DOX nanofiber bundles at 37 °C. (B) Antiproliferative activity of free DOX, **2_8-TPEC$_{10}$A** nanofibers, and **2_8-TPEC$_{10}$A**-DOX nanofiber bundles in drug-resistant NCI/RES-ADR cells determined by MTT assay. (C) Cellular uptake of free DOX and **2_8-TPEC$_{10}$A**-DOX (C_{DOX} = 10 μM) in NCI/RES-ADR cells quantified by flow cytometry at different incubation times. (D) Quantification of Annexin V-positive cells after 4 h treatment under different conditions. (E) Photographs showing pH-dependent dissolution of free DOX (0.5 mM) and **2_8** (0.125 mM) at pH 7.4 (left) and 5.5 (right). (F) Confocal fluorescence images of NCI/RES-ADR cells incubated with free DOX or **2_8-TPEC$_{10}$A**-DOX nanofiber bundles (C_{DOX} = 10 μM) for 4 h. Adapted from Original Publication II.

3.2.3.6 Real-time visualization of intracellular drug release

Confocal microscopy provided visual evidence of cellular uptake and drug release (**Figure 32F**). In NCI/ADR-RES cells treated with free DOX, only weak nuclear fluorescence was observed, indicating poor internalization. In contrast, cells incubated with **2_8-TPEC$_{10}$A**-DOX displayed bright fluorescence in both cytoplasm and nucleus after 4 hours. The blue fluorescence of **TPEC$_{10}$A** localized mainly in cytoplasmic vesicles, while the DOX fluorescence appeared in the nucleus, suggesting successful intracellular release of the drug. Co-staining with LysoTracker Deep Red confirmed that the majority of **TPEC$_{10}$A** and DOX signals colocalized within lysosomes prior to nuclear translocation, consistent with pH-triggered disassembly in acidic organelles.

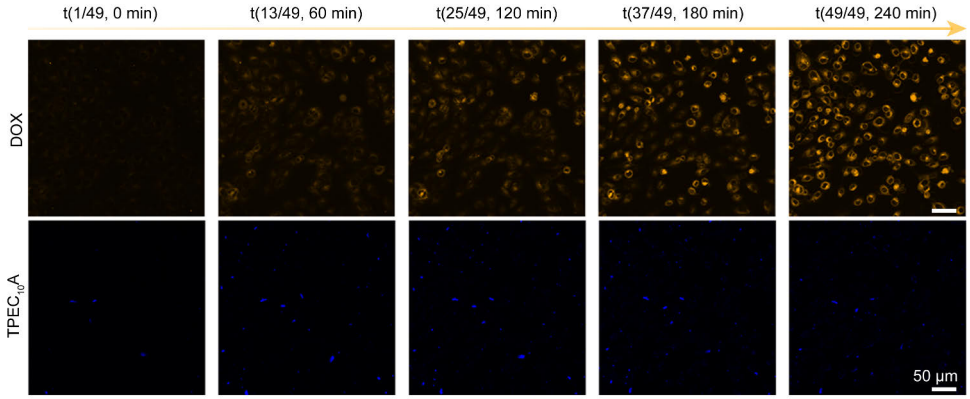

Figure 33. Real-time confocal imaging of intracellular drug release from **2_8-TPEC$_{10}$A**-DOX. Time-lapse confocal images were acquired every 5 min for 240 min to monitor the fluorogenic release process in drug-resistant NCI/RES-ADR cells incubated with **2_8-TPEC$_{10}$A**-DOX (C_{DOX} = 10 µM). Adapted from Original Publication II.

Real-time confocal imaging revealed dynamic fluorescence changes: initial darkness corresponding to intact, quenched nanofibers, followed by gradual brightening within 240 minutes as disassembly occurred (**Figure 33**). The appearance of "orange" and "blue" fluorescence from DOX and **TPEC$_{10}$A**, respectively, illustrated the synchronized activation of both components. Ultimately, DOX fluorescence emerged in the nucleus, confirming drug delivery to its target site.

These experiments demonstrate that **2_8-TPEC$_{10}$A**-DOX functions as a self-reporting nanosystem, in which entropy-controlled disassembly enables non-invasive, time-resolved visualization of drug release and intracellular transport. The combined catalytic, structural, and optical properties thus define an integrated chemical network operating at the interface of dynamic covalent chemistry and cellular biology.

3.2.4 Summary

In summary, an AIE-preorganized dynamic molecular network is established, in which aggregation-induced entropy reduction accelerates disulfide macrocyclization, thereby defining a general design principle for the generation of selective functional nanostructures. The cationic AIEgen **TPEC$_{10}$A** acted as an entropic template to direct oxidation of thiol building block **2**, leading to quantitative formation of the octameric macrocycle **2_8** and a morphological transition from micelles to nanofibers. Incorporation of the anticancer drug further reduced system entropy, enhanced the oxidation rate, and generated **2_8-TPEC$_{10}$A**-DOX nanofiber bundles with high drug-loading efficiency.

The resulting nanosystem exhibited dual responsiveness to pH and redox conditions, releasing DOX rapidly under acidic and reductive environments while remaining stable at physiological pH. In drug-resistant cancer cells, **2_8-TPEC_{10}A**-DOX enhanced cellular uptake, overcame P-gp mediated efflux, and restored DOX cytotoxicity by more than an order of magnitude. Moreover, its dual-color fluorescence allowed real-time visualization of intracellular drug release and trafficking, linking chemical dynamics directly to functional imaging.

Together, these results demonstrate the power of aggregation-induced entropy modulation as a design principle for constructing adaptive, multifunctional nanosystems that integrate chemical reactivity, supramolecular organization, and optical responsiveness, within the framework of dynamic systems chemistry, with implications for advanced biomedical applications.

3.3 Environment-Directed Selection and Chiral Memory in Micellar Dynamic Systems

Building on the findings that amphiphilic preorganization enables selective amplification and functional coupling in dynamic disulfide libraries, the next challenge is to explore whether similar amphiphilic principles can direct higher-order adaptive behaviors such as self-replication and molecular memory. Moving beyond product selectivity and functional response, this section examines how transient amphiphilic environments can act as external selective environments that bias replication, influence supramolecular chirality, and stabilize information within dynamic systems.

3.3.1 Introduction

The origin of life requires the spontaneous emergence of two interdependent properties: molecular self-replication, which enables information propagation and Darwinian evolution, and homochirality, which underlies the universal handedness of biological building blocks.[142, 143] While both phenomena are central to the transition from chemistry to biology, the mechanisms by which they arose concurrently from complex, prebiotic mixtures remain unresolved. Self-replicating molecules demonstrate the capacity for growth and selection, but without environmental stability they are often transient and easily lost to competing side reactions. Similarly, supramolecular chirality has been observed in artificial systems, yet its persistence typically requires continuous external input or templating.[144, 145] Reconciling these challenges demands chemical models that demonstrate how dynamic environments could foster both replication and chirality in a coupled and enduring manner.

Systems chemistry provides a powerful framework for addressing this question. In dynamic combinatorial libraries (DCLs), reversible covalent bonds enable mixtures of building blocks to interconvert continuously, with the potential for feedback-driven amplification of replicators under selective environmental pressures.[14] Previous studies have shown that replicators can arise spontaneously within DCLs and that chirality can emerge through supramolecular organization. However, how environmental factors can simultaneously direct the evolution of replicators and imprint persistent functional properties remains largely unexplored. The early Earth was rich in transient microenvironments such as drying lagoons, mineral surfaces, and amphiphilic compartments.[75, 146] Among these, surfactant micelles offer a particularly attractive model: they form spontaneously above critical concentrations, provide nanoscale confinement, and present tunable interfaces that can influence molecular organization. Yet, their role in driving replication and encoding supramolecular chirality has not been systematically investigated.

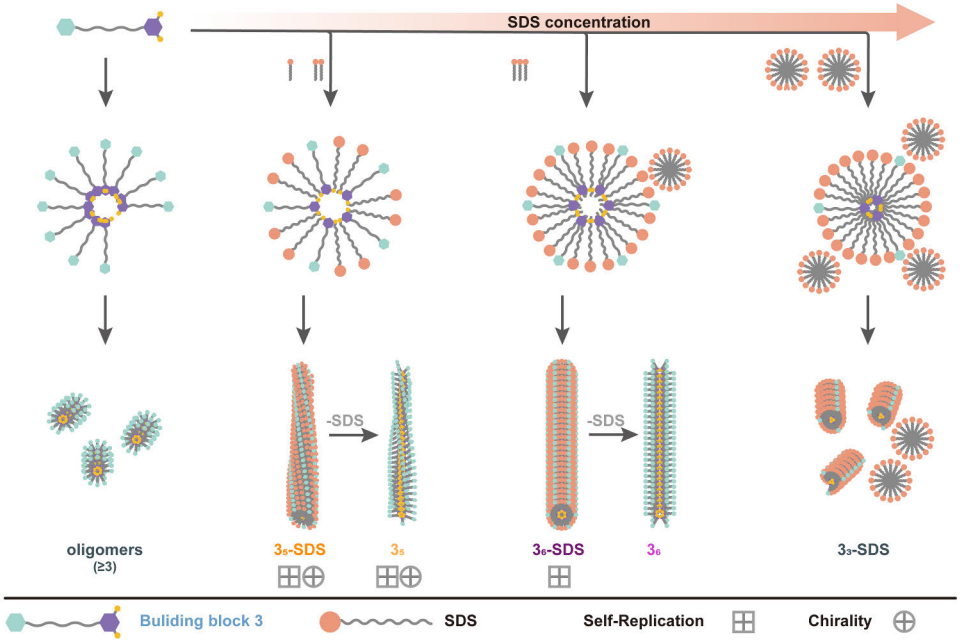

Figure 34. Micelle-directed self-replication and chiral memory in a dynamic disulfide system derived from building block **3**. Transient SDS micelles direct macrocycle selection and supramolecular assembly in a dynamic combinatorial library. Depending on surfactant concentration, distinct replicators emerge, with the pentamer (**3₅**) retaining both self-replication and supramolecular chirality after removal of the micellar environment.

In this section, we present a dynamic combinatorial system in which transient micellar environments guide both the topology and functionality of emergent

macrocyclic replicators (**Figure 34**). Using a mannose-functionalized thiol building block **3**, we demonstrate that sodium dodecyl sulfate (SDS) micelles selectively direct oxidation-driven macrocyclization toward pentameric ($\mathbf{3_5}$), hexameric ($\mathbf{3_6}$), or trimeric ($\mathbf{3_3}$) products depending on surfactant concentration. Notably, under conditions favoring $\mathbf{3_5}$, the system exhibits feedback-driven amplification, yielding twisted supramolecular fibers with a strong chiroptical response. Remarkably, $\mathbf{3_5}$ retains both self-replication and supramolecular chirality even after the removal of the SDS environment, establishing a form of molecular memory imprinted by an ephemeral scaffold. In contrast, $\mathbf{3_6}$ requires continuous environmental support and fails to persist once SDS is removed, highlighting the differential roles of environment-dependent and environment-independent replicators.

The objectives of this section are fourfold: (i) to demonstrate that micellar environments can selectively stabilize distinct macrocyclic topologies within a dynamic network, (ii) to investigate how environmental gating controls amplification kinetics and competitive outcomes, (iii) to reveal the emergence and persistence of supramolecular chirality in a topology-dependent manner, and (iv) to rationalize these phenomena using computational and environmental perturbation studies. Together, these findings provide a conceptual model for how transient amphiphilic environments can direct molecular evolution, imprinting persistent functions such as self-replication and supramolecular chirality that persist beyond their initial context.

3.3.2 Experimental section

3.3.2.1 Materials and general methods

All reagents and solvents were obtained from commercial suppliers and used without further purification unless otherwise specified. Borate buffer (50 mM, pH 7.4) was used as the standard aqueous medium unless otherwise stated. Ultrapure water (Milli-Q, 18.2 MΩ·cm) was used in all experiments.

3.3.2.2 Synthesis of building block **3**

The synthesis of building block **3** was carried out following adapted literature procedures (**Figure 35**).[147] Briefly, the thiol groups of building block **2** were protected using triphenylmethyl chloride (TrtCl), after which the carboxyl groups were activated with N-hydroxysuccinimide (NHS) to afford the corresponding activated ester (**2**-Trt-NHS). In parallel, D-mannose was peracetylated and functionalized with the appropriate bromoalcohol, followed by azide substitution and reduction to yield the corresponding amine. Coupling of the amine with the

activated ester afforded the protected conjugate, which was subjected to deacetylation and final trityl deprotection to yield building block **3**.

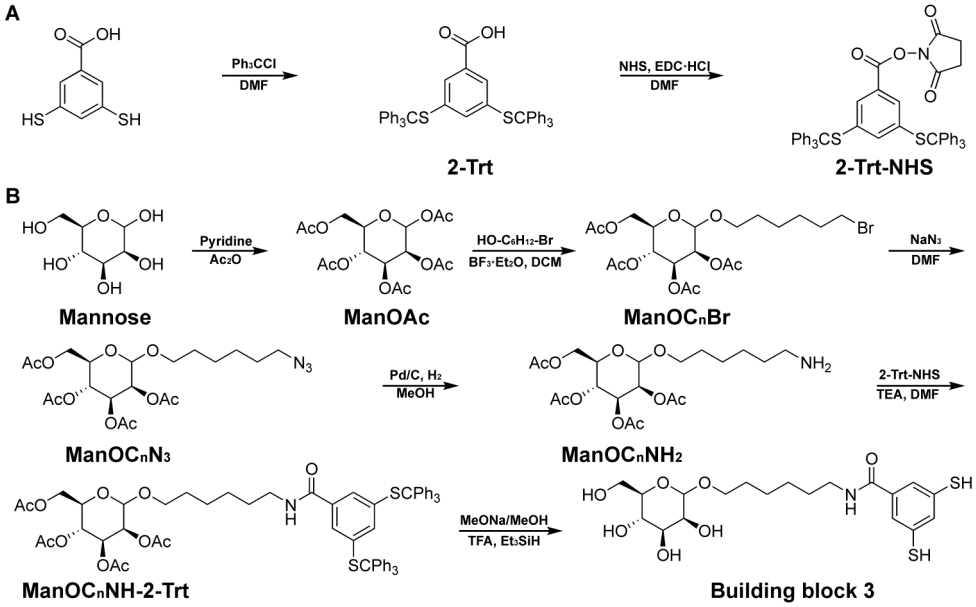

Figure 35. Scheme of the synthetic route of **2-Trt-NHS** and building block **3**.

Following synthesis, the chemical structures of building block **3** were confirmed by ^{1}H NMR and ^{1}H-^{1}H COSY spectroscopy and mass spectroscopy, as shown in **Figure 36**. COSY spectra were recorded in the presence of a small amount of dithiothreitol (DTT) to prevent disulfide formation.

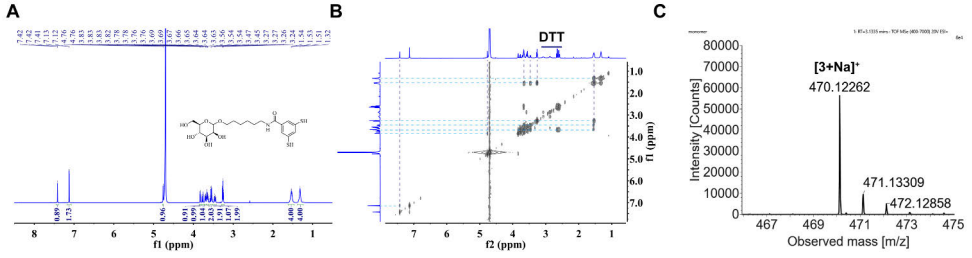

Figure 36. ^{1}H NMR and mass spectrometric characterization of building block **3**: (A) ^{1}H NMR spectrum. (B) ^{1}H-^{1}H COSY spectrum. (C) High-resolution mass spectrum (m/z calcd for $C_{18}H_{27}NO_7S_2Na^+$ [**3**+Na]$^+$ 470.1278; found 470.1226).

3.3.2.3 Oxidation of dynamic combinatorial libraries

Oxidation-driven dynamic combinatorial libraries were generated from building block **3** under unbiased ambient conditions. Unless otherwise stated, stock solutions of building block **3** (10 mM) were freshly prepared in borate buffer (50 mM, pH 7.4) and diluted to a working concentration of 2.0 mM for oxidation experiments. Oxidation was carried out in 2 mL glass vials at room temperature under continuous stirring (700 rpm). The reaction vessels were loosely capped, and the time point at which stirring was initiated was defined as t = 0 h. At each time point, a small aliquot (2 µL) was withdrawn from the reaction mixture, resulting in negligible perturbation of the total reaction volume and oxidation conditions.

For experiments performed in the presence of surfactants, sodium dodecyl sulfate (SDS) or other surfactants were added from concentrated aqueous stock solutions prior to oxidation to achieve the desired building block **3**:surfactant ratios. For stepwise SDS addition experiments, the total amount of SDS was introduced in predefined increments at specified time points during oxidation, while maintaining the same final SDS concentration and stirring conditions. Time-dependent aliquots were analyzed directly or after appropriate treatment, depending on the analytical technique employed. For experiments requiring surfactant-free conditions, SDS was removed using detergent-removal spin columns.

Partial oxidation states (e.g., approximately 70% oxidation) were obtained by allowing oxidation to proceed for a defined period determined from preliminary kinetic measurements. Fully oxidized libraries were obtained by allowing oxidation to proceed until no further changes in product distribution were detected by UPLC analysis over consecutive sampling points, consistent with the operational definition of compositional stability applied in this study.

3.3.2.4 UPLC and UPLC–MS analysis

UPLC and UPLC–MS analyses were performed under reversed-phase conditions using water and methanol containing 0.1% (v/v) trifluoroacetic acid as mobile phases. UV detection was carried out at 254 nm. The column temperature was maintained at 40 °C, and samples were stored at 10 °C prior to injection. UPLC–MS measurements were conducted using electrospray ionization in positive ion mode.

3.3.2.5 Removal of SDS from samples

Residual sodium dodecyl sulfate (SDS) was removed from oxidized samples (150 µL) using DetergentOUT™ GBS10-800 spin columns according to the manufacturer's protocol. This procedure was chosen because it allows rapid surfactant depletion under mild aqueous conditions while minimizing dilution,

avoiding prolonged dialysis, and preserving fragile oxidized macrocycle assemblies for direct comparison before and after surfactant removal. Prior to sample loading, the columns were equilibrated with equilibration buffer and centrifuged at 1000 × g for 1 min, and this equilibration step was repeated once. Each sample was then applied to the column and incubated at room temperature for 2 min, followed by centrifugation at 1000 × g for 2 min to collect the detergent-free eluate. The efficiency of SDS removal was verified subsequently by ^{1}H NMR analysis after DTT reduction, which showed disappearance of the characteristic SDS resonances, while UPLC analysis confirmed that the macrocyclic distribution was retained during the procedure. The resulting solutions were used directly for subsequent spectroscopic and microscopic analyses.

3.3.2.6 Seeding experiments

Seeding experiments were performed using macrocyclic species isolated from SDS-guided dynamic combinatorial libraries. Two types of seeds were employed, depending on the experimental design. For experiments probing the influence of environmental compatibility, macrocycle seeds were used directly in their SDS-associated form and introduced into freshly prepared oxidation systems containing SDS at defined concentrations.

For experiments designed to evaluate intrinsic, topology-dependent replication in the absence of persistent environmental support, macrocycle seeds were first subjected to SDS removal using detergent-removal spin columns prior to seeding. The resulting SDS-depleted macrocycle seeds were then introduced into freshly prepared or partially oxidized solutions of building block **3** under surfactant-free conditions. Unless otherwise stated, seeds were added at defined molar fractions relative to the total concentration of building block **3**, and the subsequent evolution of product distributions was monitored by UPLC as described above.

3.3.2.7 Computational methods

Molecular dynamics (MD) simulations were performed using GROMACS with the General AMBER Force Field (GAFF2) and the TIP3P water model. Model assemblies composed of three, five, or six building blocks were constructed and solvated, with SDS molecules and counterions added to neutralize the systems. After energy minimization and equilibration, production runs were carried out under NPT conditions at 298 K and 1 atm. Long-range electrostatics were treated using the particle mesh Ewald method, and hydrogen bonds were analyzed using standard geometric criteria.

Density functional theory (DFT) calculations were carried out using the projector augmented-wave method as implemented in VASP, employing the PBE exchange–correlation functional with DFT-D3 dispersion corrections. A plane-wave cutoff energy of 480 eV was used, and structural optimizations were performed until the residual forces were below 0.05 eV $Å^{-1}$. Formation energies were calculated based on the optimized structures to provide qualitative energetic comparisons among different macrocyclic topologies.

3.3.3 Results and discussion

3.3.3.1 Micellar environments regulate dynamic macrocycle formation

To evaluate how amphiphilic environments influence oxidation-driven dynamic networks, the mannose-functionalized dithiol building block **3** (2 mM) was oxidized in borate buffer (50 mM, pH 7.4) under ambient conditions. Upon oxidation, the reaction mixture rapidly became turbid, consistent with the formation of colloidal aggregates (**Figure 37**), which precluded reliable analysis by solution-phase techniques. A marked decrease in UPLC peak intensities was observed; however, treatment of the oxidized mixture with increasing concentrations of dithiothreitol (DTT) resulted in a gradual recovery of peak areas, reaching a plateau at higher reductant concentrations (**Figure 37A** and **37B**), consistent with the reversibility of disulfide formation.

MALDI-TOF MS further revealed a broad distribution of thiol-terminated oligomeric species corresponding to assemblies composed of approximately 3–10 units of building block **3** (m/z 1360.37–4480.31 Da), without a dominant macrocycle, indicative of unselective oxidation and uncontrolled polymerization (**Figure 37C**). The presence of residual thiol termini indicates incomplete cyclization and the formation of open-chain oligomers rather than discrete cyclic macrocycles. Cryogenic transmission electron microscopy indicated the presence of irregular, worm-like aggregates under surfactant-free conditions, while circular dichroism measurements showed no detectable optical activity. These observations suggest that, in the absence of a micellar environment, oxidation leads to nonspecific aggregation rather than the formation of ordered supramolecular architectures.

When sodium dodecyl sulfate (SDS) was added, the oxidation process and product distribution changed markedly. The solutions remained clear and stable over several months (**Figure 37D**), and discrete macrocyclic species were detected depending on SDS concentration (**Figure 38**). These results demonstrate that micellar environments suppress random aggregation and act as selective environments that channel oxidation toward specific macrocyclic topologies.

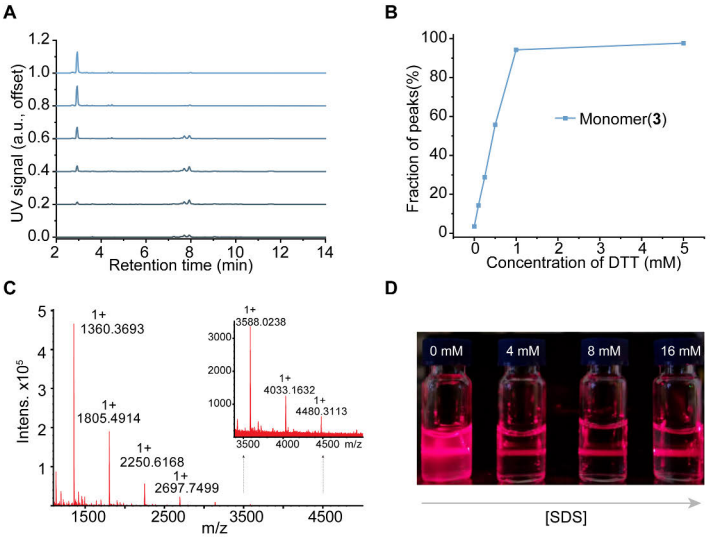

Figure 37. Reductive recovery and compositional analysis of oxidation products derived from building block **3**. (A) UPLC traces of the oxidized assemblies derived from building block 3 after treatment with increasing concentrations of dithiothreitol (DTT), showing the gradual recovery of soluble species. (B) Fraction of building block **3** recovered after reduction, normalized to the signal intensity at the highest DTT concentration (5 mM), indicating saturation behavior consistent with reversible disulfide formation. (C) MALDI-TOF mass spectrum of the oxidized library, revealing a homologous series of thiol-terminated oligomeric species spanning approximately 3–10 units of building block **3** (m/z 1360.37–4480.31). (D) Representative photographs of solutions of building block **3** (2 mM) after oxidation in the absence and presence of SDS at increasing concentrations (0, 4, 8, and 16 mM).

3.3.3.2 Concentration-dependent topology selection within the dynamic network

Oxidation of building block **3** (2.0 mM) was performed at SDS concentrations ranging from 0 to 16 mM, encompassing submicellar, micellar, and supramicellar regimes. At 4 mM SDS, UPLC–MS revealed the pentameric macrocycle $\mathbf{3_5}$ as the dominant product (**Figure 38G–J**). Increasing the SDS concentration to 8 mM, near the critical micellar concentration (CMC ≈ 8.2 mM), shifted the equilibrium toward the hexameric species ($\mathbf{3_6}$) (**Figure 38K–N**). At 16 mM SDS, beyond the CMC, a well-defined UPLC peak was observed at a retention time corresponding to that of the trimeric macrocycle $\mathbf{3_3}$ identified under SDS-free conditions (**Figure 38C–F**). This concentration-dependent outcome defines three distinct selection regimes: low SDS favoring $\mathbf{3_5}$, intermediate SDS favoring $\mathbf{3_6}$, and high SDS promoting the re-emergence of trimeric species with retention times characteristic of $\mathbf{3_3}$.

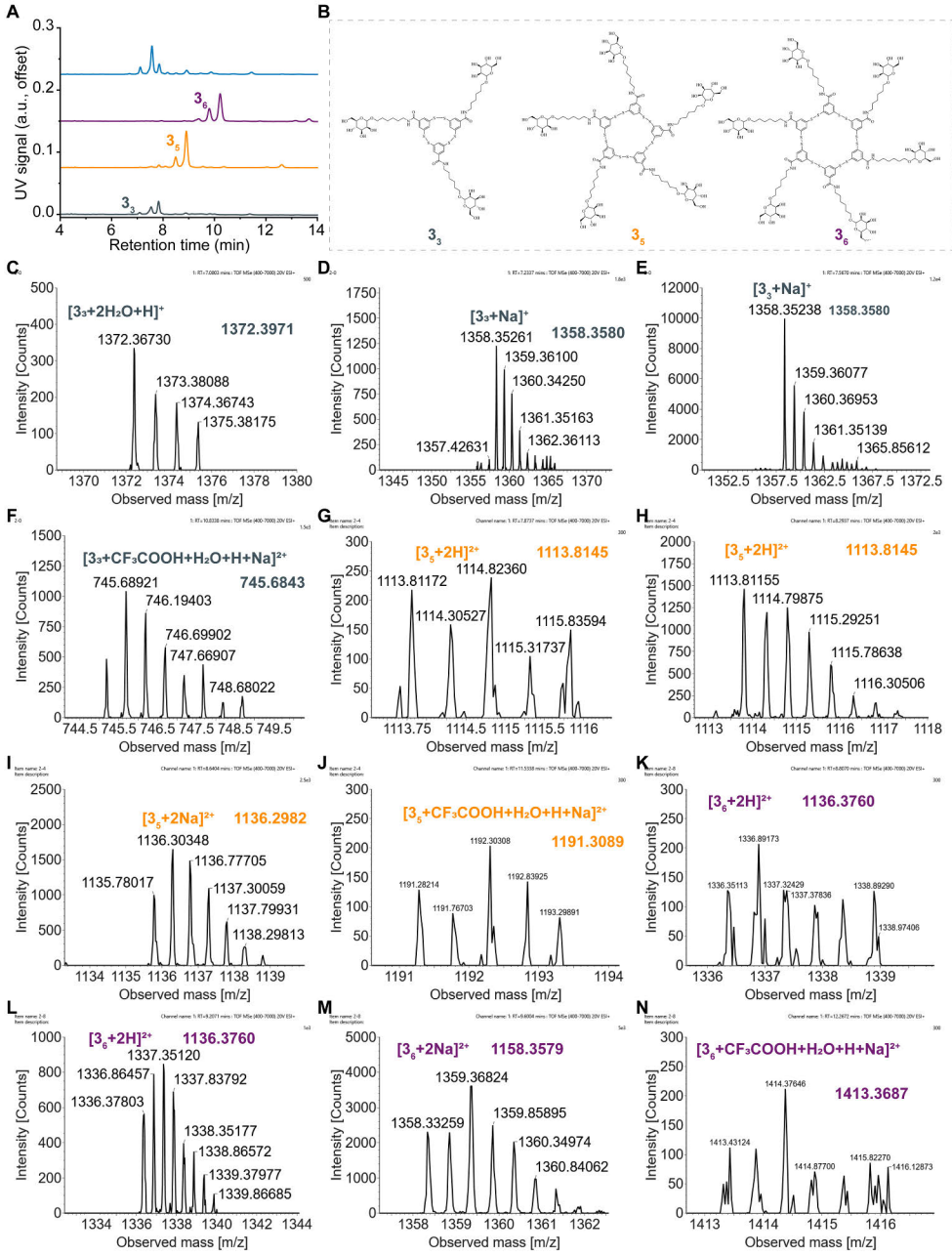

Figure 38. (A) UPLC traces of oxidation products of building block **3** (2.0 mM) obtained at increasing SDS concentrations, showing SDS-dependent changes in macrocycle distribution. Peaks corresponding to $\mathbf{3_3}$, $\mathbf{3_5}$, and $\mathbf{3_6}$ are indicated. (B) Molecular structures of $\mathbf{3_3}$, $\mathbf{3_5}$, and $\mathbf{3_6}$ derived from building block **3**. (C–F) UPLC–MS spectra of peaks eluting at retention times assigned to $\mathbf{3_3}$. (G–J) UPLC–MS spectra of peaks eluting at retention times assigned to $\mathbf{3_5}$, (K–N) UPLC–MS spectra of peaks eluting at retention times assigned to $\mathbf{3_6}$.

A phase diagram summarizing the relationship between building block **3** (0.5–8 mM) and SDS (0–16 mM), constructed from the SDS-dependent product distributions, clearly delineates the observed topology transitions (**Figure 39F**). At a fixed concentration of building block **3** (for example, 2 mM), the distribution of oxidation products varies markedly with increasing SDS concentration. Under surfactant-free or very low SDS conditions, a pronounced decrease in overall UPLC peak intensity was observed, consistent with incomplete oxidation and the formation of nonspecific oligomeric aggregates. Upon increasing the SDS concentration, the reaction became increasingly selective toward the pentameric macrocycle $\mathbf{3_5}$ (**Figure 36C**). Further addition of SDS led to a coexistence regime in which both $\mathbf{3_5}$ and $\mathbf{3_6}$ were present, accompanied by a gradual decrease in the fraction of $\mathbf{3_5}$ and a corresponding increase in that of $\mathbf{3_6}$. At higher SDS concentrations, the hexameric macrocycle $\mathbf{3_6}$ became the dominant product. Upon further increasing SDS concentration, a transition from $\mathbf{3_6}$ to $\mathbf{3_3}$ was observed, as the fraction of $\mathbf{3_6}$ decreased while the trimeric macrocycle $\mathbf{3_3}$ became predominant.

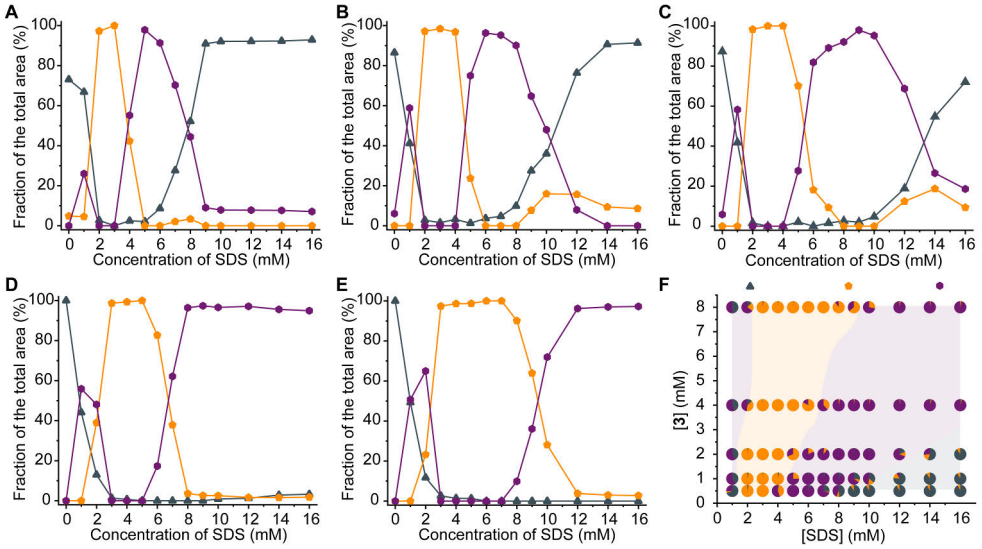

Figure 39. SDS-dependent macrocycle distributions and phase diagram for oxidation of building block **3** in borate buffer (50 mM, pH 7.4). (A–E) Fractional distributions of macrocyclic species as a function of SDS concentration for different total concentrations of building block **3**: (A) 0.5 mM, (B) 1.0 mM, (C) 2.0 mM, (D) 4.0 mM, and (E) 8.0 mM. The relative abundance of each macrocycle was determined from normalized UPLC peak areas, illustrating SDS-dependent topology transitions at each building block concentration. (F) Phase diagram summarizing the SDS-dependent topology transitions as a function of both building block **3** concentration and SDS concentration, constructed from the product distributions shown in panels A–E.

Increasing the concentration of building block **3** did not alter the overall sequence of SDS-dependent topology transitions; however, the SDS concentration ranges associated with each macrocycle distribution expanded noticeably. Collectively, these results indicate that SDS micelles not only facilitate oxidation but also act as dynamic templates that direct macrocycle topology through nanoscale confinement and interfacial organization.

3.3.3.3 Environment-gated kinetics and amplification behavior

Time-dependent oxidation studies were conducted to examine how environmental organization influences the kinetics of macrocycle formation. In the absence of SDS, the UPLC peak area of the monomeric building block gradually decreased over time, while no corresponding increase in well-defined macrocyclic products was detected. Near-complete consumption of the monomer into nonselective oligomeric species was observed after approximately 12 days. Accordingly, under surfactant-free conditions, only the decay of the monomeric species is shown (**Figure 40A**). At 4 mM SDS, the concentration of the pentamer $\mathbf{3_5}$ increased following a sigmoidal growth profile characteristic of autocatalytic amplification (**Figure 40B**). After an induction period of approximately 24 h, a phase of rapid growth was observed, followed by saturation after about 9 days. In addition to the pentamer, small but appreciable amounts of the trimeric macrocycle $\mathbf{3_3}$ were also generated at early reaction times. Notably, a small fraction of hexameric species $\mathbf{3_6}$ was transiently observed at early reaction times (up to 12%); however, this species was not sustained as the pentamer $\mathbf{3_5}$ underwent rapid amplification. The implications of this transient coexistence were further examined in the subsequent competition experiments.

At 8 mM SDS (**Figure 40C**), the time course displayed a sigmoidal amplification profile analogous to that observed at 4 mM SDS, but with the hexameric macrocycle $\mathbf{3_6}$ emerging as the dominant product. Appreciable transient populations of both the trimeric macrocycle $\mathbf{3_3}$ (up to ~28%) and the pentamer $\mathbf{3_5}$ were detected at early reaction times, before diminishing as $\mathbf{3_6}$ accumulated. By contrast, at 16 mM SDS (**Figure 40D)**, the trimeric macrocycle $\mathbf{3_3}$ increased steadily over time and reached a plateau, without exhibiting a pronounced sigmoidal growth profile.

The sigmoidal amplification behavior observed for the pentameric $\mathbf{3_5}$ and hexameric $\mathbf{3_6}$ macrocycles at intermediate SDS concentrations suggests the presence of environment-enabled, feedback-driven growth processes within the micellar environment. However, such kinetic signatures alone do not resolve whether amplification originates from micelle-mediated environmental stabilization or from intrinsic, topology-encoded self-replication. To clarify this distinction, we first examined how seed identity and environmental conditions jointly influence network evolution under SDS-containing conditions.

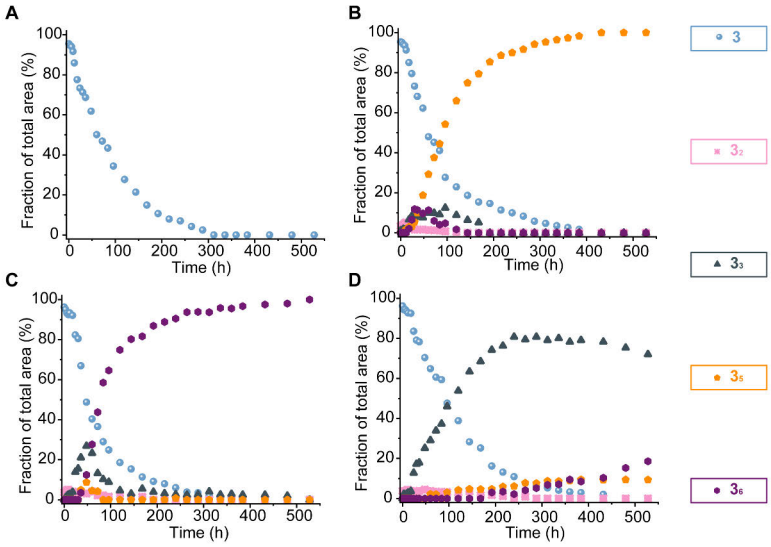

Figure 40. Oxidation kinetics of building block **3** under different SDS concentrations. Time-dependent evolution of oxidation products derived from building block **3** (2.0 mM) in borate buffer (50 mM, pH 7.4), monitored by UPLC and quantified as the fraction of total peak area. (A) In the absence of SDS (0 mM), the overall UPLC signal decreased substantially over time due to aggregation and loss of soluble material; therefore, only the decay of the monomeric building block **3** is shown. (B) 4 mM SDS. (C) 8 mM SDS. (D) 16 mM SDS.

To this end, cross-seeding experiments were performed in which preformed macrocycles derived from SDS-guided dynamic combinatorial libraries were introduced into oxidation systems that intrinsically favor an alternative topology. When $\mathbf{3_6}$ seeds were introduced into a **3**:SDS = 2 mM:4 mM system, which normally favors formation of $\mathbf{3_5}$, the product distribution was redirected toward $\mathbf{3_6}$ (**Figure 41A**). In contrast, $\mathbf{3_5}$ seeds failed to override the environmental preference at **3**:SDS = 2mM:8 mM, and $\mathbf{3_6}$ remained the dominant species throughout the reaction (**Figure 41B**). These results reveal a pronounced directional asymmetry, demonstrating that environmental compatibility can supersede seed identity in determining macrocycle outcome under micelle-guided conditions.

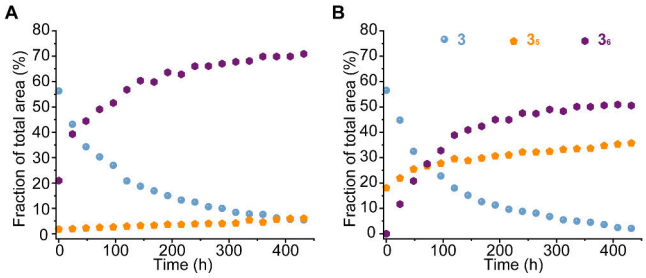

Figure 41. Seeded oxidation kinetics of macrocycles $\mathbf{3_5}$ and $\mathbf{3_6}$ derived from SDS-guided dynamic combinatorial libraries. (A) Time-dependent evolution of the macrocycle distribution in a DCL at **3**:SDS = 2 mM:4 mM seeded with 25% $\mathbf{3_6}$, showing progressive enrichment of $\mathbf{3_6}$ during oxidation. (B) Time-dependent evolution of the macrocycle distribution in a DCL at **3**:SDS = 2 mM:8 mM seeded with 25% $\mathbf{3_5}$, where $\mathbf{3_6}$ remains the dominant species over time. Product distributions are expressed as fractions of the detectable total UPLC peak area at each time point.

Beyond seed identity, we next investigated whether the temporal mode of environmental input influences macrocycle selection. Under otherwise identical final conditions (**3**:SDS = 2 mM:8 mM), a single, one-step addition of SDS led exclusively to $\mathbf{3_6}$ formation. By contrast, stepwise SDS addition resulted in mixed product distributions, and partitioning the total SDS input into three increments yielded a final $\mathbf{3_5}$:$\mathbf{3_6}$ ratio of approximately 60%:20% (**Figure 42**). These observations demonstrate a kinetic gating effect, whereby transient amplification during early stages of oxidation biases the final topology. Once established, the resulting distribution resists subsequent re-equilibration, indicating that the system encodes a memory of its environmental trajectory through feedback-stabilized growth.

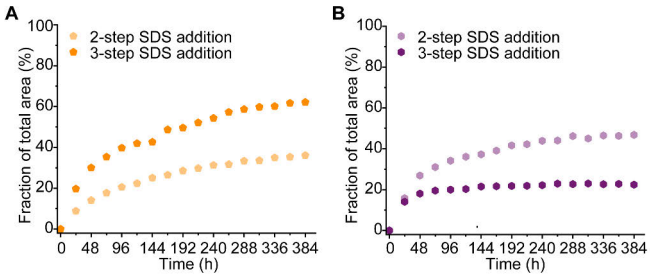

Figure 42. Kinetic evolution of macrocycle distributions under stepwise SDS addition. A) Time-dependent formation of the pentameric macrocycle $\mathbf{3_5}$ under different SDS addition protocols. (B) Time-dependent formation of the hexameric macrocycle $\mathbf{3_6}$ under identical conditions. In all cases, the final SDS concentration corresponds to a **3**:SDS ratio of 2 mM:8 mM.

Together, the cross-seeding experiments and stepwise SDS addition studies demonstrate that macrocycle amplification and topology selection under SDS-containing conditions are strongly influenced by environmental compatibility and kinetic history. While feedback-driven growth is clearly observed, these results do not yet distinguish whether amplification reflects intrinsic, topology-encoded self-replication or arises predominantly from micelle-mediated environmental stabilization. To address this question, we next investigated the replication behavior of isolated macrocycles by systematically varying the presence of the surfactant environment during seeding. Specifically, two complementary seeding conditions were examined: seeding with macrocycles retained in their SDS-associated form under SDS-containing conditions, and seeding with macrocycles from which SDS was subsequently removed to evaluate replication behavior in the absence of external surfactant templating.

3.3.3.4 Self-replication versus environmental stabilization of $\mathbf{3_5}$ and $\mathbf{3_6}$ macrocycles

To examine whether amplification behavior arises from transient environmental templating or intrinsic macrocycle topology,[146] controlled seeding experiments were performed in the absence of externally added SDS. Preformed macrocycles, isolated from SDS-guided dynamic combinatorial libraries, were introduced into solutions of building block **3** at defined molar fractions (5%, 10%, or 25%), with the total concentration of building block **3** maintained at 2 mM. Although trace SDS may remain from purification, no additional surfactant was added, allowing the evaluation of topology-dependent replication under near-template-free conditions.

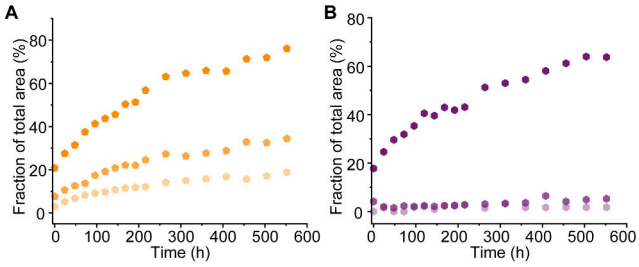

Figure 43. Seeded oxidation kinetics of macrocycles $\mathbf{3_5}$ and $\mathbf{3_6}$ derived from SDS-guided dynamic combinatorial libraries. (A) Time-dependent evolution of the fraction of pentameric macrocycle $\mathbf{3_5}$ during oxidation of building block **3** (total concentration 2 mM) following seeding at different molar fractions (5%, 10%, and 25%). (B) Corresponding time-dependent evolution of the fraction of hexameric macrocycle $\mathbf{3_6}$ under identical conditions. Product distributions are expressed as fractions of the detectable total UPLC peak area at each time point.

Seeding with the pentameric macrocycle **3_5**, derived from SDS-guided libraries, resulted in clear seed concentration-dependent amplification. At 25% seeding, the yield increased from 20.8% to 76.1% after 552 hours (**Figure 43A**), while lower seed levels produced proportionally weaker responses. Nevertheless, even at the lowest seed fractions, a gradual but measurable increase in the **3_5** population was observed over time. Although the kinetics lacked cooperativity, the sustained and topology-specific propagation in the absence of added SDS indicates that **3_5** encodes sufficient structural memory to support autonomous, topology-encoded replication.

In contrast, seeding with the hexameric macrocycle **3_6** did not result in seed concentration-dependent amplification. At low seed fractions (5% and 10%), the fraction of **3_6** remained essentially unchanged over time, accompanied by a decrease in the overall UPLC peak area similar to that observed for oxidation of the building block under surfactant-free conditions. Although an increase in the **3_6** fraction was observed at 25% seeding, this response rapidly reached a plateau at approximately 63.7% and was not accompanied by measurable growth at lower seed levels or evidence of feedback-driven acceleration (**Figure 43B**). Collectively, these observations indicate that **3_6** lacks intrinsic replicative capacity and is instead stabilized by high initial loading or environmental organization rather than autonomous propagation.

To further clarify the role of the surfactant environment, residual SDS in the preformed macrocycle seeds was removed using a commercial detergent removal column prior to seeding. As shown in **Figure 44A** and **44B**, ^{1}H NMR spectra recorded after detergent removal, as well as after subsequent DTT reduction, showed no detectable SDS signals, confirming effective surfactant removal. Importantly, UPLC analysis revealed no significant change in total peak area before and after SDS removal (**Figure 44C**), indicating that the macrocyclic material was preserved. Together, these results demonstrate that this procedure yields SDS-free macrocycle seeds suitable for subsequent seeding experiments.

The resulting SDS-depleted macrocycle seeds were then introduced into both freshly oxidizing monomer solutions and partially oxidized mixtures (≈ 70% oxidation) to assess whether macrocycle amplification is sustained through intrinsic structural feedback or requires external surfactant templating. In freshly oxidizing systems, the fraction of **3_5** reached 89.3% within 264 hours at 25% seeding (**Figure 45A**), while a comparable fraction of 89.8% was obtained with 50% seeding under the same conditions.

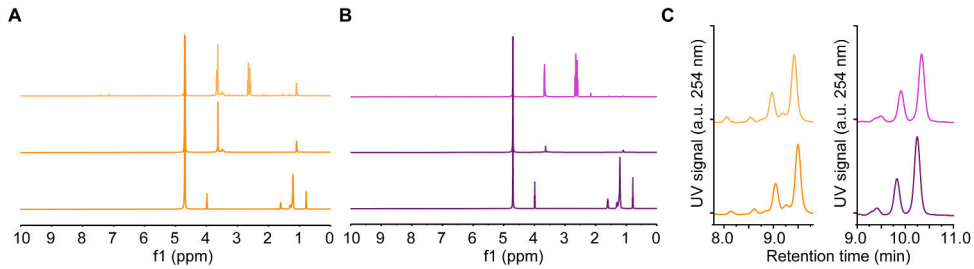

Figure 44. Evaluation of SDS removal from SDS-guided dynamic combinatorial libraries using commercial removal column. (A) ^{1}H NMR spectra of samples derived from oxidation of building block **3** in the presence of 4 mM SDS. From bottom to top: ^{1}H NMR spectrum of SDS; spectrum after treatment with SDS removal column, showing no detectable signals; and spectrum after SDS removal followed by DTT reduction, revealing resonances corresponding to building block **3**. (B) ^{1}H NMR spectra of samples derived from oxidation of building block **3** in the presence of 8 mM SDS. From bottom to top: ^{1}H NMR spectrum of SDS; spectrum after treatment with SDS removal column, showing no detectable signals; and spectrum after SDS removal followed by DTT reduction, revealing resonances corresponding to building block **3**. Minor residual signals observed in spectra arise from trace organic solvents present in the removal column. (C) UPLC traces recorded before (bottom) and after (top) SDS removal for DCLs generated at 4 mM SDS (left, predominantly $\mathbf{3_5}$) and 8 mM SDS (right, predominantly $\mathbf{3_6}$), indicating no significant loss of total peak area upon SDS removal.

When $\mathbf{3_5}$ was seeded into partially oxidized mixtures, amplification was still observed but the extent of growth depended on the seed loading (**Figure 45B**). The higher plateau reached at 50% seeding likely arises from the large initial population of $\mathbf{3_5}$, which biases the final product distribution under conditions where the pool of exchange-competent building blocks is limited. In contrast, at lower seed loadings (25%), amplification of $\mathbf{3_5}$ becomes constrained by the reduced availability of dynamically accessible species, resulting in earlier saturation at a lower plateau. This behavior is consistent with the oxidation-driven kinetic experiments described above, which showed that topology redistribution can occur during oxidation but becomes progressively restricted as the system approaches higher oxidation states.

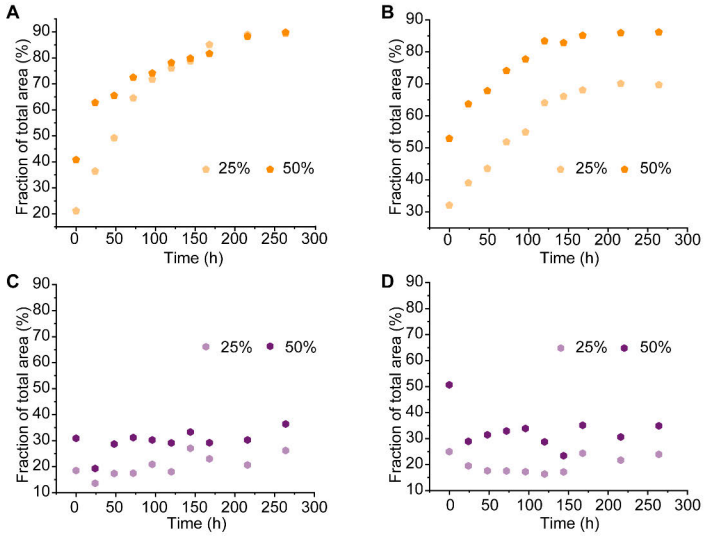

Figure 45. Seeding experiments using SDS-depleted macrocycle seeds. (A, B) Seeding with SDS-depleted $\mathbf{3_5}$ (25% and 50%) into freshly prepared (A) and partially oxidized (≈ 70%, B) solutions of building block **3** (total concentration 2 mM). (C, D) Seeding with SDS-depleted $\mathbf{3_6}$ (25% and 50%) under identical conditions. Product distributions are expressed as fractions of the detectable total UPLC peak area over time.

By contrast, seeding with SDS-depleted $\mathbf{3_6}$ did not result in sustained amplification under either freshly oxidizing or partially oxidized conditions (**Figure 45C** and **45D**). At both 25% and 50% seeding, the fraction of $\mathbf{3_6}$ remained largely constant over time, with only minor fluctuations and no clear trend toward enrichment. In parallel, a gradual decrease in the overall detectable UPLC peak area was observed, similar to that seen during oxidation of the building block under surfactant-free conditions, indicating that in the absence of a surfactant environment, $\mathbf{3_6}$ does not undergo sustained propagation or enrichment but is progressively redistributed into poorly detected oligomeric species.

To assess competitive fitness, $\mathbf{3_5}$ and $\mathbf{3_6}$ were co-introduced at equal molar fractions (25% each) into a fresh solution of building block **3** (**Figure 46A**). Initially, both species were present in comparable amounts; however, over time $\mathbf{3_5}$ amplified to 76.3%, whereas $\mathbf{3_6}$ declined to 2.4%. Despite identical initial abundance, $\mathbf{3_5}$ rapidly dominated the network, underscoring its superior autonomous replicative persistence (**Figure 46B**).

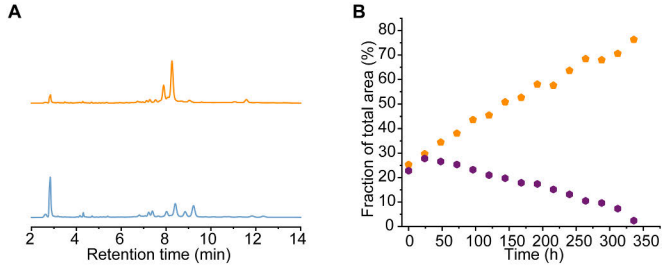

Figure 46. Competitive seeding between $\mathbf{3_5}$ and $\mathbf{3_6}$ under SDS-depleted conditions. (A) UPLC chromatograms recorded before (bottom) and after oxidation (top) of building block **3** (2 mM) in the presence of competing SDS-depleted $\mathbf{3_5}$ and $\mathbf{3_6}$ seeds (25% each). (B) Time-dependent evolution of the relative fractions of $\mathbf{3_5}$ and $\mathbf{3_6}$ during oxidation under competitive seeding conditions.

Together, these findings establish $\mathbf{3_5}$ as a topology-encoded self-replicator capable of dominating network evolution through structural stability and feedback-driven amplification.[13] In contrast, $\mathbf{3_6}$ relies on environmental templating and lacks autonomous persistence under SDS-depleted conditions. This pronounced competitive asymmetry illustrates how directional selection, heredity, and history dependence can emerge within minimal chemical networks.

3.3.3.5 Micellar microenvironments modulate monomer dynamics and network topology

To rationalize how subtle differences in SDS concentration bias the outcome of macrocyclization and, ultimately, dynamic network topology, we examined the behavior of building block **3** under various micellar conditions prior to oxidation.[121] Following oxidation, the ^{1}H NMR signals corresponding to the monomeric building block become extensively broadened and unresolved, rendering the monomeric species no longer amenable to direct ^{1}H NMR analysis. Consequently, characterization of the system prior to oxidation provides the most direct and informative spectroscopic window for probing how micellar environments preorganize the monomer pool and bias subsequent network formation.

^{1}H NMR spectra of building block **3** recorded in the presence of increasing SDS concentrations revealed pronounced, concentration-dependent chemical shift perturbations (**Figure 47**). At 4 mM SDS, the aromatic proton resonances exhibited noticeable, site-specific shifts relative to surfactant-free conditions, consistent with a microenvironmental transition associated with the onset of micellar association. Above 8 mM SDS, these shifts plateaued, indicating incorporation of building block **3** into a micelle-dominated regime. In contrast, the –OCH_2– and terminal –CH_3 resonances of SDS exhibited only minor, concentration-dependent chemical shift

changes that were comparable in the absence and presence of building block **3**, indicating that these variations primarily reflect surfactant-driven micellar organization rather than perturbation induced by the building block.

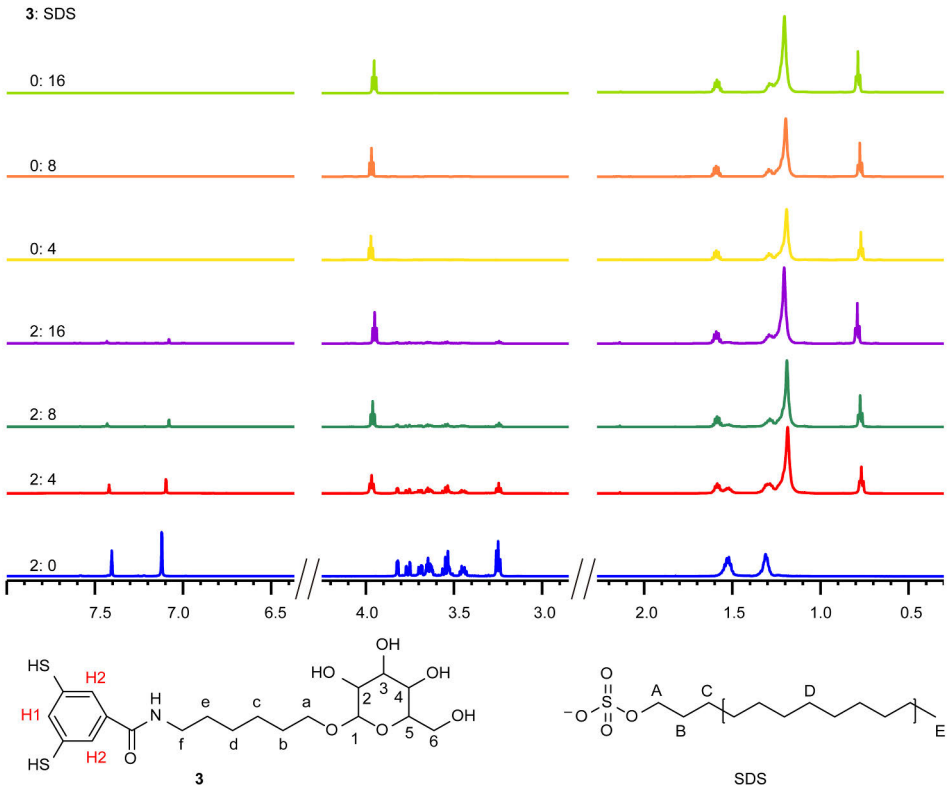

Figure 47. ^{1}H NMR spectra of building block **3** (2 mM) in the presence of increasing concentrations of SDS (4 mM, 8 mM and 16 mM) prior to oxidation. Selected spectral regions are shown for clarity. Upon addition of SDS, concentration-dependent and site-specific chemical shift changes are observed for the aromatic protons of building block **3**, while the resonances of SDS display only minor changes across the same concentration range.

Notably, despite the local, site-specific chemical shift perturbations observed for building block **3**, the overall spectral profiles of the building block **3**–SDS mixtures closely resembled those of SDS alone, suggesting that micellar organization is primarily governed by surfactant concentration and is only weakly perturbed at a global level by the presence of the building block. Accordingly, building block **3** is best described as being incorporated as a guest within a preorganized amphiphilic environment rather than acting as a persistent, structure-directing component of the micelles.

Spatial proximity between building block **3** and SDS was further evaluated by two-dimensional NOESY spectroscopy. At 4 mM SDS, weak NOE cross-peaks were observed between the aromatic region of building block **3** (H1) and the aliphatic protons of SDS (H_D), indicating limited interfacial contact (**Figure 48A**). As the SDS concentration increased to 8 mM and 16 mM, cross-peak intensities grew significantly stronger and comparable, consistent with a transition from weak interfacial association to a more persistent micelle-associated state, reflected by increased spatial proximity to the hydrophobic domains (**Figure 48C–D**).

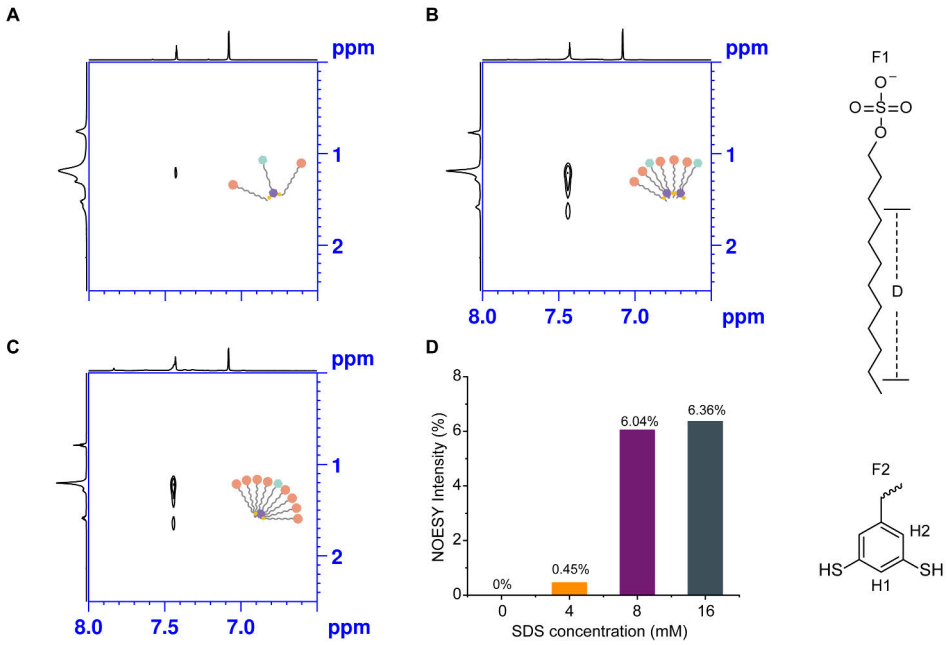

Figure 48. 2D NOESY analysis of the spatial proximity between building block **3** and SDS at increasing surfactant concentrations prior to oxidation. (A–C) Sections of the 2D NOESY spectra highlighting cross-peaks between the aromatic protons of building block **3** (2 mM) and the aliphatic protons of SDS at 4 mM (A), 8 mM (B), and 16 mM (C) SDS. At low SDS concentration, only weak NOE cross-peaks are observed, whereas markedly stronger cross-peaks appear at higher SDS concentrations. (D) Relative NOESY cross-peak intensities as a function of SDS concentration NOE intensities were quantified by normalizing the H1–SDS cross-peak integrals to the diagonal signal of H_2, which does not exhibit detectable NOE cross-peaks under these conditions, allowing comparison of relative spatial proximity across different surfactant concentrations. Chemical structures and proton assignments of SDS (F1) and building block **3** (F2) are shown for reference.

To further assess how micellar environments influence monomer mobility, T_2 relaxation times of selected protons were measured across increasing SDS concentrations. Aromatic protons H_1 and H_2 exhibited marked increases in T_2 upon

SDS addition, rising from 1871 ms and 540 ms in the absence of surfactant to 5349 ms and 1981 ms at 4 mM SDS, and reaching maximum of 6907 ms and 4829 ms at 8 mM SDS, respectively. These changes indicate a redistribution of molecular dynamics upon micellar association, consistent with enhanced motional averaging experienced by the monomer within the amphiphilic environment. In contrast, SDS protons displayed sharp decreases in T_2 values (H_E: 1303 ms to 41.6 ms at 4 mM SDS), reflecting the restricted mobility associated with supramolecular assembly. Partial recovery of SDS relaxation times at higher concentrations likely reflects the coexistence of micelle-bound and free surfactant populations.

Although H1 and H2 of building block **3** occupy different positions on the aromatic core, their dynamic differentiation became more pronounced within micellar environments. At 8-16 mM SDS, only H1 showed NOE correlations with SDS aliphatic protons and a slight T_2 decrease, suggesting closer association with the micellar interior. H2 remained dynamically flexible and solvent accessible. These results indicate that environment-driven partitioning not only modulates global conformational mobility but also amplifies local asymmetry within building block **3**, generating submolecular differentiation that mirrors the topology and density of the micellar scaffold.

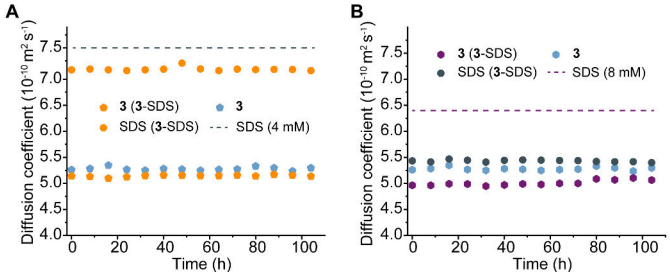

Figure 49. DOSY-derived diffusion coefficients of building block **3** (H2) and SDS (H_A) measured in sealed NMR tubes at 4 mM (A) and 8 mM (B) SDS prior to oxidation. SDS-alone diffusion coefficients were measured once at 0 h and are shown as reference values. Building block **3** exhibits reduced diffusion coefficients in the presence of SDS, approaching those of SDS under micellar conditions.

To assess whether such site-specific dynamic differentiation is reflected at the ensemble level, diffusion coefficients were measured by DOSY spectroscopy. Diffusion coefficients were extracted from the H2 resonance of building block **3** and the H_A resonance of SDS, enabling direct comparison of their diffusion behavior under identical conditions. In the presence of SDS (4 and 8 mM), the diffusion coefficient of building block **3** decreased markedly and approached that of SDS, consistent with co-diffusion of the monomer with micellar assemblies (**Figure 49**). The absence of significant time-dependent changes indicates that, owing to the

limited oxygen availability in sealed NMR tubes, oxidation proceeds sufficiently slowly that the system remains in a quasi-steady state over the measurement window. Together with the NOESY and T_2 data, these results establish that local, environment-imposed asymmetry within the monomer is integrated into a micelle-associated dynamic state at the ensemble scale.

After oxidation, the aromatic and amide resonances of building block **3** became extensively broadened and effectively unobservable in the ^{1}H NMR spectrum, leaving predominantly broadened SDS signals, consistent with the formation of high-molecular-weight assemblies. These results indicate that oxidation within micellar environments promotes the conversion of preorganized, molecular-scale interactions into extended supramolecular assemblies. The morphologies of these assemblies were subsequently examined by cryogenic transmission electron microscopy (cryo-TEM).

3.3.3.6 Topology-dependent emergence of supramolecular chirality

To delineate the evolution of supramolecular assemblies during oxidation, cryo-TEM was employed to examine SDS-only systems as well as mixtures containing building block **3** at both the initial stage (0 h) and after partial oxidation (48 h). This comparison enables the separation of intrinsic SDS aggregation behavior from oxidation-induced assembly processes and provides a consistent baseline for assessing morphology evolution as a function of SDS concentration (**Figure 50**).

SDS-only control samples at all investigated concentrations exhibited a homogeneous, low-contrast background characteristic of SDS aggregation, while at higher SDS concentrations typical spherical micelles were clearly observed, providing a morphological reference for distinguishing SDS aggregates from assemblies driven by building block **3** (**Figure 50B1**–**D1**). UPLC analysis at the initial stage (0 h) shows that all systems are dominated by monomeric species, with no detectable macrocycle formation (**Figure 50A1, top**). In systems containing building block **3** (2 mM), cryo-TEM images recorded at 0 h revealed no well-defined ordered supramolecular structures (**Figure 50A2**). At a **3**:SDS ratio of 2:4 mM, an increased number of nanoscale aggregates was observed (**Figure 50B2**), whereas at 2:8 mM the images were mainly characterized by enhanced contrast with only a small number of short linear features (**Figure 50C2**). At 2:16 mM, similar but even less pronounced features were detected (**Figure 50D2**). These observations indicate that the presence of building block **3** perturbs the SDS aggregates at the initial stage, but the system has not yet evolved into clearly defined ordered assemblies.

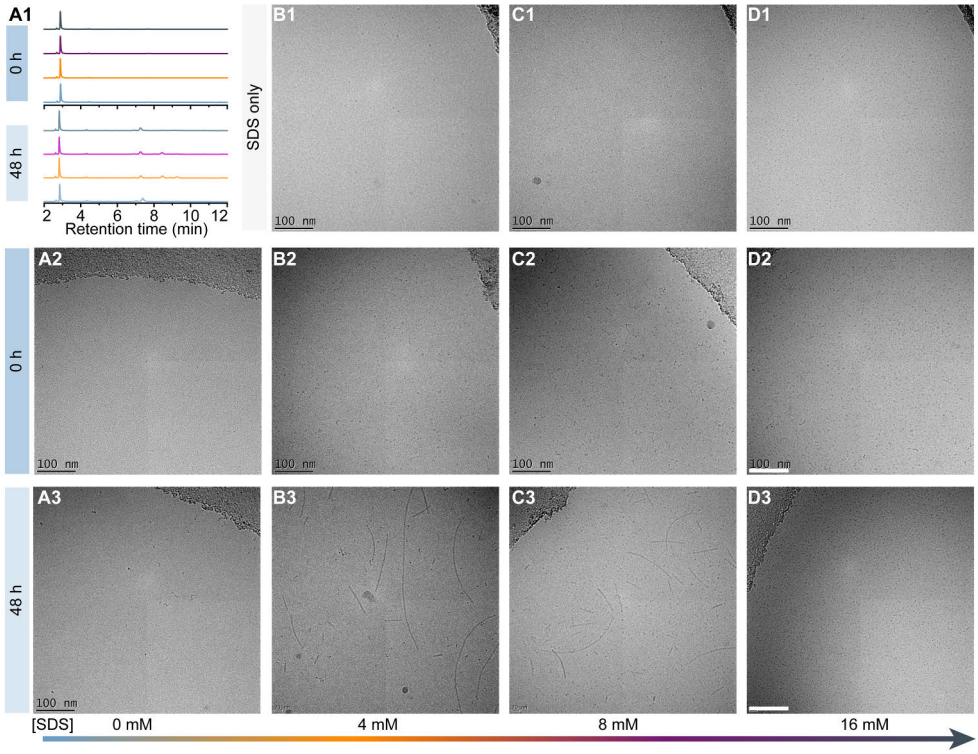

Figure 50. Cryogenic transmission electron microscopy (cryo-TEM) analysis of assembly states during oxidation of building block **3** under different SDS concentrations. Columns correspond to increasing SDS concentration (0, 4, 8, and 16 mM). (A1) shows representative UPLC chromatograms recorded at 0 h and 48 h, confirming partial oxidation over this time window. (B1–D1) show SDS-only control samples, which exhibit homogeneous, low-contrast background features characteristic of SDS aggregation; at higher SDS concentrations, typical spherical micelles are clearly observed. (A2–D2) show samples containing building block **3** (2 mM) at the initial stage of oxidation (0 h). (A3–D3) show the corresponding samples after 48 h of oxidation. Scale bars: 100 nm.

At the early stage of oxidation, assemblies formed after 48 h already begin to exhibit pronounced SDS-concentration-dependent differences. In the absence of SDS, only a small number of irregular wormlike aggregates are observed after 48 h (**Figure 50A3**). Although UPLC analysis shows that all systems remain largely monomeric at this time point (**Figure 50A1, bottom**), distinct assembly behaviors are evident. At a **3**:SDS ratio of 2:4 mM, only small amounts of macrocycles $\mathbf{3}_3$, $\mathbf{3}_5$, and $\mathbf{3}_6$ are detected; however, cryo-TEM reveals the formation of pronounced nanofibers, some of which display a twisted morphology (**Figure 50B3**). This indicates that the system has already entered a fibrillar assembly pathway, despite macrocycles not yet dominating the overall composition. When the SDS concentration is increased to 8 mM (**3**:SDS = 2:8 mM), oxidation for 48 h yields only small amounts of macrocycles $\mathbf{3}_3$ and $\mathbf{3}_5$. Corresponding cryo-TEM images

show the presence of nanofibers without detectable twisted features, while a noticeable background of SDS micelles remains (**Figure 50C3**). In contrast, at higher SDS concentration (**3**:SDS = 2:16 mM), UPLC analysis indicates the formation of only minor amounts of macrocycle $\mathbf{3_3}$ after 48 h. Cryo-TEM images reveal no significant morphological changes compared to the initial state (**Figure 50D3**), with the overall appearance still dominated by a micellar background, indicating that under conditions exceeding the critical micelle concentration, the global morphology of the system remains governed by SDS aggregates.

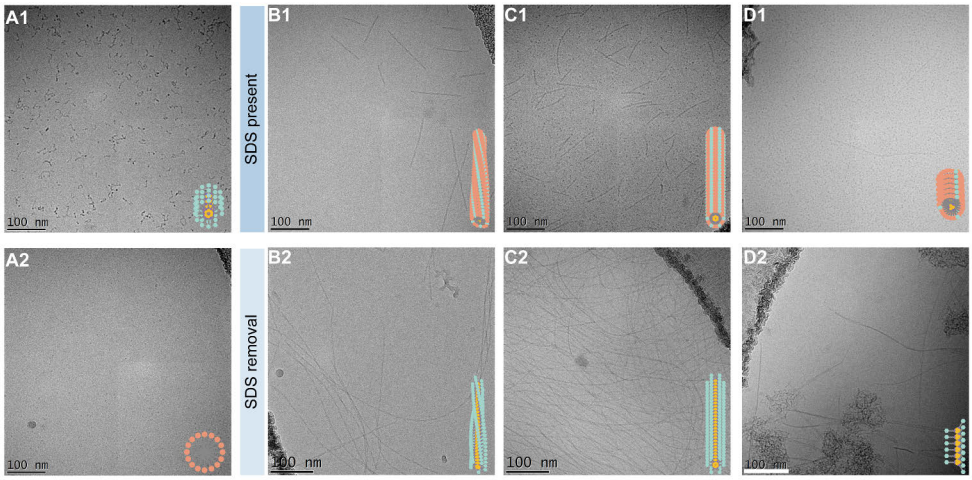

Figure 51. Cryogenic transmission electron microscopy (cryo-TEM) images of supramolecular assemblies formed after complete oxidation of building block **3**. (A1) Oxidation in the absence of SDS, yielding disordered wormlike aggregates formed by uncontrolled oligomerization. (A2) SDS alone (8 mM), displaying spherical micelles. (B1–D1) Assemblies obtained after oxidation in the presence of SDS (2 mM building block **3** with 4, 8, and 16 mM SDS), corresponding predominantly to macrocycles $\mathbf{3_5}$, $\mathbf{3_6}$, and $\mathbf{3_3}$, respectively. (B2–D2) Corresponding samples after complete SDS removal. Twisted nanofibers formed by $\mathbf{3_5}$ persist after SDS removal, whereas samples containing $\mathbf{3_6}$ yield only straight nanofibers, and the spherical micelles observed prior to SDS removal completely disappear. In samples dominated by $\mathbf{3_3}$, SDS micelles disappear upon SDS removal, leaving heterogeneous assemblies composed of nanofibers and aggregated wormlike structures. Scale bars: 100 nm.

After complete oxidation, the supramolecular morphologies formed under different SDS concentrations were examined by cryo-TEM (**Figure 51**). In the absence of SDS, the fully oxidized system predominantly formed disordered wormlike aggregates (**Figure 51A1**), consistent with uncontrolled oligomerization in bulk solution. In contrast, oxidation in the presence of SDS led to the emergence of distinct morphologies that depended strongly on the SDS concentration.

At **3**:SDS ratio of 2:4 mM, complete oxidation resulted in exclusively twisted nanofibers **(Figure 51B1**), consistent with the selective amplification of macrocycle **3_5.** These fibers exhibited uniform helicity with an average pitch of approximately 40 nm. Increasing the SDS concentration to 8 mM (**3**:SDS = 2:8 mM) led to the coexistence of straight nanofibers and residual spherical micelles after full oxidation (**Figure 51C1**), consistent with predominant formation of macrocycle **3_6**. At higher SDS concentration (**3**:SDS = 2:16 mM), spherical micelles persisted throughout oxidation and only sparse, short fibers were observed after full conversion (**Figure 51D1**), in agreement with dominant formation of macrocycle **3_3**.

To assess whether these morphologies were maintained independently of SDS, the assemblies were examined after complete SDS removal (**Figure 51B2–D2**). An SDS-only control subjected to the same removal procedure is shown in **Figure 51A2**, confirming the absence of detectable SDS micelles after removal. Under these conditions, the twisted nanofiber morphology formed by macrocycle **3_5** was fully preserved (**Figure 51B2**), whereas samples dominated by macrocycles **3_6** and **3_3** yielded exclusively straight nanofibers or featureless fibrous and wormlike aggregates after SDS removal (**Figure 51C2–D2**). The disappearance of spherical micelles upon SDS removal confirms that the micellar features observed prior to removal originated from excess SDS rather than macrocycle-driven co-assembly.

Circular dichroism measurements further revealed that pronounced chiroptical activity is observed exclusively for macrocycle **3_5**. The **3_5**-SDS assemblies display a strong bisignate CD signal with negative Cotton effects at 313 and 248 nm, coinciding with the corresponding UV–vis absorption maxima. These spectral features are retained after SDS removal, indicating that the supramolecular chirality originates from the topology of macrocycle **3_5** and persists independently of the surfactant environment.[144] In contrast, macrocycle **3_6** exhibits only weak, non-featured CD signals in the presence of SDS and is nearly CD-silent after SDS removal, whereas oxidized oligomeric assemblies show no detectable CD response under the conditions examined (**Figure 52**). CD measurements were therefore focused on assemblies that exhibit well-defined fibrous morphologies after complete oxidation.

Overall, these results demonstrate that SDS micelles act as transient selectors that bias the oxidation pathway toward distinct macrocycle topologies, but do not dictate the final supramolecular architecture.[146] Instead, the assembled morphologies and their associated chiroptical responses are encoded by the intrinsic topology of the amplified macrocycles. In particular, only macrocycle **3_5** gives rise to stable twisted nanofibers and pronounced supramolecular chirality, which persists after SDS removal, establishing topology as the key determinant for the emergence and retention of supramolecular chirality in this system.

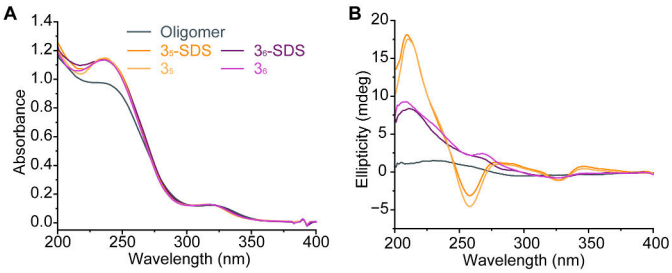

Figure 52. UV–vis and circular dichroism (CD) spectra of macrocycle assemblies before and after SDS removal. (A) UV–vis absorption spectra of oxidized building block **3** (oligomer), **3₅**-SDS (4 mM SDS), **3₆**-SDS (8 mM SDS), and the isolated macrocycles **3₅** and **3₆**. The absorption profiles of **3₅** and **3₆** remain largely unchanged after SDS removal, indicating preservation of the macrocyclic structures. (B) CD spectra of the corresponding samples. **3₅**-SDS exhibits a pronounced Cotton effect that is retained in the isolated **3₅** sample, whereas **3₆**-SDS shows only a weak CD signal and the isolated **3₆** is nearly CD-silent.

3.3.3.7 Computational and environmental rationalization of topology control

To understand how environmental conditions regulate macrocycle topology and supramolecular behavior, atomistic molecular dynamics (MD) simulations were performed to examine the stacking and assembly of **3₃**, **3₅**, and **3₆** at different building block **3**:SDS molar ratios. Each macrocycle was modeled as an axially stacked aggregate and simulated under experimentally relevant surfactant conditions corresponding to selective amplification (building block **3**: SDS = 2:4, 2:8, and 2:16 mM). The resulting assemblies were analyzed in terms of intermacrocycle interactions, macrocycle-SDS contacts, hydrogen bonding, and overall morphology (**Figure 53**).

Macrocycle **3₅** exhibited the strongest intermacrocycle interaction energies together with the highest number of intermacrocycle hydrogen bonds, consistent with its efficient stacking and selective amplification. In contrast, its interaction with SDS was the weakest among the three systems, characterized by few hydrogen bonds and a loose, asymmetric distribution of surfactant molecules around the fiber periphery. This transient and non-restrictive interaction environment coincided with the spontaneous emergence of a twisted stacking configuration. Magnified views further reveal a consistent, handed offset between neighboring macrocycles, indicating that supramolecular chirality originates from the intrinsic local stacking geometry of **3₅** rather than being imposed by SDS. This behavior is in full agreement with the experimentally observed twisted nanofibers, pronounced CD signals, and the persistence of chirality after SDS removal.

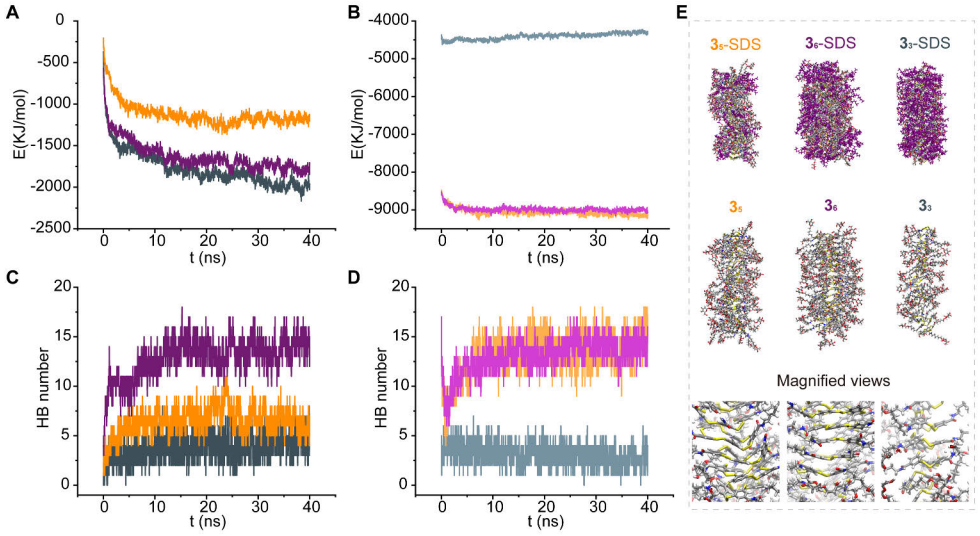

Figure 53. Atomistic MD analysis of macrocycle–SDS ($\mathbf{3_5}$–SDS, $\mathbf{3_6}$–SDS, $\mathbf{3_3}$–SDS) and macrocycle–macrocycle interactions ($\mathbf{3_5}$–$\mathbf{3_5}$, $\mathbf{3_6}$–$\mathbf{3_6}$, $\mathbf{3_3}$–$\mathbf{3_3}$). (A) Time evolution of interaction energies between macrocycles and SDS molecules. (B) Time evolution of interaction energies between macrocycles within the stacked assemblies. (C) Number of hydrogen bonds formed between macrocycles and SDS molecules as a function of simulation time. (D) Number of hydrogen bonds formed between macrocycles within the stacked assemblies. (E) Representative MD snapshots of stacked macrocycle aggregates for $\mathbf{3_5}$, $\mathbf{3_6}$, $\mathbf{3_3}$ under their respective selective amplification conditions. Top row: assemblies in the presence of SDS, illustrating differences in surfactant association. Middle row: corresponding macrocycle stacks after removal of SDS, highlighting intrinsic stacking stability. Bottom row: magnified views highlighting local stacking motifs and symmetry differences.

Macrocycle $\mathbf{3_6}$ showed moderately strong intermacrocycle cohesion but substantially stronger association with SDS. The resulting assemblies form predominantly straight nanofibers, and magnified views reveal no persistent handed offset at the local stacking level. Accordingly, $\mathbf{3_6}$ exhibits only weak chiroptical activity in the presence of SDS and becomes nearly CD-silent after SDS removal, indicating that its assemblies lack an intrinsic chiral stacking motif and rely on the surfactant environment for structural organization. Macrocycle $\mathbf{3_3}$ displayed the weakest intermacrocycle interactions but the strongest binding to SDS, leading to compact and disordered aggregates. The absence of continuous stacking interactions and the dominance of surfactant association are consistent with its micellar morphology and the lack of selective amplification or detectable chiroptical response.

To assess whether this topology-dependent behavior is also reflected at the energetic level, density functional theory (DFT) calculations were performed to evaluate the formation energetics of the competing macrocycles under different environmental conditions. The calculated formation energies of macrocycles $\mathbf{3_3}$, $\mathbf{3_5}$,

and $\mathbf{3_6}$ are summarized in **Table 2**. Gas-phase calculations were first carried out to establish an intrinsic energetic baseline, with formation energies normalized by the number of atoms in each macrocycle to enable comparison among different topologies. Under these conditions, macrocycles $\mathbf{3_5}$ and $\mathbf{3_6}$ exhibit comparable formation energies per atom, whereas macrocycle $\mathbf{3_3}$ is significantly less favorable, indicating that, in the absence of environmental modulation, the intrinsic thermodynamic preference does not strongly discriminate between $\mathbf{3_5}$ and $\mathbf{3_6}$ but disfavors the smaller macrocycle $\mathbf{3_3}$.

Table 2. DFT-calculated formation energies of macrocycles

Macrocycle	n	M	E_{form} (eV/atom) gas phase	E_{form} (eV/atom) dielectric continuum
$\mathbf{3_5}$	5	280	0.00185	0.0115
$\mathbf{3_6}$	6	336	0.00192	0.0131
$\mathbf{3_3}$	3	168	0.00574	0.0102

Note: Gas-phase and dielectric-continuum calculations employ different electronic references. Moreover, different representative dielectric constants were used for different macrocycles. Therefore, absolute E_{form} values are not directly compared across environments; only relative trends within each computational treatment are discussed. Here, n denotes the number of building block **3** units per macrocycle, and M denotes the total number of atoms in the macrocycle.

To probe the influence of environmental polarity, additional calculations were performed using a dielectric-continuum model. Representative dielectric constants were selected to approximate solution environments at different SDS concentrations. Within this framework, the relative stability ranking among macrocycles is altered compared to the gas-phase reference, and the formation energies fall within a comparable energetic range, indicating that changes in environmental polarity can qualitatively reshape the formation-energy landscape. Representative DFT-optimized molecular structures obtained under the corresponding dielectric-continuum conditions are shown in **Figure 54**.

Because gas-phase and dielectric-continuum calculations employ different electronic reference states, and because different representative dielectric constants were used for different macrocycles, absolute formation energies are not directly compared across environments. Instead, these DFT results provide a qualitative energetic rationale for the experimentally observed, SDS-dependent topology selection, complementing the MD analysis and supporting the conclusion that macrocycle topology and supramolecular behavior are jointly regulated by intrinsic stacking propensity and environmental modulation.

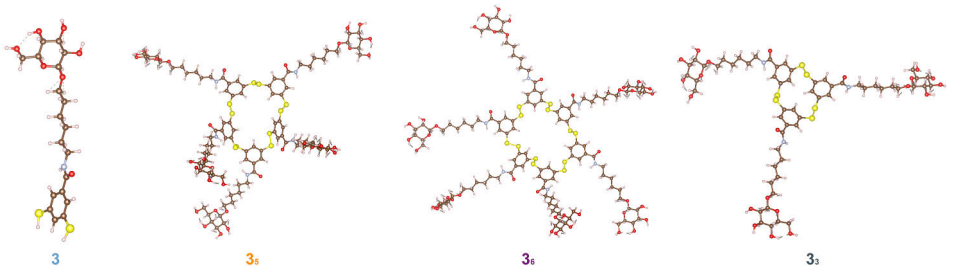

Figure 54. DFT-optimized molecular structures of building block **3** and macrocycles $\mathbf{3_5}$, $\mathbf{3_6}$, and $\mathbf{3_3}$. The macrocycle structures shown correspond to representative optimized geometries obtained under dielectric-continuum conditions used in the DFT calculations.

3.3.3.8 Structural and environmental programming of topology and function

To determine whether topology control is specific to SDS or reflects a more general micellar phenomenon, a series of structurally related anionic and cationic surfactants were examined. Sodium dodecyl sulfonate (DSS), an anionic analogue of SDS, caused extensive peak broadening at 2:2 mM, indicative of non-selective oligomerization, but selectively directed the formation of $\mathbf{3_5}$ at 2:4 and 2:8 mM (**Figure 55A**). While DSS reproduces the low-concentration selectivity observed for SDS, it does not induce the topology switch to $\mathbf{3_6}$ at higher surfactant concentration, indicating that subtle differences in headgroup chemistry can significantly influence the programmability of topology selection. Similarly, investigating surfactants with different alkyl chain length, such as sodium decyl sulfate (SDS-10) and sodium tetradecyl sulfate (SDS-14), revealed that they also failed to induce the desired topology switching, highlighting the unique role of the dodecyl chain in this system. Among cationic surfactants, dodecyltrimethylammonium bromide (DTAB, C_{12}) exclusively generated $\mathbf{3_5}$ across all concentrations tested, indicating strong but narrow selectivity (**Figure 55B**). In contrast, hexadecyltrimethylammonium bromide (CTAB, C_{16}) produced $\mathbf{3_5}$ only at low concentration (2:2 mM) and predominantly yielded macrocycle $\mathbf{3_3}$ at 2:4 and 2:8 mM (**Figure 55D**), suggesting that excessive micellar size or reduced compatibility favors the formation of low-order, non-functional species.

Strikingly, tetradecyltrimethylammonium bromide (TTAB, C_{14}) was the only cationic surfactant capable of reproducing SDS-like behavior. Macrocycle $\mathbf{3_5}$ formed at 2:2 mM, a mixture of $\mathbf{3_5}$ and $\mathbf{3_6}$ appeared at 2:4 mM, and $\mathbf{3_6}$ dominated at 2:8 mM (**Figure 55C**). Notably, the critical micelle concentration of TTAB lies in a concentration range comparable to that of SDS, such that the experimental conditions span the micellization threshold, providing a physical basis for the observed concentration-dependent topology switching. This programmable

transition between distinct topologies highlights TTAB's ability to provide a responsive micellar microenvironment and identifies it as a rare non-anionic micellar template capable of dual topology control. The contrasting behaviors of DTAB, TTAB, and CTAB further demonstrate that topology selection is not dictated solely by surfactant charge, but instead depends critically on the balance among micellar dimensions, curvature, and molecular compatibility with the building block.

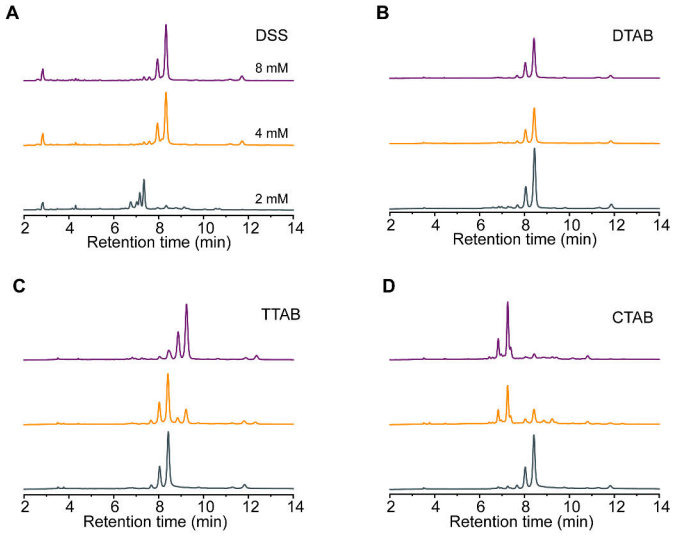

Figure 55. Surfactant-dependent macrocycle topology selection from building block **3**. UPLC traces of oxidized dynamic combinatorial libraries derived from building block 3 in the presence of different surfactants at varying concentrations. (A) Sodium dodecyl sulfonate (DSS), (B) dodecyltrimethylammonium bromide (DTAB), (C) tetradecyltrimethylammonium bromide (TTAB), and (D) hexadecyltrimethylammonium bromide (CTAB). For each panel, traces are shown at surfactant concentrations of 2 mM (bottom), 4 mM (middle), and 8 mM (top). Distinct and surfactant-dependent macrocycle selectivity is observed, highlighting the role of micellar identity and concentration in programming macrocycle topology.

To examine the robustness of this environmental programming, the effect of increased ionic strength was investigated by introducing 100 mM NaCl into SDS-templated systems derived from building block **3** (**Figure 56A**). At a building block **3**:SDS ratio of 2:4 mM, the system changed from producing exclusively macrocycle $\mathbf{3_5}$ to a mixture of $\mathbf{3_5}$ and $\mathbf{3_6}$. At 2:8 mM, which typically favors formation of $\mathbf{3_6}$ under standard conditions, elevated ionic strength unexpectedly promoted $\mathbf{3_5}$ as the dominant species. These results indicate that increased ionic strength perturbs the micellar interface, likely through electrostatic screening and altered surfactant packing, thereby reshaping the energetic landscape governing topology selection.

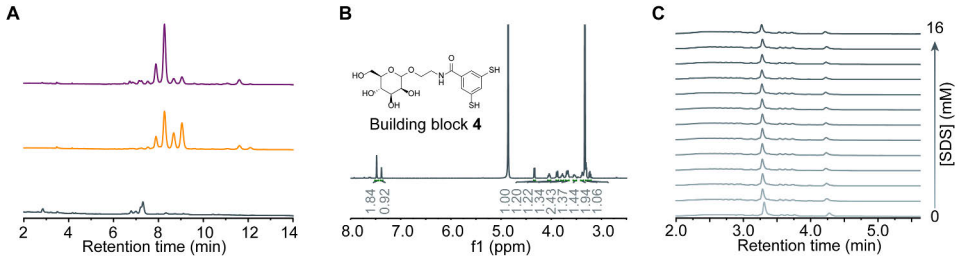

Figure 56. Macrocycle selectivity under increased ionic strength and reduced building-block hydrophobicity. (A) Oxidation of building block **3** in the presence of 100 mM NaCl. At a building block **3**:SDS ratio of 2:4 mM, a mixture of macrocycles $\mathbf{3_5}$ and $\mathbf{3_6}$ is formed, whereas at 2:8 mM selective amplification of macrocycle $\mathbf{3_5}$ is observed. (B) ^{1}H NMR spectrum of building block **4** (500 MHz, MeOD-d_4), an analogue of building block **3** in which the C6 alkyl spacer is shortened to C2. (C) Oxidation of building block **4** in the presence of varying SDS concentrations yields mixtures of macrocycles $\mathbf{4_3}$ and $\mathbf{4_4}$ without selective amplification, indicating the absence of effective template-directed control.

To further define the molecular boundaries of environmental programming, a structural analogue, building block **4** (**Figure 56B**), was synthesized in which the hydrophobic spacer of building block **3** was shortened from six to two carbon atoms. Upon oxidation in the presence of SDS, building block **4** failed to generate pentameric or hexameric macrocycles and instead yielded only trimeric and tetrameric species (**Figure 56C**). The concentration-independent macrocycle distribution across different SDS concentrations underscores the critical role of amphiphilic cooperativity in enabling environmental programmability and demonstrates that insufficient hydrophobic character prevents effective, SDS-directed topology selection.

Together, these results establish that macrocycle topology and emergent supramolecular function are programmed by a cooperative interplay between micellar environment and building-block amphiphilicity, with both factors defining the accessible and inaccessible regions of the topology selection landscape.

3.3.4 Summary

In summary, this section investigates how transient micellar environments direct the evolution of dynamic networks based on the mannose-functionalized building block **3**. Systematic variation of SDS concentration controls macrocycle topology, leading to the selective emergence of distinct species $\mathbf{3_5}$, $\mathbf{3_6}$, and $\mathbf{3_3}$. Among them, $\mathbf{3_5}$ exhibited autocatalytic self-replication, persistent supramolecular chirality, and structural stability after micelle removal, identifying it as a topology-encoded self-sustaining replicator.

NMR spectroscopy and relaxation analyses reveal that SDS concentration regulates the dynamic state and spatial partitioning of the monomer prior to oxidation, thereby biasing subsequent topology selection. Complementary molecular dynamics and density functional theory calculations indicate that surfactant concentration shapes both the supramolecular and thermodynamic energy landscapes governing macrocycle formation. Perturbations in ionic strength and surfactant identity further demonstrate that macrocycle topology is not an intrinsic property of the building block alone but a programmable outcome arising from molecular compatibility, micellar curvature, and interfacial organization.

Together, these findings demonstrate that transient amphiphilic environments can function as active templates that direct topology selection, self-assembly, and emergent function within oxidation-driven dynamic networks. More specifically, the results show that SDS concentration governs the relative formation of different macrocyclic topologies during oxidation, supporting a role for micellar templation in topology selection and amplification. In the case of $\mathbf{3}_5$, the persistence of supramolecular chirality and structural organization after micelle removal further indicates that part of this environmentally induced bias can remain evident beyond the immediate templating state. The interplay between reversible covalent exchange and micellar organization therefore provides a mechanistic framework for understanding how environmental structure can be translated into persistent molecular effects in synthetic, and potentially prebiotic, dynamic systems.

4 Summary

In this thesis, a series of amphiphilic compounds were employed as operative templates to drive the emergence of complex functional behaviors within dynamic covalent libraries of disulfide macrocycles. By integrating template effects, oxidation-driven exchange, and supramolecular organization, three successive systems were established to reveal how amphiphilic templation governs molecular selection, amplification, and information retention in aqueous environments. Together, these studies demonstrate the versatility of dynamic combinatorial chemistry (DCC) as a platform for constructing adaptive and functionally responsive molecular networks.

In the first part, oxidation-driven dynamic molecular networks were constructed in living cells, where a short-chain tetraphenylethene-based quaternary ammonium amphiphile served simultaneously as a structural template and a fluorescent reporter. The resulting assemblies displayed reversible fluorescence modulation under oxidative conditions, showing that redox-controlled disulfide exchange can operate autonomously in complex biological environments. This work established the feasibility of implementing dynamic covalent chemistry in living systems and laid the foundation for responsive molecular imaging based on reversible network behavior.

In the second part, a long-chain aggregation-induced emission amphiphile was introduced to preorganize disulfide macrocycles, enhancing hydrophobic interactions and reducing entropic barriers. This preorganization led to the selective amplification of an octameric species and enabled functional coupling with the chemotherapeutic drug doxorubicin. The resulting assemblies provided real-time optical monitoring of drug release through fluorescence modulation, linking molecular preorganization to entropy-driven amplification and therapeutic function.

In the third part, sodium dodecyl sulfate (SDS) micelles acted as transient amphiphilic compartments that directed the composition of dynamic disulfide libraries. By tuning micellar concentration, pentameric, hexameric, and trimeric macrocycles were selectively amplified. Importantly, the pentameric species displayed topology-encoded persistence, retaining supramolecular chirality and replication behavior even after removal of the micellar environment, whereas the

hexameric species is more appropriately interpreted as a micelle-stabilized product whose amplification depends on continued environmental support. This distinction shows that amphiphilic environments can either transiently stabilize selected outcomes or, under favorable topological conditions, imprint chiral information and replicative states that persist beyond the template itself.

Overall, this work establishes amphiphilic templation as a general and versatile strategy for controlling molecular behavior in dynamic disulfide libraries. Across the three systems, the influence of amphiphiles evolves from guiding reversible organization to promoting selective amplification, and finally to supporting persistent, topology-dependent behavior under transient environmental control. By connecting structure, dynamics, and function within aqueous media, the thesis provides design principles for adaptive chemical systems that emulate key features of biological organization and evolution.

Acknowledgements

This thesis is based on experimental work carried out at the MediCity Research Laboratory and the Laboratory of Organic Chemistry and Chemical Biology, Department of Chemistry, University of Turku, Finland. Financial support from the China Scholarship Council, the Sigrid Jusélius Foundation (Senior Researcher Fellowship), and the Academy of Finland is gratefully acknowledged. I also acknowledge the Doctoral Programme in Exact Sciences (EXACTUS) of the University of Turku Graduate School (UTUGS) for providing me with the opportunity to pursue my doctoral studies.

First and foremost, I would like to express my sincere gratitude to my supervisor, Dr. Jianwei Li, for giving me the opportunity to pursue my doctoral studies under his guidance. I am deeply grateful for his continuous support, insightful advice, patience, and trust throughout my PhD studies. His expertise in dynamic combinatorial chemistry and his rigorous approach to scientific research have been invaluable to my academic and professional development. I am also grateful to my co-supervisor, Professor Tuomas Lönnberg, for his support during my doctoral studies. In addition, I thank my research director, Professor Pasi Virta, for his continued support.

I would like to express my sincere gratitude to Professor Hao Li and Emeritus Professor Heikki Tenhu for carefully reviewing my thesis. Their valuable comments and suggestions greatly improved this thesis. I am also grateful to Professor Kari Rissanen for agreeing to serve as my opponent.

I would also like to thank my colleagues for their constant support. My gratitude goes to all present and former co-workers at the MediCity Research Laboratory for fostering a balanced, collegial, and positive working environment. In particular, I thank Dr. Yu Cao, Dr. Yonglei Lyu, Dr. Dawei Qi, Dr. Xiaoxia Wu, Dr. Jingjing Yu, Xuncheng Shi, Dr. Qin Li, Caihong Lin, and Chong Chen for their help, advice, and for creating a pleasant atmosphere in the laboratory. I am especially grateful to Katri Kulmala for her invaluable support at all times, and to Dr. Antti-Pekka Laine for his extensive assistance with IT-related matters. I further thank Annika Kankare, Pasi Viljakainen, Mikael Wasberg, and Kim Sundfors for their support with chemicals and instrument maintenance. I warmly thank Dr. Sanna Nordman and Dr. Eevi

Savola for their administrative support and guidance throughout my doctoral studies, particularly in matters related to the doctoral programme. I also thank all current and former members of the Bioorganic Group for their support and for maintaining a collegial working environment during my first year.

In addition, I thank Dr. Anastassios C. Papageorgiou for PXRD measurements and for his support in numerous trials of sugar and protein crystallization, Dr. Markus Peurla for TEM imaging, Dr. Ermei Mäkilä for SEM imaging, and Dr. Jouko Sandholm for CLSM measurements. I also thank Dr. Tuomas Karskela, Dr. Jari Sinkkonen, Dr. Jani Rahkila, Dr. Denys Mavrynsky, Ilia Evstafev, and Adjunct Professor Alex Dickens at the Instrument Center/CCMA for their assistance with NMR and MS instrumentation. Finally, I thank Dr. Jani Seitsonen (Aalto University) for assistance with cryo-EM, Dr. Emil Rosqvist (Åbo Akademi University) for help with AFM measurements, and Dr. Rebecca Sternke-Hoffmann (Paul Scherrer Institute, PSI) for her professional support and technical assistance with SAXS measurements.

I am happy to have good friends in Turku, Dr. Kang Chen, Dr. Chang Liu, and Dr. Weihua Zhang, whose friendship has brought genuine joy and balance to my time here. I also warmly thank all my friends in Turku for helping me step outside of work, recharge, and keep perspective during demanding periods.

My warmest thanks go to my wife, Xin Wang, for her love and steadfast companionship, which has carried us from our university days to the present. Throughout the years, we have supported one another through challenges and milestones alike, worked side by side in the laboratory, and shared countless conversations about experiments and about life. Her patience, understanding, and unwavering support have been a constant source of strength, and I am deeply grateful to have shared this journey with her.

Finally, I thank my parents, Deming Yang and Huifang Wei, and my elder brother, Xing Yang, for their enduring encouragement, trust, and support.

Turku, March 2026
Jinghui Yang
杨敬辉

List of References

[1] Lehn, J. M. Supramolecular chemistry: receptors, catalysts, and carriers. *Science* **1985**, *227* (4689), 849-856. DOI: 10.1126/science.227.4689.849.

[2] Whitesides, G. M.; Grzybowski, B. Self-assembly at all scales. *Science* **2002**, *295* (5564), 2418-2421. DOI: 10.1126/science.1070821.

[3] Lehn, J. M. Dynamic combinatorial chemistry and virtual combinatorial libraries. *Chem. Eur. J.* **1999**, *5* (9), 2455-2463. DOI: 10.1002/(sici)1521-3765(19990903)5:9<2455::Aid-chem2455>3.0.Co;2-h.

[4] Lehn, J. M. From supramolecular chemistry towards constitutional dynamic chemistry and adaptive chemistry. *Chem. Soc. Rev.* **2007**, *36* (2), 151-160. DOI: 10.1039/b616752g.

[5] Brady, P. A.; Bonar-Law, R. P.; Rowan, S. J.; Suckling, C. J.; Sanders, J. K. M. 'Living' macrolactonisation: thermodynamically-controlled cyclisation and interconversion of oligocholates. *Chem. Commun.* **1996**, (3), 319-320. DOI: 10.1039/cc9960000319.

[6] Rowan, S. J.; Hamilton, D. G.; Brady, P. A.; Sanders, J. K. M. Automated Recognition, Sorting, and Covalent Self-Assembly by Predisposed Building blocks in a Mixture. *J. Am. Chem. Soc.* **1997**, *119* (10), 2578-2579. DOI: 10.1021/ja963320k.

[7] Otto, S.; Furlan, R. L. E.; Sanders, J. K. M. Dynamic combinatorial libraries of macrocyclic disulfides in water. *J. Am. Chem. Soc.* **2000**, *122* (48), 12063-12064. DOI: DOI 10.1021/ja005507o.

[8] Corbett, P. T.; Leclaire, J.; Vial, L.; West, K. R.; Wietor, J. L.; Sanders, J. K.; Otto, S. Dynamic combinatorial chemistry. *Chem. Rev.* **2006**, *106* (9), 3652-3711. DOI: 10.1021/cr020452p.

[9] Carnall, J. M.; Waudby, C. A.; Belenguer, A. M.; Stuart, M. C.; Peyralans, J. J.; Otto, S. Mechanosensitive self-replication driven by self-organization. *Science* **2010**, *327* (5972), 1502-1506. DOI: 10.1126/science.1182767.

[10] Mattia, E.; Otto, S. Supramolecular systems chemistry. *Nat. Nanotechnol.* **2015**, *10* (2), 111-119. DOI: 10.1038/nnano.2014.337.

[11] Grzybowski, B. A.; Huck, W. T. The nanotechnology of life-inspired systems. *Nat. Nanotechnol.* **2016**, *11* (7), 585-592. DOI: 10.1038/nnano.2016.116.

[12] Grzybowski, B. A.; Fitzner, K.; Paczesny, J.; Granick, S. From dynamic self-assembly to networked chemical systems. *Chem. Soc. Rev.* **2017**, *46* (18), 5647-5678. DOI: 10.1039/c7cs00089h.

[13] Otto, S. Dynamic molecular networks: from synthetic receptors to self-replicators. *Acc. Chem. Res.* **2012**, *45* (12), 2200-2210. DOI: 10.1021/ar200246j.

[14] Li, J.; Nowak, P.; Otto, S. Dynamic combinatorial libraries: from exploring molecular recognition to systems chemistry. *J. Am. Chem. Soc.* **2013**, *135* (25), 9222-9239. DOI: 10.1021/ja402586c.

[15] Sadownik, J. W.; Philp, D. A simple synthetic replicator amplifies itself from a dynamic reagent pool. *Angew. Chem. Int. Ed.* **2008**, *47* (51), 9965-9970. DOI: 10.1002/anie.200804223.

[16] Sorrenti, A.; Leira-Iglesias, J.; Markvoort, A. J.; de Greef, T. F. A.; Hermans, T. M. Non-equilibrium supramolecular polymerization. *Chem. Soc. Rev.* **2017**, *46* (18), 5476-5490. DOI: 10.1039/c7cs00121e.

[17] Giuseppone, N.; Lehn, J. M. Protonic and temperature modulation of constituent expression by component selection in a dynamic combinatorial library of imines. *Chem. Eur. J.* **2006**, *12* (6), 1715-1722. DOI: 10.1002/chem.200501038.

[18] Mansfeld, F. M.; Au-Yeung, H. Y.; Sanders, J. K. M.; Otto, S. Dynamic combinatorial chemistry at the phospholipid bilayer interface. *J. Syst. Chem.* **2010**, *1* (1), 12. DOI: 10.1186/1759-2208-1-12.

[19] Rodriguez-Docampo, Z.; Eugenieva-Ilieva, E.; Reyheller, C.; Belenguer, A. M.; Kubik, S.; Otto, S. Dynamic combinatorial development of a neutral synthetic receptor that binds sulfate with nanomolar affinity in aqueous solution. *Chem. Commun.* **2011**, *47* (35), 9798-9800. DOI: 10.1039/c1cc13451e.

[20] Bull, S. D.; Davidson, M. G.; van den Elsen, J. M.; Fossey, J. S.; Jenkins, A. T.; Jiang, Y. B.; Kubo, Y.; Marken, F.; Sakurai, K.; Zhao, J.; et al. Exploiting the reversible covalent bonding of boronic acids: recognition, sensing, and assembly. *Acc. Chem. Res.* **2013**, *46* (2), 312-326. DOI: 10.1021/ar300130w.

[21] Jin, Y.; Yu, C.; Denman, R. J.; Zhang, W. Recent advances in dynamic covalent chemistry. *Chem. Soc. Rev.* **2013**, *42* (16), 6634-6654. DOI: 10.1039/c3cs60044k.

[22] Dirksen, A.; Dirksen, S.; Hackeng, T. M.; Dawson, P. E. Nucleophilic catalysis of hydrazone formation and transimination: implications for dynamic covalent chemistry. *J. Am. Chem. Soc.* **2006**, *128* (49), 15602-15603. DOI: 10.1021/ja067189k.

[23] Li, J.; Carnall, J. M.; Stuart, M. C.; Otto, S. Hydrogel formation upon photoinduced covalent capture of macrocycle stacks from dynamic combinatorial libraries. *Angew. Chem. Int. Ed.* **2011**, *50* (36), 8384-8386. DOI: 10.1002/anie.201103297.

[24] Lee, H.; Kim, J.; Lee, M.; Kang, J. Dynamic Bond Chemistry in Soft Materials: Bridging Adaptability and Mechanical Robustness. *Chem. Rev.* **2025**, *125* (23), 11379-11425. DOI: 10.1021/acs.chemrev.5c00566.

[25] Greenlee, A. J.; Wendell, C. I.; Cencer, M. M.; Laffoon, S. D.; Moore, J. S. Kinetic and thermodynamic control in dynamic covalent synthesis. *Trends Chem.* **2020**, *2* (12), 1043-1051.

[26] De Greef, T. F.; Smulders, M. M.; Wolffs, M.; Schenning, A. P.; Sijbesma, R. P.; Meijer, E. W. Supramolecular polymerization. *Chem. Rev.* **2009**, *109* (11), 5687-5754. DOI: 10.1021/cr900181u.

[27] Minton, A. P. How can biochemical reactions within cells differ from those in test tubes? *J. Cell Sci.* **2006**, *119* (Pt 14), 2863-2869. DOI: 10.1242/jcs.03063.

[28] Mei, J.; Leung, N. L.; Kwok, R. T.; Lam, J. W.; Tang, B. Z. Aggregation-Induced Emission: Together We Shine, United We Soar! *Chem. Rev.* **2015**, *115* (21), 11718-11940. DOI: 10.1021/acs.chemrev.5b00263.

[29] Feng, H. T.; Yuan, Y. X.; Xiong, J. B.; Zheng, Y. S.; Tang, B. Z. Macrocycles and cages based on tetraphenylethylene with aggregation-induced emission effect. *Chem. Soc. Rev.* **2018**, *47* (19), 7452-7476. DOI: 10.1039/c8cs00444g.

[30] Bartolec, B.; Leonetti, G.; Li, J.; Smit, W.; Altay, M.; Monreal Santiago, G.; Yan, Y.; Otto, S. Emergence of Compartments Formed from Unconventional Surfactants in Dynamic Combinatorial Libraries. *Langmuir* **2019**, *35* (17), 5787-5792. DOI: 10.1021/acs.langmuir.8b03662.

[31] Otto, S.; Furlan, R. L.; Sanders, J. K. Dynamic combinatorial chemistry. *Drug Discov. Today* **2002**, *7* (2), 117-125. DOI: 10.1016/s1359-6446(01)02086-4.

[32] Otto, S.; Furlan, R. L. E.; Sanders, J. K. M. Selection and Amplification of Hosts From Dynamic Combinatorial Libraries of Macrocyclic Disulfides. *Science* **2002**, *297* (5581), 590-593. DOI: doi:10.1126/science.1072361.

[33] Rowan, S. J.; Cantrill, S. J.; Cousins, G. R.; Sanders, J. K.; Stoddart, J. F. Dynamic covalent chemistry. *Angew. Chem. Int. Ed.* **2002**, *41* (6), 898-952. DOI: 10.1002/1521-3773(20020315)41:6<898::aid-anie898>3.0.co;2-e.

[34] West, K. R.; Bake, K. D.; Otto, S. Dynamic combinatorial libraries of disulfide cages in water. *Org. Lett.* **2005**, *7* (13), 2615-2618. DOI: 10.1021/ol0507524.
[35] Corbett, P. T.; Sanders, J. K.; Otto, S. Competition between receptors in dynamic combinatorial libraries: amplification of the fittest? *J. Am. Chem. Soc.* **2005**, *127* (26), 9390-9392. DOI: 10.1021/ja0509026.
[36] Corbett, P. T.; Sanders, J. K.; Otto, S. Exploring the relation between amplification and binding in dynamic combinatorial libraries of macrocyclic synthetic receptors in water. *Chem. Eur. J.* **2008**, *14* (7), 2153-2166. DOI: 10.1002/chem.200701413.
[37] Alfonso, I.; Bolte, M.; Bru, M.; Burguete, M. I.; Luis, S. V.; Rubio, J. Supramolecular control for the modular synthesis of pseudopeptidic macrocycles through an anion-templated reaction. *J. Am. Chem. Soc.* **2008**, *130* (19), 6137-6144. DOI: 10.1021/ja710132c.
[38] Canal-Martin, A.; Perez-Fernandez, R. Protein-Directed Dynamic Combinatorial Chemistry: An Efficient Strategy in Drug Design. *ACS Omega* **2020**, *5* (41), 26307-26315. DOI: 10.1021/acsomega.0c03800.
[39] Bravin, C.; Hunter, C. A. Template effects of vesicles in dynamic covalent chemistry. *Chem. Sci.* **2020**, *11* (34), 9122-9125. DOI: 10.1039/d0sc03185b.
[40] Carbajo, D.; Perez, Y.; Bujons, J.; Alfonso, I. Live-Cell-Templated Dynamic Combinatorial Chemistry. *Angew. Chem. Int. Ed.* **2020**, *59* (39), 17202-17206. DOI: 10.1002/anie.202004745.
[41] Kriebisch, C. M. E.; Burger, L.; Zozulia, O.; Stasi, M.; Floroni, A.; Braun, D.; Gerland, U.; Boekhoven, J. Template-based copying in chemically fuelled dynamic combinatorial libraries. *Nat. Chem.* **2024**, *16* (8), 1240-1249. DOI: 10.1038/s41557-024-01570-5.
[42] Leclaire, J.; Husson, G.; Devaux, N.; Delorme, V.; Charles, L.; Ziarelli, F.; Desbois, P.; Chaumonnot, A.; Jacquin, M.; Fotiadu, F.; et al. CO2 binding by dynamic combinatorial chemistry: an environmental selection. *J. Am. Chem. Soc.* **2010**, *132* (10), 3582-3593. DOI: 10.1021/ja909975q.
[43] Dumartin, M.; Septavaux, J.; Donnier-Marechal, M.; Jeamet, E.; Dumont, E.; Perret, F.; Vial, L.; Leclaire, J. The dark side of disulfide-based dynamic combinatorial chemistry. *Chem. Sci.* **2020**, *11* (31), 8151-8156. DOI: 10.1039/d0sc02399j.
[44] Cacciapaglia, R.; Di Stefano, S.; Mandolini, L. Metathesis reaction of formaldehyde acetals: an easy entry into the dynamic covalent chemistry of cyclophane formation. *J. Am. Chem. Soc.* **2005**, *127* (39), 13666-13671. DOI: 10.1021/ja054362o.
[45] Kosikova, T.; Philp, D. Exploring the emergence of complexity using synthetic replicators. *Chem. Soc. Rev.* **2017**, *46* (23), 7274-7305. DOI: 10.1039/c7cs00123a.
[46] Ratjen, L.; Vantomme, G.; Lehn, J. M. Strain-Induced Reactivity in the Dynamic Covalent Chemistry of Macrocyclic Imines. *Chem. Eur. J.* **2015**, *21* (28), 10070-10081. DOI: 10.1002/chem.201501192.
[47] Larsen, D.; Beeren, S. R. Enzyme-mediated dynamic combinatorial chemistry allows out-of-equilibrium template-directed synthesis of macrocyclic oligosaccharides. *Chem. Sci.* **2019**, *10* (43), 9981-9987. DOI: 10.1039/c9sc03983j.
[48] Samuelsen, L.; Larsen, D.; Schonbeck, C.; Beeren, S. R. pH-Responsive templates modulate the dynamic enzymatic synthesis of cyclodextrins. *Chem. Commun.* **2022**, *58* (33), 5152-5155. DOI: 10.1039/d1cc06554h.
[49] Tong, K. L.; Yee, C. C.; Tse, Y. C.; Au-Yeung, H. Y. Discoveries from a phenanthroline-based dynamic combinatorial library: catenane from a copper(I) or copper(II) template? *Inorg. Chem. Front.* **2016**, *3* (3), 348-353. DOI: 10.1039/c5qi00227c.
[50] Gregolinski, J.; Slepokura, K.; Packowski, T.; Lisowski, J. Expansion of a 2 + 2 macrocycle into a 6 + 6 macrocycle: template effect of cadmium(II). *Org. Lett.* **2014**, *16* (17), 4372-4375. DOI: 10.1021/ol501602f.
[51] Bru, M.; Alfonso, I.; Bolte, M.; Burguete, M. I.; Luis, S. V. Structurally disfavoured pseudopeptidic macrocycles through anion templation. *Chem. Commun.* **2011**, *47* (1), 283-285. DOI: 10.1039/c0cc01784a.

[52] Ulatowski, F.; Sadowska-Kuziola, A.; Jurczak, J. "Choose-a-size" approach in dynamic combinatorial chemistry: a single substrate dynamic combinatorial library of oligomacrocycles that adapts to the size and shape of carboxylates. *J. Org. Chem.* **2014**, *79* (20), 9762-9770. DOI: 10.1021/jo501956h.

[53] Galan, A.; Escudero-Adan, E. C.; Ballester, P. Template-directed self-assembly of dynamic covalent capsules with polar interiors. *Chem. Sci.* **2017**, *8* (11), 7746-7750. DOI: 10.1039/c7sc03731g.

[54] Fuchs, B.; Nelson, A.; Star, A.; Stoddart, J. F.; Vidal, S. Amplification of dynamic chiral crown ether complexes during cyclic acetal formation. *Angew. Chem. Int. Ed.* **2003**, *42* (35), 4220-4224. DOI: 10.1002/anie.200351558.

[55] Vial, L.; Ludlow, R. F.; Leclaire, J.; Perez-Fernandez, R.; Otto, S. Controlling the biological effects of spermine using a synthetic receptor. *J. Am. Chem. Soc.* **2006**, *128* (31), 10253-10257. DOI: 10.1021/ja062536b.

[56] Nowak, P.; Colomb-Delsuc, M.; Otto, S.; Li, J. Template-Triggered Emergence of a Self-Replicator from a Dynamic Combinatorial Library. *J. Am. Chem. Soc.* **2015**, *137* (34), 10965-10969. DOI: 10.1021/jacs.5b04380.

[57] Hamieh, S.; Saggiomo, V.; Nowak, P.; Mattia, E.; Ludlow, R. F.; Otto, S. A "dial-a-receptor" dynamic combinatorial library. *Angew. Chem. Int. Ed.* **2013**, *52* (47), 12368-12372. DOI: 10.1002/anie.201305744.

[58] Ramstrom, O.; Lehn, J. M. In situ generation and screening of a dynamic combinatorial carbohydrate library against concanavalin A. *Chembiochem* **2000**, *1* (1), 41-48. DOI: 10.1002/1439-7633(20000703)1:1<41::AID-CBIC41>3.0.CO;2-L.

[59] Demontrond, F.; Pascal, Y.; Donnier-Marechal, M.; Raillon, C.; Luton, B.; Tramblais, C.; Vial, L.; Gueyrard, D.; Galia, W.; Berger, E.; et al. Dynamic Combinatorial Chemistry Generates Adaptative Libraries of Glyco-Dyn[n]Arenes That can Be Templated to Produce Anti-Adhesive Glycoconjugates Targeting Pseudomonas aeruginosa. *Chem. Eur. J.* **2025**, *31* (48), e02161. DOI: 10.1002/chem.202502161.

[60] Erichsen, A.; Peters, G. H. J.; Beeren, S. R. Templated Enzymatic Synthesis of delta-Cyclodextrin. *J. Am. Chem. Soc.* **2023**, *145* (8), 4882-4891. DOI: 10.1021/jacs.3c00341.

[61] Sorensen, J.; Hansen, E. L.; Larsen, D.; Elmquist, M. A.; Buchleithner, A.; Florean, L.; Beeren, S. R. Light-controlled enzymatic synthesis of gamma-CD using a recyclable azobenzene template. *Chem. Sci.* **2023**, *14* (28), 7725-7732. DOI: 10.1039/d3sc01997g.

[62] Hartman, A. M.; Jumde, V. R.; Elgaher, W. A. M.; Te Poele, E. M.; Dijkhuizen, L.; Hirsch, A. K. H. Potential Dental Biofilm Inhibitors: Dynamic Combinatorial Chemistry Affords Sugar-Based Molecules that Target Bacterial Glucosyltransferase. *Chemmedchem* **2021**, *16* (1), 113-123. DOI: 10.1002/cmdc.202000222.

[63] Jumde, R. P.; Guardigni, M.; Gierse, R. M.; Alhayek, A.; Zhu, D.; Hamid, Z.; Johannsen, S.; Elgaher, W. A. M.; Neusens, P. J.; Nehls, C.; et al. Hit-optimization using target-directed dynamic combinatorial chemistry: development of inhibitors of the anti-infective target 1-deoxy-d-xylulose-5-phosphate synthase. *Chem. Sci.* **2021**, *12* (22), 7775-7785. DOI: 10.1039/d1sc00330e.

[64] Aguanell, A.; Hennebelle, M.; Ortega, M. A.; Perez-Fernandez, R. Dynamic combinatorial chemistry directed by proteins and nucleic acids: a powerful tool for drug discovery. *Chem. Soc. Rev.* **2025**, *54* (15), 7093-7113, Review. DOI: 10.1039/d5cs00223k.

[65] Qi, D.; Shi, X.; Lin, C.; Holzhausen, F.; Ville, L.; Sun, X.; Luo, J.; Pitkänen, L.; Zhu, Y.; Rosenholm, J.; et al. Self-Adaptive Synthesis of Non-Covalent Crosslinkers while Folding Single-Chain Polymers. *Angew. Chem. Int. Ed.* **2024**, *136* (38). DOI: 10.1002/ange.202408670.

[66] Morrow, S. M.; Colomer, I.; Fletcher, S. P. A chemically fuelled self-replicator. *Nat. Commun.* **2019**, *10* (1), 1011. DOI: 10.1038/s41467-019-08885-9.

[67] Howlett, M. G.; Fletcher, S. P. From autocatalysis to survival of the fittest in self-reproducing lipid systems. *Nat. Rev. Chem.* **2023**, *7* (10), 673-691. DOI: 10.1038/s41570-023-00524-8.

[68] Zhou, Z.; Zhang, L.; Yang, Y.; Vitorica-Yrezabal, I. J.; Wang, H.; Tan, F.; Gong, L.; Li, Y.; Chen, P.; Dong, X.; et al. Growth of single-crystal imine-linked covalent organic frameworks using amphiphilic amino-acid derivatives in water. *Nat. Chem.* **2023**, *15* (6), 841-847. DOI: 10.1038/s41557-023-01181-6.

[69] Cao, Y.; Yang, J.; Eichin, D.; Zhao, F.; Qi, D.; Kahari, L.; Jia, C.; Peurla, M.; Rosenholm, J. M.; Zhao, Z.; et al. Self-Synthesizing Nanorods from Dynamic Combinatorial Libraries against Drug Resistant Cancer. *Angew. Chem. Int. Ed.* **2021**, *60* (6), 3062-3070. DOI: 10.1002/anie.202010937.

[70] Black, S. P.; Sanders, J. K.; Stefankiewicz, A. R. Disulfide exchange: exposing supramolecular reactivity through dynamic covalent chemistry. *Chem. Soc. Rev.* **2014**, *43* (6), 1861-1872. DOI: 10.1039/c3cs60326a.

[71] Zhang, Q.; Qu, D. H.; Feringa, B. L.; Tian, H. Disulfide-Mediated Reversible Polymerization toward Intrinsically Dynamic Smart Materials. *J. Am. Chem. Soc.* **2022**, *144* (5), 2022-2033. DOI: 10.1021/jacs.1c10359.

[72] Jin, S.; Oh, D. X.; Park, J. Dynamic Disulfide Chemistry for Functional Polymers: Self-Healing, Vitrimer Behavior, and Biochemical/Electronic Applications. *Chemsuschem* **2025**, e202501023. DOI: 10.1002/cssc.202501023.

[73] Schafer, F. Q.; Buettner, G. R. Redox environment of the cell as viewed through the redox state of the glutathione disulfide/glutathione couple. *Free Radic. Biol. Med.* **2001**, *30* (11), 1191-1212. DOI: 10.1016/s0891-5849(01)00480-4.

[74] Jones, D. P. Redefining oxidative stress. *Antioxid. Redox. Signal.* **2006**, *8* (9-10), 1865-1879. DOI: 10.1089/ars.2006.8.1865.

[75] Kahana, A.; Lancet, D. Self-reproducing catalytic micelles as nanoscopic protocell precursors. *Nat. Rev. Chem.* **2021**, *5* (12), 870-878. DOI: 10.1038/s41570-021-00329-7.

[76] Canal-Martin, A.; Perez-Fernandez, R. Biomimetic selenocystine based dynamic combinatorial chemistry for thiol-disulfide exchange. *Nat. Commun.* **2021**, *12* (1), 163. DOI: 10.1038/s41467-020-20415-6.

[77] Cheng, W.; Wang, G.; Pan, X.; Zhang, Y.; Tang, B. Z.; Liu, Y. Redox-responsive nanoparticles with Aggregation-Induced Emission (AIE) characteristic for fluorescence imaging. *Macromol. Biosci.* **2014**, *14* (8), 1059-1066. DOI: 10.1002/mabi.201400076.

[78] Wang, B.; Li, C.; Yang, L. J.; Zhang, C. R.; Liu, L. J.; Zhu, S.; Chen, Y.; Wang, Y. Tetraphenylethene decorated with disulfide-functionalized hyperbranched poly(amido amine)s as metal/organic solvent-free turn-on AIE probes for biothiol determination. *J. Mater. Chem. B* **2019**, *7* (24), 3846-3855. DOI: 10.1039/c9tb00214f.

[79] Drozdz, W.; Bouillon, C.; Kotras, C.; Richeter, S.; Barboiu, M.; Clement, S.; Stefankiewicz, A. R.; Ulrich, S. Generation of Multicomponent Molecular Cages using Simultaneous Dynamic Covalent Reactions. *Chem. Eur. J.* **2017**, *23* (71), 18010-18018. DOI: 10.1002/chem.201703868.

[80] Pappas, C. G.; Mandal, P. K.; Liu, B.; Kauffmann, B.; Miao, X.; Komaromy, D.; Hoffmann, W.; Manz, C.; Chang, R.; Liu, K.; et al. Emergence of low-symmetry foldamers from single monomers. *Nat. Chem.* **2020**, *12* (12), 1180-1186. DOI: 10.1038/s41557-020-00565-2.

[81] Ulrich, S. Growing Prospects of Dynamic Covalent Chemistry in Delivery Applications. *Acc. Chem. Res.* **2019**, *52* (2), 510-519. DOI: 10.1021/acs.accounts.8b00591.

[82] Hu, Y.; Cao, X.; Guo, Y.; Zheng, X.; Li, D.; Chen, S. K.; Chen, G.; You, J. An aggregation-induced emission fluorogen/DNA probe carrying an endosome escaping pass for tracking reduced thiol compounds in cells. *Anal. Bioanal. Chem.* **2020**, *412* (28), 7811-7817. DOI: 10.1007/s00216-020-02909-w.

[83] Altinbasak, I.; Arslan, M.; Sanyal, R.; Sanyal, A. Pyridyl disulfide-based thiol–disulfide exchange reaction: shaping the design of redox-responsive polymeric materials. *Polym. Chem.* **2020**, *11* (48), 7603-7624.

[84] Ryu, J. H.; Chacko, R. T.; Jiwpanich, S.; Bickerton, S.; Babu, R. P.; Thayumanavan, S. Self-cross-linked polymer nanogels: a versatile nanoscopic drug delivery platform. *J. Am. Chem. Soc.* **2010**, *132* (48), 17227-17235. DOI: 10.1021/ja1069932.

[85] Palanikumar, L.; Choi, E. S.; Cheon, J. Y.; Joo, S. H.; Ryu, J. H. Noncovalent Polymer-Gatekeeper in Mesoporous Silica Nanoparticles as a Targeted Drug Delivery Platform. *Adv. Funct. Mater.* **2015**, *25* (6), 957-965. DOI: 10.1002/adfm.201402755.

[86] Park, H.; Choi, Y.; Jeena, M. T.; Ahn, E.; Choi, Y.; Kang, M. G.; Lee, C. G.; Kwon, T. H.; Rhee, H. W.; Ryu, J. H.; et al. Reduction-Triggered Self-Cross-Linked Hyperbranched Polyglycerol Nanogels for Intracellular Delivery of Drugs and Proteins. *Macromol. Biosci.* **2018**, *18* (4), e1700356. DOI: 10.1002/mabi.201700356.

[87] Kim, S.; Jana, B.; Go, E. M.; Lee, J. E.; Jin, S.; An, E. K.; Hwang, J.; Sim, Y.; Son, S.; Kim, D.; et al. Intramitochondrial Disulfide Polymerization Controls Cancer Cell Fate. *Acs Nano* **2021**, *15* (9), 14492-14508. DOI: 10.1021/acsnano.1c04015.

[88] Kim, S.; Chae, J. B.; Kim, D.; Park, C. W.; Sim, Y.; Lee, H.; Park, G.; Lee, J.; Hong, S.; Jana, B.; et al. Supramolecular Senolytics via Intracellular Oligomerization of Peptides in Response to Elevated Reactive Oxygen Species Levels in Aging Cells. *J. Am. Chem. Soc.* **2023**, *145* (40), 21991-22008. DOI: 10.1021/jacs.3c06898.

[89] Kim, S.; Lee, Y.; Seu, M. S.; Sim, Y.; Ryu, J. H. Enzyme-instructed intramitochondrial polymerization for enhanced anticancer treatment without the development of drug-resistance. *J. Control. Release* **2024**, *373*, 189-200. DOI: 10.1016/j.jconrel.2024.07.029.

[90] Choi, E. S.; Kim, S.; Kim, D.; Choi, E.; Ryu, J. H. Drug-Loaded Nanogel for Efficient Orchestration of Cell Death Pathways by Intramitochondrial Disulfide Polymerization. *Small* **2024**, *20* (15), e2308872. DOI: 10.1002/smll.202308872.

[91] Su, X.; Ma, B.; Hu, J.; Yu, T.; Zhuang, W.; Yang, L.; Li, G.; Wang, Y. Dual-Responsive Doxorubicin-Conjugated Polymeric Micelles with Aggregation-Induced Emission Active Bioimaging and Charge Conversion for Cancer Therapy. *Bioconjug. Chem.* **2018**, *29* (12), 4050-4061. DOI: 10.1021/acs.bioconjchem.8b00671.

[92] Wu, X.; Xing, J.; Lyu, Y.; Yu, J.; Yang, J.; Qi, D.; Wang, X.; Lin, J.; Shao, G.; Wu, A.; et al. Kinetic control over co-self-assembly using an in situ dynamic covalent reaction resulting in a synergistic chemo-photodynamic therapy. *Cell Rep. Phys. Sci.* **2023**, *4* (10), 101598. DOI: https://doi.org/10.1016/j.xcrp.2023.101598.

[93] Luo, J.; Xie, Z.; Lam, J. W.; Cheng, L.; Chen, H.; Qiu, C.; Kwok, H. S.; Zhan, X.; Liu, Y.; Zhu, D.; et al. Aggregation-induced emission of 1-methyl-1,2,3,4,5-pentaphenylsilole. *Chem. Commun.* **2001**, (18), 1740-1741, 10.1039/B105159H. DOI: 10.1039/b105159h.

[94] Kasha, M. Energy Transfer Mechanisms and the Molecular Exciton Model for Molecular Aggregates. *Radiat. Res.* **1963**, *20* (1), 55-70.

[95] Leung, N. L.; Xie, N.; Yuan, W.; Liu, Y.; Wu, Q.; Peng, Q.; Miao, Q.; Lam, J. W.; Tang, B. Z. Restriction of intramolecular motions: the general mechanism behind aggregation-induced emission. *Chem. Eur. J.* **2014**, *20* (47), 15349-15353. DOI: 10.1002/chem.201403811.

[96] Mei, J.; Hong, Y.; Lam, J. W.; Qin, A.; Tang, Y.; Tang, B. Z. Aggregation-induced emission: the whole is more brilliant than the parts. *Adv. Mater.* **2014**, *26* (31), 5429-5479. DOI: 10.1002/adma.201401356.

[97] Li, Q.; Blancafort, L. A conical intersection model to explain aggregation induced emission in diphenyl dibenzofulvene. *Chem. Commun.* **2013**, *49* (53), 5966-5968, 10.1039/C3CC41730A. DOI: 10.1039/c3cc41730a.

[98] Peng, X. L.; Ruiz-Barragan, S.; Li, Z. S.; Li, Q. S.; Blancafort, L. Restricted access to a conical intersection to explain aggregation induced emission in dimethyl tetraphenylsilole. *J. Mater. Chem. C* **2016**, *4* (14), 2802-2810, 10.1039/C5TC03322E. DOI: 10.1039/c5tc03322e.

[99] Tu, Y.; Zhao, Z.; Lam, J. W. Y.; Tang, B. Z. Mechanistic connotations of restriction of intramolecular motions (RIM). *Natl. Sci. Rev.* **2021**, *8* (6), nwaa260. DOI: 10.1093/nsr/nwaa260.

[100] Zheng, M. X.; Wang, Y.; Hu, D. N.; Tian, M.; Wei, Y.; Yuan, J. Y. Construction and modulation of aggregation-induced emission materials based on dynamic covalent bonds. *Aggregate* **2024**, *5* (6). DOI: 10.1002/agt2.624.
[101] Wurthner, F.; Kaiser, T. E.; Saha-Moller, C. R. J-aggregates: from serendipitous discovery to supramolecular engineering of functional dye materials. *Angew. Chem. Int. Ed.* **2011**, *50* (15), 3376-3410. DOI: 10.1002/anie.201002307.
[102] Hestand, N. J.; Spano, F. C. Expanded Theory of H- and J-Molecular Aggregates: The Effects of Vibronic Coupling and Intermolecular Charge Transfer. *Chem. Rev.* **2018**, *118* (15), 7069-7163. DOI: 10.1021/acs.chemrev.7b00581.
[103] Hong, Y.; Lam, J. W.; Tang, B. Z. Aggregation-induced emission. *Chem. Soc. Rev.* **2011**, *40* (11), 5361-5388, 10.1039/C1CS15113D. DOI: 10.1039/c1cs15113d.
[104] Li, K.; Liu, B. AIE-active polymers and biomaterials. *Chem. Soc. Rev.* **2014**, *43*, 6570–6599. DOI: 10.1039/c4cs00130g.
[105] Lou, X. Y.; Yang, Y. W. Manipulating Aggregation-Induced Emission with Supramolecular Macrocycles. *Adv. Opt. Mater.* **2018**, *6* (22), 1800668. DOI: 10.1002/adom.201800668.
[106] Chen, Y. C.; Lam, J. W. Y.; Kwok, R. T. K.; Liu, B.; Tang, B. Z. Aggregation-induced emission: fundamental understanding and future developments. *Mater. Horiz.* **2019**, *6* (3), 428-433. DOI: 10.1039/c8mh01331d.
[107] Li, J.; Wang, J.; Li, H.; Song, N.; Wang, D.; Tang, B. Z. Supramolecular materials based on AIE luminogens (AIEgens): construction and applications. *Chem. Soc. Rev.* **2020**, *49* (4), 1144-1172. DOI: 10.1039/c9cs00495e.
[108] Li, Z.; Ji, X.; Xie, H.; Tang, B. Z. Aggregation-Induced Emission-Active Gels: Fabrications, Functions, and Applications. *Adv. Mater.* **2021**, *33* (33), e2100021. DOI: 10.1002/adma.202100021.
[109] Xie, Y.; Li, Z. Development of aggregated state chemistry accelerated by aggregation-induced emission. *Natl. Sci. Rev.* **2021**, *8* (6), nwaa199. DOI: 10.1093/nsr/nwaa199.
[110] Ji, J.; Yuan, J.; Wei, Y. Dynamic polymer networks with luminescent response. *Chem. Commun.* **2022**, *58*, 1601–1604. DOI: 10.1039/d1cc06022g.
[111] Xu, C.; Shen, H.; Liu, T.-M.; Kwok, R. T. K.; Lam, J. W. Y.; Tang, B. Z. Restriction of molecular motion to a higher level: Towards bright AIE dots for biomedical applications. *iScience* **2023**, *26* (5), 106568. DOI: https://doi.org/10.1016/j.isci.2023.106568.
[112] Jiang, B.-P.; Guo, D.-S.; Liu, Y.-C.; Wang, K.-P.; Liu, Y. Photomodulated Fluorescence of Supramolecular Assemblies of Sulfonatocalixarenes and Tetraphenylethene. *Acs Nano* **2014**, *8* (2), 1609-1618. DOI: 10.1021/nn405923b.
[113] Xue, X.; Jin, S.; Zhang, C.; Yang, K.; Huo, S.; Chen, F.; Zou, G.; Liang, X. J. Probe-inspired nano-prodrug with dual-color fluorogenic property reveals spatiotemporal drug release in living cells. *Acs Nano* **2015**, *9* (3), 2729-2739. DOI: 10.1021/nn5065452.
[114] Wang, P.; Yan, X.; Huang, F. Host-guest complexation induced emission: a pillar[6]arene-based complex with intense fluorescence in dilute solution. *Chem. Commun.* **2014**, *50* (39), 5017-5019. DOI: 10.1039/c4cc01560f.
[115] Zhang, N.; Trépout, S.; Chen, H.; Li, M.-H. AIE Polymer Micelle/Vesicle Photocatalysts Combined with Native Enzymes for Aerobic Photobiocatalysis. *J. Am. Chem. Soc.* **2023**, *145* (1), 288-299. DOI: 10.1021/jacs.2c09933.
[116] Brzechwa-Chodzynska, A.; Markiewicz, G.; Cecot, P.; Harrowfield, J.; Stefankiewicz, A. R. Self-assembly of a fluorescent hydrogen-bonded capsule based on an amino-acid functionalised tetraphenylethylene. *Chem. Commun.* **2023**, *59* (41), 6247-6250. DOI: 10.1039/d3cc01263h.
[117] Pan, G.; Wu, Z.; Liu, Z.; Xu, B.; Tian, W. Photoinduced Fluorescence Switching in Molecular Aggregates by Topological [2+2] Cycloaddition. *Angew. Chem. Int. Ed.* **2023**, *62* (22), e202303152. DOI: 10.1002/anie.202303152.

[118] Dong, Z.; Bi, Y.; Cui, H.; Wang, Y.; Wang, C.; Li, Y.; Jin, H.; Wang, C. AIE Supramolecular Assembly with FRET Effect for Visualizing Drug Delivery. *ACS Appl. Mater. Interfaces* **2019**, *11* (27), 23840-23847. DOI: 10.1021/acsami.9b04938.

[119] Wang, H.; Li, Q.; Alam, P.; Bai, H.; Bhalla, V.; Bryce, M. R.; Cao, M.; Chen, C.; Chen, S.; Chen, X.; et al. Aggregation-Induced Emission (AIE), Life and Health. *Acs Nano* **2023**, *17* (15), 14347-14405. DOI: 10.1021/acsnano.3c03925.

[120] Dwars, T.; Paetzold, E.; Oehme, G. Reactions in micellar systems. *Angew. Chem. Int. Ed.* **2005**, *44* (44), 7174-7199. DOI: 10.1002/anie.200501365.

[121] Serrano-Luginbühl, S.; Ruiz-Mirazo, K.; Ostaszewski, R.; Gallou, F.; Walde, P. Soft and dispersed interface-rich aqueous systems that promote and guide chemical reactions. *Nat. Rev. Chem.* **2018**, *2* (10), 306-327. DOI: 10.1038/s41570-018-0042-6.

[122] Chiappisi, L.; Yalcinkaya, H.; Gopalakrishnan, V. K.; Gradzielski, M.; Zemb, T. Catanionic surfactant systems-thermodynamic and structural conditions revisited. *Colloid Polym. Sci.* **2015**, *293* (11), 3131-3143. DOI: 10.1007/s00396-015-3739-9.

[123] Kalyanasundaram, K.; Thomas, J. K. Environmental Effects on Vibronic Band Intensities in Pyrene Monomer Fluorescence and Their Application in Studies of Micellar Systems. *J. Am. Chem. Soc.* **1977**, *99* (7), 2039-2044. DOI: DOI 10.1021/ja00449a004.

[124] Duhamel, J. New insights in the study of pyrene excimer fluorescence to characterize macromolecules and their supramolecular assemblies in solution. *Langmuir* **2012**, *28* (16), 6527-6538. DOI: 10.1021/la2047646.

[125] Ba-Salem, A. O.; Gong, R.; Duhamel, J. Characterization of the Interactions between an Unassociated Cationic Pyrene-Labeled Gemini Surfactant and Anionic Sodium Dodecyl Sulfate. *Langmuir* **2022**, *38* (24), 7484-7495. DOI: 10.1021/acs.langmuir.2c00452.

[126] Koehler, R. D.; Raghavan, S. R.; Kaler, E. W. Microstructure and dynamics of wormlike micellar solutions formed by mixing cationic and anionic surfactants. *J. Phys. Chem. B* **2000**, *104* (47), 11035-11044. DOI: 10.1021/jp0018899.

[127] Jensen, G. V.; Lund, R.; Narayanan, T.; Pedersen, J. S. Transformation from Globular to Cylindrical Mixed Micelles through Molecular Exchange that Induces Micelle Fusion. *J. Phys. Chem. Lett.* **2016**, *7* (11), 2039-2043. DOI: 10.1021/acs.jpclett.6b00767.

[128] Sharma, V. K.; Mitra, S.; Mukhopadhyay, R. Dynamic Landscape in Self-Assembled Surfactant Aggregates. *Langmuir* **2019**, *35* (44), 14151-14172. DOI: 10.1021/acs.langmuir.8b03596.

[129] La Sorella, G.; Strukul, G.; Scarso, A. Recent advances in catalysis in micellar media. *Green Chem.* **2015**, *17* (2), 644-683. DOI: 10.1039/c4gc01368a.

[130] Yu, J.; Qi, D.; Li, J. Design, synthesis and applications of responsive macrocycles. *Commun. Chem.* **2020**, *3* (1), 189. DOI: 10.1038/s42004-020-00438-2.

[131] Liu, F.; Danylchuk, D. I.; Andreiuk, B.; Klymchenko, A. S. Dynamic covalent chemistry in live cells for organelle targeting and enhanced photodynamic action. *Chem. Sci.* **2022**, *13* (13), 3652-3660. DOI: 10.1039/d1sc04770a.

[132] Zhang, Z.; Zhang, L.; Zhou, L.; Lei, Y.; Zhang, Y.; Huang, C. Redox signaling and unfolded protein response coordinate cell fate decisions under ER stress. *Redox Biol.* **2019**, *25*, 101047. DOI: 10.1016/j.redox.2018.11.005.

[133] Liu, Z.; Guo, J.; Qiao, Y.; Xu, B. Enzyme-Instructed Intracellular Peptide Assemblies. *Acc. Chem. Res.* **2023**, *56* (21), 3076-3088. DOI: 10.1021/acs.accounts.3c00542.

[134] Lancet, D.; Zidovetzki, R.; Markovitch, O. Systems protobiology: origin of life in lipid catalytic networks. *J. R. Soc. Interface* **2018**, *15* (144). DOI: 10.1098/rsif.2018.0159.

[135] Tu, Y. J.; Zhao, Z.; Lam, J. W. Y.; Tang, B. Z. Aggregate Science: Much to Explore in the Meso World. *Matter* **2021**, *4* (2), 338-349. DOI: 10.1016/j.matt.2020.12.005.

[136] Riener, C. K.; Kada, G.; Gruber, H. J. Quick measurement of protein sulfhydryls with Ellman's reagent and with 4,4'-dithiodipyridine. *Anal. Bioanal. Chem.* **2002**, *373* (4-5), 266-276. DOI: 10.1007/s00216-002-1347-2.

[137] Ashkenasy, G.; Hermans, T. M.; Otto, S.; Taylor, A. F. Systems chemistry. *Chem. Soc. Rev.* **2017**, *46* (9), 2543-2554. DOI: 10.1039/c7cs00117g.
[138] Sarkar, A.; Swinkels, P. J. M.; Duttenhofer, L.; Besenius, P.; Walther, A. Photoactivated Enzymatic Reaction Network Enables Spatiotemporal Programming of Thiol/Disulfide Redox Systems. *Angew. Chem. Int. Ed.* **2025**, *64* (25), e202503822. DOI: 10.1002/anie.202503822.
[139] Gottesman, M. M.; Fojo, T.; Bates, S. E. Multidrug resistance in cancer: role of ATP–dependent transporters. *Nat. Rev. Cancer* **2002**, *2* (1), 48-58.
[140] Peer, D.; Karp, J. M.; Hong, S.; Farokhzad, O. C.; Margalit, R.; Langer, R. Nanocarriers as an emerging platform for cancer therapy. *Nat. Nanotechnol.* **2007**, *2* (12), 751-760. DOI: 10.1038/nnano.2007.387.
[141] Lehn, J. M. Toward complex matter: supramolecular chemistry and self-organization. *Proc. Natl. Acad. Sci. U. S. A.* **2002**, *99* (8), 4763-4768. DOI: 10.1073/pnas.072065599.
[142] Frank, F. C. On spontaneous asymmetric synthesis. *Biochim. Biophys. Acta* **1953**, *11* (4), 459-463. DOI: 10.1016/0006-3002(53)90082-1.
[143] Blackmond, D. G. The origin of biological homochirality. *Cold Spring Harb. Perspect. Biol.* **2010**, *2* (5), a002147. DOI: 10.1101/cshperspect.a002147.
[144] Palmans, A. R.; Meijer, E. W. Amplification of chirality in dynamic supramolecular aggregates. *Angew Chem. Int. Ed.* **2007**, *46* (47), 8948-8968. DOI: 10.1002/anie.200701285.
[145] Ludlow, R. F.; Otto, S. Systems chemistry. *Chem. Soc. Rev.* **2008**, *37* (1), 101-108, 10.1039/B611921M. DOI: 10.1039/b611921m.
[146] Surman, A. J.; Rodriguez-Garcia, M.; Abul-Haija, Y. M.; Cooper, G. J. T.; Gromski, P. S.; Turk-MacLeod, R.; Mullin, M.; Mathis, C.; Walker, S. I.; Cronin, L. Environmental control programs the emergence of distinct functional ensembles from unconstrained chemical reactions. *Proc. Natl. Acad. Sci. U. S. A.* **2019**, *116* (12), 5387-5392. DOI: 10.1073/pnas.1813987116.
[147] Lyu, Y.; Wu, X. X.; Papageorgiou, A. C.; Yang, J. H.; Wang, X.; Qi, D. W.; Li, J. W. Dynamic covalent macrocycles co-delivering genes and drugs against drug-resistant cancer. *Cell Rep. Phys. Sci.* **2022**, *3* (11). DOI: 10.1016/j.xcrp.2022.101150.

TURUN
YLIOPISTO
UNIVERSITY
OF TURKU

Painosalama, Turku, Finland 2026

ISBN 978-952-02-0609-3 (PRINT)
ISBN 978-952-02-0610-9 (PDF)
ISSN 0082-7002 (Print)
ISSN 2343-3175 (Online)